Charmonium production as a function of charged-particle multiplicity in p-Pb collisions at $\sqrt{}$NN = 8.16 TeV with ALICE at the LHC

Theraa Tork

université PARIS-SACLAY

Charmonium production as a function of charged-particle multiplicity in p–Pb collisions at $\sqrt{s_{\mathrm{NN}}}$ = 8.16 TeV with ALICE at the LHC

Production de charmonium en fonction de la multiplicité de particules chargées dans les collisions p–Pb à $\sqrt{s_{\mathrm{NN}}}$ = 8.16 TeV dans ALICE au LHC

Thèse de doctorat de l'université Paris-Saclay

École doctorale n° 576, Particules, Hadrons, Énergie et Noyau : Instrumentation, Imagerie, Cosmos et Simulation (PHENIICS)
Spécialité de doctorat: Physique des particules
Graduate School : Physique.
Référent : Faculté des sciences d'Orsay

Thèse préparée dans l'unité de recherche **IJCLab** (Université Paris-Saclay, CNRS), sous la direction de **Zaida CONESA DEL VALLE**, Chargée de recherche CNRS, et la co-direction de **Christophe SUIRE**, Chargé de recherche CNRS

Thèse soutenue à Paris-Saclay, le 10 Octobre 2023, par

Theraa TORK

Composition du jury

Membres du jury avec voix délibérative

Marie-Hélène SCHUNE Directrice de recherche, Université Paris-Saclay (IJCLab)	Présidente
Philippe CROCHET Directeur de recherche, Université Clermont Auvergne (LPC)	Rapporteur & Examinateur
Raphaël GRANIER DE CASSAGNAC Directeur de recherche, École polytechnique(LLR)	Rapporteur & Examinateur
Alberto BALDISSERI Directeur de recherche, Université Paris-Saclay (CEA)	Examinateur
Elena GONZALEZ FERREIRO Professeure, University of Santiago de Compostela	Examinatrice

THESE DE DOCTORAT
NNT : 2023UPASP125

université PARIS-SACLAY

ÉCOLE DOCTORALE
Particules, hadrons, énergie et noyau : instrumentation, imagerie, cosmos et simulation (PHENIICS)

Titre: Production de charmonium en fonction de la multiplicité de particules chargées dans les collisions p–Pb à $\sqrt{s_{NN}}$ = 8.16 TeV dans ALICE au LHC

Mots clés: Charmonia, dépendance en multiplicité, collisions proton-noyau, ALICE, LHC

Résumé: Dans la matière ordinaire, les quarks et les gluons ne peuvent être trouvés que dans un état confiné, appelés hadrons. Cependant, la chromodynamique quantique sur réseau prédit l'existence d'un état déconfiné de quarks et de gluons, le plasma de quarks et de gluons (QGP). Dans la nature, il est possible que le QGP ait pu exister pendant les premières microsecondes de l'univers, où des conditions extrêmes de haute densité d'énergie et de haute température auraient été présentes. De telles conditions peuvent être reproduites en laboratoire en faisant entrer en collision des ions lourds à des énergies suffisamment élevées. En raison de sa courte durée de vie, plusieurs observables indirectes sont utilisées pour caractériser le QGP. En plus des effets du QGP, les observables peuvent également être affectées par la présence des noyaux, appelés effets de matière nucléaire froide (CNM). Pour dissocier les effets du QGP des effets de CNM, des collisions proton-noyau, dans lequelles on ne s'attend pas à former du QGP, sont utilisées comme système de contrôle. L'une des observables les plus intéressantes pour sonder le QGP est l'étude famille des quarkonia. Les quarkonia sont des états liés de paires de quarks-antiquarks lourds ($c\bar{c}$ or $b\bar{b}$). En raison de leur masse élevée, le mécanisme de production des quarks lourds se produit à des échelles de haute impulsion de la chromodynamique quantique (QCD), tandis que la formation des états liés implique des échelles plus basses impulsion de la QCD. Les quarkonia sont donc sensibles à la fois aux aspects perturbatifs et non-perturbatifs de la QCD. De plus, leur mesure dans les collisions p–Pb fournit des informations sur les effets de la matière nucléaire froide, tels que le shadowing nucléaire ou l'interaction avec les particules qui se déplacent avec elles. Des mesures récentes révèlent que les taux de production des J/Ψ augmentent avec la multiplicité des particules chargées dans les collisions pp et p-Pb au LHC. Différents mécanismes ont été proposés pour expliquer cette observation. L'un d'eux est l'influence des interactions à plusieurs partons dans l'état initial de la collision. Les mesures des états excités du charmonium, par exemple $\Psi(2S)$, en fonction de la multiplicité des particules chargées, sont essentielles pour dissocier l'impact des éventuels effets de l'état final. Dans cette thèse, nous présentons la mesure des les taux de production du charmonium en fonction de la multiplicité des particules chargées, mesurée à rapidité centrale ($|\eta| < 1.0$). Les J/Ψ et $\Psi(2S)$ sont reconstruits dans leur canal de désintégrations en dimuons dans les régions de rapidité $2.03 < y_{\rm cms} < 3.53$ et $-4.46 < y_{\rm cms} < -2.96$. Cette mesure est réalisée à l'aide de collisions p–Pb à $\sqrt{s_{\rm NN}}$ = 8.16 TeV dans ALICE, expérience dédiée aux ions lourds au LHC du CERN. De plus, nous présentons des résultats préliminaires pour l'incertitude systématique de l'efficacité de la reconstruction des traces dans le spectromètre à muon d'ALICE. Cette partie a été réalisée en utilisant un jeu de données de collisions pp à $\sqrt{s}$ = 13.6 TeV collecté en 2022.

université PARIS-SACLAY

ÉCOLE DOCTORALE
Particules, hadrons, énergie et noyau : instrumentation, imagerie, cosmos et simulation (PHENIICS)

Title: Charmonium production as a function of charged-particle multiplicity in p–Pb collisions at $\sqrt{s_{NN}} = 8.16$ TeV with ALICE at the LHC

Keywords: Charmonia, charged-particle multiplicity, proton-nucleus collisions, ALICE, LHC

Abstract: In ordinary matter, quarks and gluons can only be found in a confined state, forming hadrons. However, lattice QCD predicts the existence of the quark-gluon plasma (QGP), a deconfined state of quarks and gluons, at extremely high energy density and temperature. In nature, QGP may have existed during the first microseconds of the universe, where such extreme conditions occurred. Such conditions are reproduced in the laboratory by colliding heavy ions at sufficiently high energy. Due to its short lifetime, the QGP can not be characterized by direct observations. The influence of its formation on particle production is used to characterize it. In heavy-ion collisions, besides QGP effects, the observables might also be affected by the presence of the nuclei, the so-called cold nuclear matter (CNM) effects. To disentangle the QGP effects from the CNM effects, proton-nucleus collisions are used as a control system in which QGP is not expected to be formed. One of the main tools used to probe QGP is quarkonia. Quarkonia are bound states of heavy quark-antiquark pairs ($c\bar{c}$ or $b\bar{b}$ pairs). Due to their large mass, heavy-quark production mechanism takes place at hard scales of QCD, while the formation of the bound states involves soft QCD scales. Quarkonia are, therefore, sensitive to both perturbative and non-perturbative aspects of QCD. In addition, their measurement in p–Pb collisions provides information on CNM effects, such as nuclear shadowing or the interaction with comoving particles. Recent measurements reveal that J/Ψ yields increase with charged-particle multiplicity in pp and p–Pb collisions at the LHC. Different mechanisms were proposed to explain this observation. One of them is the influence of multiple parton interactions in the initial state of the collision. Measurements of the excited charmonium states, e.g., $\Psi(2S)$, as a function of charged-particle multiplicity, are essential to disentangle the impact of possible final-state effects. In this thesis, we present the measurement of charmonium yields as a function of charged-particle multiplicity, measured at central rapidity ($|\eta| < 1.0$). J/Ψ and $\Psi(2S)$ are reconstructed in their dimuon decays within the rapidity region $2.03 < y_{\mathrm{cms}} < 3.53$ and $-4.46 < y_{\mathrm{cms}} < -2.96$. This measurement is performed using in p–Pb collisions at $\sqrt{s_{\mathrm{NN}}} = 8.16$ TeV collected by ALICE at the LHC (CERN). In addition, we present preliminary results of the systematic uncertainty of the muon spectrometer tracking efficiency in Run 3. This study was performed using a data set of pp collisions at $\sqrt{s} = 13.6$ TeV.

Dedication

لله الحمد من قبل ومن بعد

إلى رفاق الخطوة الأولى و الطريق الصعب: أبي و أمي محمد ترك و ماجدة رضوان.

إلى عرين و ثائر و مرح أصدقائي الصادقين على مر السنين.

إلى أهلي أهل فلسطين الصابرين الصامدين.

أهدي هذا لكم ، منكم أنتم تعلمت أن الحياة لا معنى لها بلا صبر وابتسامة.

Mahmoud Darwish, a Palestinian poet, once said:
As you conduct your wars, think of others
(do not forget those who seek peace).
As you pay your water bill, think of others
(those who are nursed by clouds).
As you return home, to your home, think of others
(do not forget the people of the camps).
As you sleep and count the stars, think of others
(those who have nowhere to sleep).
As you liberate yourself in metaphor, think of others
(those who have lost the right to speak).
As you think of others far away, think of yourself
(say: “If only I were a candle in the dark”)."

To the people of Palestine, one day we will be free!

Acknowledgement

I would like to express my deepest gratitude to all those who have contributed to the completion of this thesis. This journey would not have been possible without the support, guidance, and encouragement of many individuals.
First and foremost, I extend my heartfelt thanks to my supervisors Zaida Conesa del Valle and Christophe Suire. Thank you for the guidance, help, and support during these three years. Thank you both for your availability to discuss and to answer my questions and for your patience, especially when correcting my typos!
I am also grateful to all the members of the ALICE group at IJCLab. Thank you Cynthia, Laure, and Bruno for all the discussions, support, and advice you gave to me. Corentin, my office mate, thank you for all our conversations in Arabic, English, and French, and for all the games you taught me. I would also like to thank all the previous and current students and post-docs in the ALICE group: Chun-Lu, Sizar, Afnan, Andrea, Dukishyam, Qasem, and Juliette. Thank you all for all the fun time that we had together.
Special thanks to Marie Hélène-Schune, Philippe Crochet, Raphael Granier De Cassagnac, Alberto Baldisseri, and Elena Gonzalez Ferreiro for accepting to be the jury of my thesis defense and for all the comments and suggestions you gave me.
I came for the first time to France via a collaboration between AN-Najah National University and Paris-Saclay University to do my master's internship in Osay. A special thank you goes to Achille Stocchi, Ahmed Bassalat, and Hadil Abualrob, who are leading this collaboration. Without your effort and support, this achievement would not be possible. I would also like to thank David Rousseau, Lydia Fayard from the ATLAS group, and Marie Hélène-Schune and Fabrice Desse from the LHCb group, for accepting me to join their teams during my first and second internships in France.
A very special and warm thank you go to Sara Sellam, my lovely and clever friend ;), who

flew from Spain to Paris to help and support me during my defense. Thank you for all the fun time we spent at CERN, Santiago, and Paris.

To the Mosquéetienne team, thank you for all the lovely Friday nights we spent together. Thank you Milie, Emma, Amy, Mariyatou, Aude, Ghadeer, Laila, Sarnya, and Hajar.

Thanks to the funny and lovely Palestinian family in France with whom I shared so many nice moments during these three years. Thank you "آل ماعand آل باتشينو": Massa, Shaymaa, Manar, Reema, Ola, Afnan, Rasha, Rand, Kholoud, Fidaa, Sali, Ikhlas, Raneem, and Shereen. Love you all!

To my friends back home, thank you for the endless love and support. To Ayyat, Asmaa, Asmaa, Wafa, Nawal, Mitha, Wafaa, Fatima, Najwa, Sabrine, Yafa, Jihad, Ekhlas, Amal.

إنّما سمّي الخليل خليلًا؛ لأنّ محبّته تتخلّل القلب فلا تدع فيه خللًا إلّا ملأته.

Finally, to the heroes of my life: my parents and my lovely siblings, Areen, Thaer, and Marah. Thank you for your unconditional love and endless support. أحبكم

في النهاية كما قالت رضوى: هناك احتمال آخر لتتويج مسعانا بغير الهزيمة، ما دمنا قررنا أننا لن نموت قبل أن نحاول أن نحيا

Theraa ثراء
Paris, November 2023.

Table of contents

Synthèse en français

Dans la nature, les quarks et les gluons, c'est-à-dire les particules élémentaires de la matière QCD ordinaire, sont toujours confinés à l'intérieur des hadrons, un phénomène connu sous le nom de confinement de la QCD. Cependant, dans des conditions extrêmes de densité d'énergie et de température, la matière QCD subit une transition de phase vers un état où les quarks et les gluons se déplacent librement, créant ce que l'on appelle le plasma de quarks et de gluons (QGP). Ces conditions extrêmes peuvent être recréées en laboratoire grâce à des collisions d'ions lourds ultra-relativistes. En raison de sa durée de vie très courte, typiquement de l'ordre du femtoseconde par la vitesse de la lumière (fm/c), le QGP ne peut pas être détecté directement. Pour explorer et comprendre le QGP, l'étude de la production de charmonia sert d'outil précieux. Les quarks charmés sont produits au cours des premières étapes de ces collisions, avant la formation du QGP, et par la suite, ils sont influencés par l'évolution du milieu.

L'étude de la production de charmonium dans des systèmes de petite taille, tels que les collisions proton-proton ou proton-ion lourd, est essentielle car ces systèmes servent de points de référence où aucun effet du QGP n'est attendu. Néanmoins, plusieurs comportements QGP-like inattendus ont été observés dans des systèmes de petite taille lors d'événements de haute multiplicité, ce qui a conduit à considérer les interactions multipartoniques comme un scénario clé pour expliquer ces résultats. L'étude de la production de charmonium en fonction de la multiplicité de particules chargées est une méthode pour sonder ces interactions multipartoniques. L'objectif principal de cette thèse est d'analyser la production de charmonium en fonction de la multiplicité de particules chargées dans les collisions p–Pb à une énergie de centre de masse de $\sqrt{s_{\rm NN}} = 8{,}16$ TeV en utilisant l'expérience ALICE au Grand Collisionneur de Hadrons (LHC).

Dans le chapitre 1, je commence par expliquer les concepts fondamentaux liés au

plasma de quarks et de gluons et aux méthodes utilisées pour l'étudier. Ensuite, je présente des exemples de comportements QGP-like surprenants observés dans des systèmes de petite taille. Le chapitre se conclut par un aperçu des études de quarkonium concernant la multiplicité de particules chargées.

Dans le chapitre 2, je discute de l'équipement expérimental utilisé pour recueillir l'ensemble de données utilisé pour l'analyse. Je commence par une brève explication du processus d'accélération, puis je me plonge dans la description du détecteur ALICE, en mettant l'accent sur les composants utilisés pour évaluer les rendements de charmonium et la multiplicité de particules chargées.

Le chapitre 3 fournit une explication détaillée de la procédure utilisée pour évaluer la multiplicité de particules chargées et les rendements de charmonium. La première section couvre les observables étudiés, suivie d'une présentation de l'échantillon de données utilisé pour l'analyse et des critères de sélection des traces et des événements. La troisième section décrit la méthodologie pour déterminer la multiplicité de particules chargées, notamment l'utilisation du nombre de tracelettes comme estimateur de la multiplicité. Une simulation Monte Carlo est utilisée pour mesurer les corrélations et convertir le nombre de segments de trace en multiplicité de particules chargées. Le chapitre se termine par une explication des sources d'incertitudes systématiques évaluées pour la mesure de la multiplicité de particules chargées. Dans les trois dernières sections de ce chapitre, j'explique la procédure pour mesurer les rendements de charmonium normalisés à eux-mêmes. Cela commence par l'ajustement du spectre de masse des dimuons pour extraire les rendements bruts de J/ψ et de ψ(2S). Ensuite, j'explique la correction appliquée aux rendements bruts pour obtenir les rendements de charmonium normalisés à eux-mêmes. Les incertitudes systématiques évaluées pour les rendements de charmonium sont expliquées dans la dernière section de ce chapitre.

Dans le chapitre 4, je présente les résultats de cette thèse : les résultats dépendant de la multiplicité de ψ(2S), J/ψ et ψ(2S)-sur-J/ψ. Cela est suivi de la discussion des mesures de quarkonium et de saveurs lourdes ouvertes disponibles en fonction de la multiplicité.

Pendant le deuxième arrêt prolongé (2018-2022), ALICE a subi plusieurs mises à niveau pour se préparer à la prise de données de la Run3. Dans le chapitre 5, nous discutons brièvement des mises à niveau des sous-détecteurs d'ALICE, en mettant l'accent sur ceux utilisés pour l'analyse des quarkonia. Parmi ces mises à niveau, il y a le remplacement de l'électronique des chambres de trajectographie des muons (MCH). Cela est fait pour améliorer la robustesse du détecteur afin de faire face à la luminosité accrue attendue dans la Run3. Dans cette partie, notre principal objectif est d'évaluer l'incertitude de l'efficacité

de suivi du détecteur MCH. Dans le chapitre 6, j'explique la procédure pour évaluer cette incertitude et les résultats obtenus à l'aide d'un échantillon de la prise de données de la Run 3.

General introduction

In Nature, quarks and gluons, i.e., the elementary particles of ordinary QCD matter, are always found to be confined inside hadrons. This is known as QCD confinement. However, under extreme conditions of energy density and temperature, QCD matter undergoes a phase transition to a state of freely moving quarks and gluons, known as quark-gluon plasma (QGP). Such conditions can be reproduced in the laboratory using ultra-relativistic heavy-ion collisions. Due to its very short lifetime, typically on the order of a few fm/c, the QGP cannot be observed directly. To probe the QGP, the study of charmonia production is an excellent tool, as the charm quarks are produced during the initial stages of the collision, before the QGP formation, and experience the entire medium evolution.
The study of charmonium production in small systems, i.e., proton–proton or proton–heavy-ion collisions, is essential as a reference since no QGP effects are expected in small systems. However, several surprising QGP-like behaviors have been observed in small systems in high multiplicity events. Multiple-parton interactions is one of the main scenarios proposed to understand these findings. Studying charmonium production as a function of charged-particle multiplicity is one way to probe multiple-parton interactions. In this thesis our goal is to study the charmonium production as a function of charged-particle multiplicity in p–Pb collisions at $\sqrt{s_{\rm NN}}$ = 8.16 TeV with the ALICE experiment at the LHC. In particular, the measurements reported in this thesis on both ground and excited charmonium states bring additional information on the role of final state effects at play in p–Pb collisions, as the role of initial state effects is expected to be similar for ground and excited quarkonium states.
In chapter 1, I introduce the fundamental concepts of the quark-gluon plasma and its probes. Then, I discuss some examples of the surprising QGP-like behaviors in small systems. I close the chapter with an overview of the quarkonium studies as a function of charged-particle multiplicity.

In chapter 2, I discuss the experimental apparatus used to collect the data set used in the analysis. I start with a brief explanation of the accelerator chain process. This is followed by the description of the ALICE detector focusing on the sub-detectors used to evaluate the charmonium yields and the charged-particle multiplicity.
In chapter 3, I provide a detailed explanation of the procedure used to evaluate the charged-particle multiplicity and charmonium yields. In the first section, I explain the observables studied in this analysis. In the second section, I present the data sample used in this analysis, as well as the track and event selections applied to this data sample. In the third section, I explain the procedure to determine the charged-particle multiplicity. The multiplicity estimator used in the analysis is the number of tracklets (or track segments) reconstructed in the Silicon Pixel Detector. A Monte Carlo simulation is used to evaluate the correlation and convert the number of tracklets into the charged-particle multiplicity. This section ends with an explanation of the systematic uncertainties evaluated for the charged-particle multiplicity measurement. In the last three sections of this chapter, I explain the procedure to measure the self-normalized charmonium yields. This starts with fitting the invariant mass spectrum of the dimuon to extract the raw J/ψ and ψ(2S) yields. Then, I explain the corrections applied to the raw yields in order to obtain the self-normalized charmonium yields. The systematic uncertainties evaluated for the charmonium yields are explained in the last section of this chapter.
In chapter 4, I present the results of this thesis: the ψ(2S) and the J/ψ self-normalized yields, as well as the ψ(2S)-over-J/ψ ratio as a function of the self-normalized charged-particle multiplicity. This is followed by a discussion of the available quarkonium and open heavy-flavor measurements to date.
During the second long shutdown (2018-2022), ALICE underwent several upgrades in order to prepare for the Run 3 data taking. In chapter 5, we briefly discuss the upgrades of the ALICE sub-detectors focusing on those that are used for the quarkonia analysis. Among these upgrades is the replacement of the electronics of the muon tracking chambers (MCH). This is done to enhance the robustness of the detector to cope with the increased luminosity expected in Run 3. In this part, our main goal is to evaluate the MCH detector tracking efficiency uncertainty. In chapter 6, I explain the procedure to evaluate this uncertainty and the results obtained using a sample from Run 3 data taking.

Part I

Introduction

1 Introduction

1.1 The Standard Model of particle physics and Quantum Chromodynamics

The Standard Model (SM) is the cornerstone of our understanding of the fundamental constituents of Nature. It provides a comprehensive framework for describing elementary particles and their interactions. Fig.1.1 presents an overview of the particles in the SM. The SM classifies elementary particles into four types: two families of spin-1/2 fermions (leptons and quarks), one family of spin-1 bosons known as gauge bosons (which serve as force carriers), and a spin-0 particle called the Higgs boson.

The quarks consist of three generations: the first (and lighter) is made up of up (u) and down (d) quarks, the second of charm (c) and strange (s) quarks, the third of top (t) and bottom (b) quarks. The quarks carry a non-integer electric charge. The u, c, and t quarks have a $+2/3$ e, while the d, s, and b quarks carry a negative electric charge of $-1/3$ e. The quarks also have a color charge and come in a blue, red, or green color. In ordinary matter, quarks can only be found in confined colorless states called hadrons. The leptons are also grouped into three generations: the first generation contains the electron (e) and its associated neutrino (ν_e), the second generation consists of the muon (μ) and its associated neutrino (ν_μ), while the third generation is made up of the tau (τ) and its associated neutrino (ν_τ). Figure 1.1 represents this classification of elementary particles.

Our universe is governed by four forces: the strong force, the electromagnetic force, the

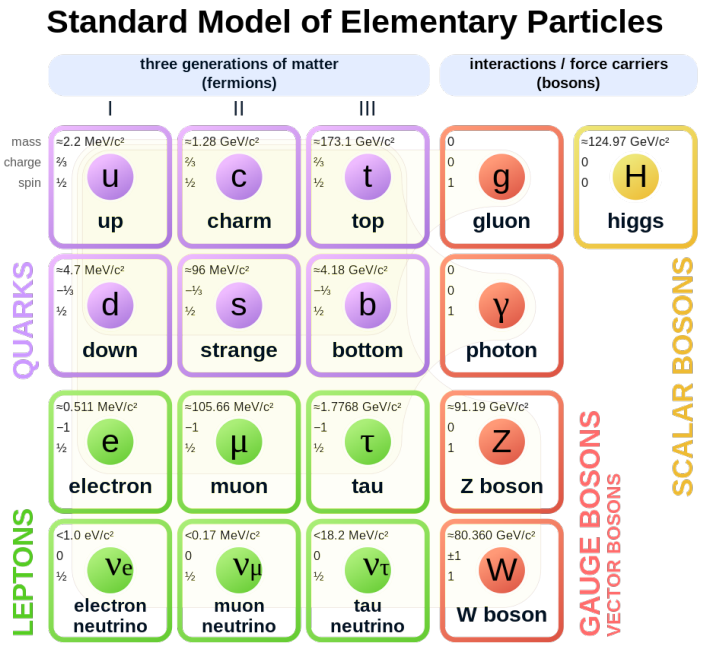

Figure 1.1: The standard model of elementary particles [1].

weak force, and the gravitational force. However, the SM only describes three of them, as the gravitational force carriers are not yet included in the SM. The electromagnetic interaction is described by the theory of Quantum Electrodynamics (QED). All the electrically charged fermions can interact electromagnetically by exchanging photons (γ). The weak interaction is described by the electroweak theory, which unifies the electromagnetic and the weak interactions. Within this framework, all fermions can go through a weak interaction by exchanging $W^{\pm}$ or Z bosons. The strong interaction is described by the Quantum Chromo-Dynamics (QCD) theory. Particles with color charges, namely quarks and gluons, can interact strongly by exchanging gluons (g). In the standard model, the mass of the elementary particles arises through their interaction with the Higgs field [2]. The Higgs boson, the quantum of the Higgs field, was discovered in 2012 at CERN by two LHC experiments, ATLAS [3] and CMS [4].

Quantum Chromodynamics (QCD)

Quantum Chromodynamics (QCD) is the gauge field theory that describes the strong interactions of the colored particles, i.e., quarks and gluons [5]. The coupling constant of QCD α_s describes the strength of interaction and depends on the momentum transferred (Q). It can

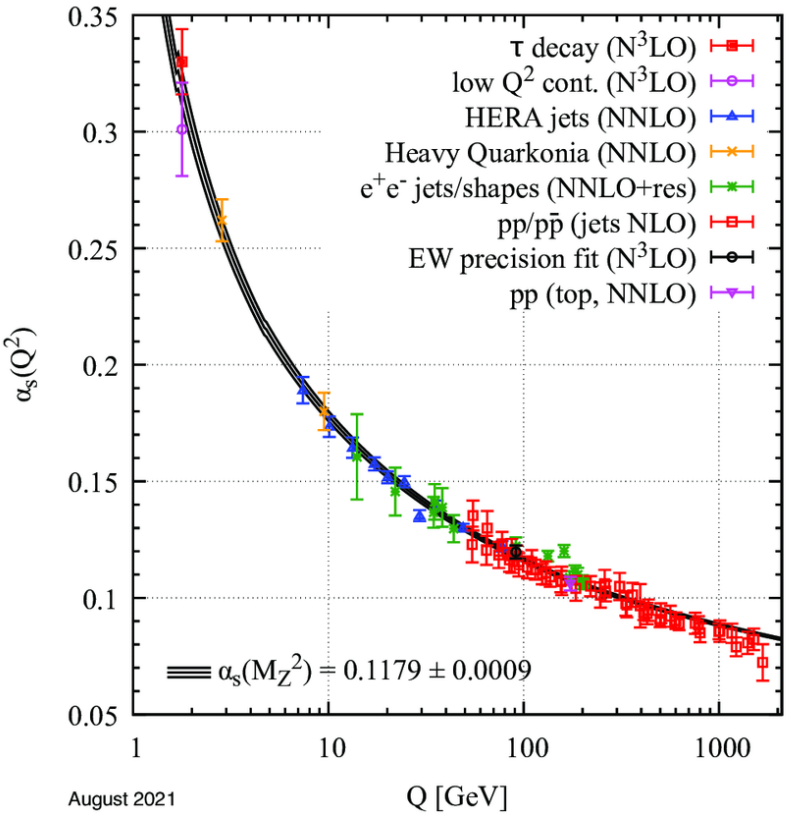

Figure 1.2: Summary of measurements of the QCD coupling constant α_s as a function of the energy scale Q [5].

be obtained at the leading order from:

$$\alpha_s = \frac{\alpha_s(\mu^2)}{1 + \alpha_s(\mu^2)\left(\frac{33-2n_f}{12\pi}\right)\ln\left(\frac{Q^2}{\mu^2}\right)}, \tag{1.1}$$

where μ is the scale of the renormalization, n_f is the number of quark flavors. Fig.1.2 shows the behavior of α_s as a function of Q. Following the figure, as $Q \longrightarrow \infty$, α_s decreases, which means that the quarks behave as if they are free particles. This phenomenon is known as asymptotic freedom. The strong interaction can be fully described in this energy region using perturbative QCD. On the other hand, when the value of Q decreases and becomes close to the QCD scale ($\Lambda_{QCD} \sim 200$ MeV), the coupling increases, which implies that the quarks are strongly bound inside hadrons, and it becomes impossible to separate them. This phenomenon is known as confinement. In this regime, the perturbative QCD is no longer applicable, and other techniques like Lattice QCD are used to solve the QCD Lagrangian.

1.2 Quantum Chromodynamics under extreme conditions: Quark Gluon Plasma

The QCD state where quarks and gluons are freely moving is known as Quark Gluon Plasma (QGP). In Fig.1.3, the QCD phase diagram describes the state of matter as a function of temperature (T) and baryochemical potential (μ_B), which in this context can be associated to the net baryon density. For low μ_B and T values, the quarks and gluons are found only in color-neutral states, the so-called hadrons. The transition from the hadron phase to the QGP phase is of cross-over type at a T ~ 170 MeV and low μ_B [6] (smooth transition where the two phases coexist). Moving to a higher μ_B, the transition becomes of first-order type [7].

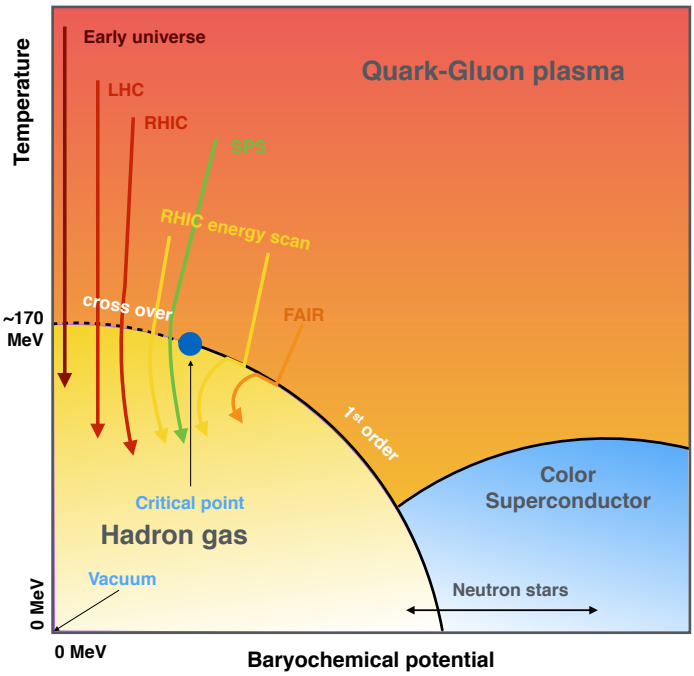

Figure 1.3: Conceptual drawing for the QCD phase diagram [8].

Evolution of a heavy-ion collision

Experimentally, the QGP can be created in the laboratory by generating conditions of high energy density and high temperature. This is achieved through high-energy heavy-ion collisions, such as Pb–Pb collisions at the LHC or Au–Au collisions at RHIC. In the following, we describe the evolution of a heavy-ion collision [9, 8] as schematically depicted in Fig.1.4.

The timescales shown in the figure are indicative. Due to their ultra-relativistic velocity, the colliding nuclei are Lorentz contracted along their direction of motion.

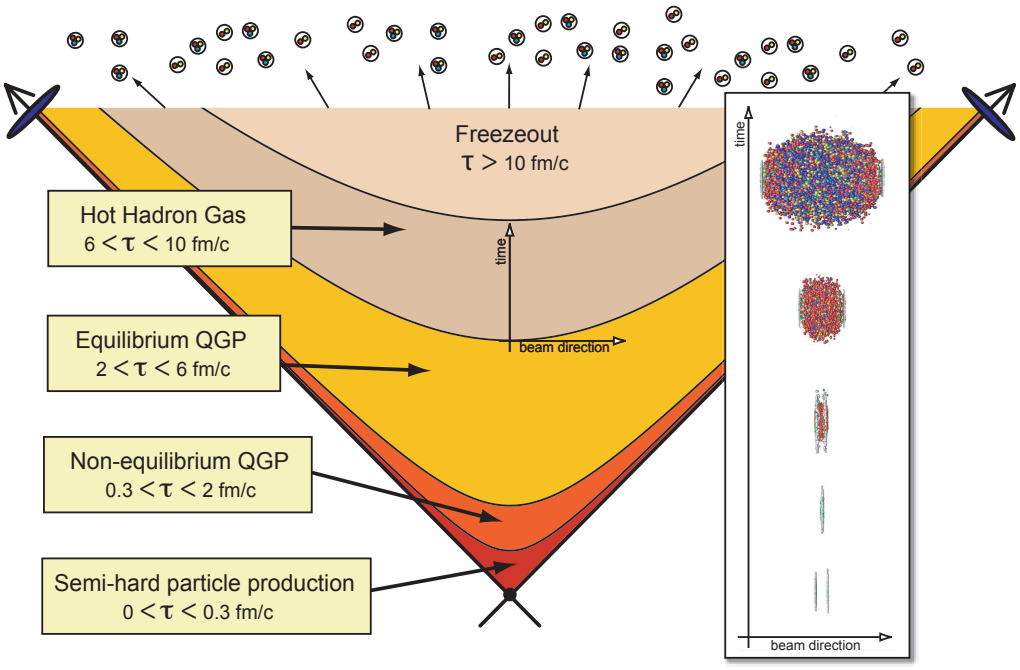

Figure 1.4: Schematic representation of the time evolution of a heavy-ion collision. Taken from [8].

The collision takes place at time $\tau = 0$ and go through the following stages:

- $0 < \tau < 0.3$ fm/c: hard scattering processes, i.e., scatterings with large momentum transfer between the partons of the colliding nuclei, take place;
- $0.3 < \tau < 2$ fm/c: rescatterings of the partons created from the inelastic collision may lead to the thermalization of the system. The energy-density of the medium reaches up to 12–20 GeV/fm^3 (these values correspond to 0-5% Pb–Pb collisions at $\sqrt{s_{\mathrm{NN}}} = 2.76$ TeV and the correspondent expectations for the core of the collision) [10], which is twenty times higher than the average energy-density inside a hadron [11]. This can lead to the creation of non-equilibrium QGP;
- $2 < \tau < 6$ fm/c: the QGP is in an equilibrium stage, in which the viscous hydrodynamics can be used to model the system. Then, the system starts to expand and cool down;

- $6 < \tau < 10$ fm/c: the system reaches the critical temperature in which the hadrons start to be created. The system reaches a chemical freeze-out stage where no further inelastic collisions occur, and the total number of hadrons remains constant;
- $\tau > 10$ fm/c: the system continues to expand and cool down until it reaches the kinetic freeze-out where no more elastic collisions occur. At this stage, the kinetic properties of the particles are fixed. After that, the particles start to fly away to be detected.

1.2.1 Quark gluon plasma probes

Due to its extremely short lifetime of approximately 10 fm/c at the LHC collision energies [12], direct detection of the QGP is impossible. Instead, several indirect probes are employed to investigate the properties of the QGP. These probes can be classified into two categories depending on the momentum scale involved: hard and soft probes. Hard probes refer to observables that arise from processes with high momentum transfer, occurring only during the initial stages of the collision. Examples of hard probes for the QGP include jet quenching, the production of heavy flavor particles, heavy quarkonia production, and weak boson production. On the other hand, soft probes involve processes with relatively low momentum transfer. Such observables can be generated throughout all the stages of the system evolution. Examples of soft probes include the flow of charged particles and electromagnetic probes such as photons.

QGP experimental observables

Several experimental observables confirm the discovery of QGP. A complete overview of the QGP observables can be found in the following references [13–18]. In the following discussion, we present two specific observables: the elliptic flow of charged particles and the enhancement of strange hadron production. These two were among the early indicators of the formation of the QGP.

Strangeness enhancement: the strange hadron production in AA collisions serves as an essential tool for investigating the properties of the QGP in AA collisions. Unlike the up and down quarks, strange quarks are not present as valence quarks in the colliding particles. However, due to their relatively low mass, they are abundantly produced during the collision. In the initial stages of the system evolution, the strange quarks are produced from the hard partonic scattering processes via flavor creation, i.e., $gg \rightarrow s\bar{s}$ and $q\bar{q} \rightarrow s\bar{s}$, and flavor excitation $gs \rightarrow gs$ and $qs \rightarrow qs$. In addition, strange quarks can be produced

during the subsequent partonic evolution via gluon splitting g → s$\bar{s}$. In the later stages of the system evolution, the soft QCD processes dominate the strangeness production. In a QGP environment, strange quarks are expected to restore their bare mass $m_q \sim 0$ due to the chiral symmetry restoration. Consequently, strange hadron production becomes easier in a QGP (vs. vacuum), and is expected to be enhanced in AA collisions due to the presence of the QGP. Experimentally, the enhancement of strangeness production in AA collisions has been observed by several experiments and at different collision energies [19–22]. These studies have found that the ratio of strange hadrons to those composed of lighter hadrons (consisting of up and down quarks) is significantly higher in AA collisions compared to pp collisions.

Elliptic flow of charged particles: it refers to the preferential alignment of emitted particles in the reaction plane during non-central heavy-ion collisions. Fig.1.5 presents a conceptual drawing for a heavy-ion collision describing the origin of elliptic flow. This phenomenon is a consequence of the initial spatial anisotropy, as the overlap region of colliding nuclei has an almond shape due to the geometric configuration of the collision. When the energy density is large enough (e.g. QGP), particles created in the overlap region reinteract. This implies that a strong pressure gradient will be generated on the particle located along the short axis, x-axis in Fig.1.5, and a weaker pressure gradient on the particles located along the long-axis, y-axis in Fig.1.5. This angular anisotropy of pressure will generate angular anisotropy of momentum, leading to asymmetries in the final state particle distributions [23].

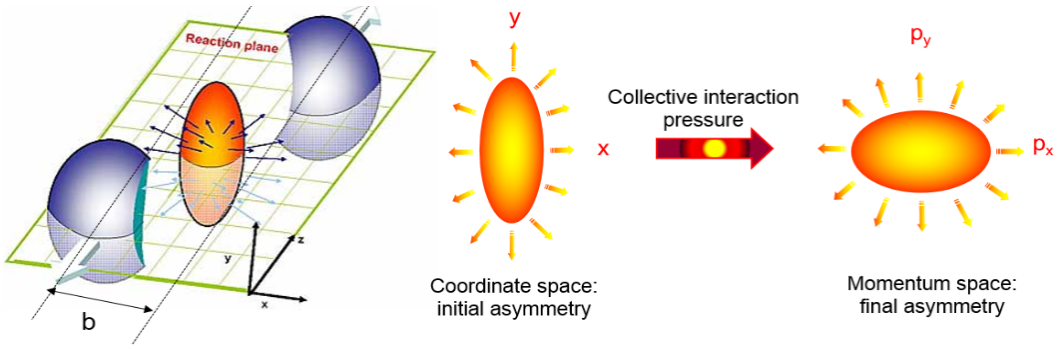

Figure 1.5: Conceptual drawing of a heavy-ion collision which describes the origin of the collective flow. Taken from Ref.[23].

The angular distribution of the final state particles can be written as:

$$\frac{dN}{d\phi} \propto 1 + 2\sum_{n=1}^{\infty} v_n \cos\left(n\left(\phi - \psi_n\right)\right) \tag{1.2}$$

where ϕ is the azimuthal angle, ψ_n is the reaction plane angle, n is the order of harmonic, and v is the flow coefficient. The v_2 is the second order coefficient, named elliptic flow, that points to the anisotropic geometry of the collision. Non-zero v_2 coefficient probes the spatial anisotropy of the final state particles.

1.3 Unexpected observations in small systems

As discussed in Sec.1.2.1, the production of strange hadrons is enhanced in AA collisions as a signature of the formation of the QGP. This is also true for the elliptic flow of charged particles, which points to the collective behavior of the particles formed in a deconfined state. Surprisingly, these and other behaviors have been observed in small systems, i.e., pp and pA collisions, particularly in high multiplicity events. In such systems, the energy-density and the temperature are not supposed to be large enough to create a QGP.

Strangeness enhancement in small systems: as discussed in Sec.1.2.1, the production of strange hadrons in AA collisions is enhanced relative to pp collisions. This effect was further investigated as a function of charged-particle multiplicity in smaller systems. Fig.1.6 presents the ratio of strange hadrons yield to pions as a function of charged-particle multiplicity. The plot compares the results obtained by the ALICE collaboration from pp at $\sqrt{s}$ = 7 TeV, p–Pb at $\sqrt{s_{\rm NN}}$ = 5.02 TeV, and Pb–Pb at $\sqrt{s_{\rm NN}}$ = 2.76 TeV depicted in closed circles, diamond, and square shapes, respectively [24, 25, 22]. The plot shows the ratios of the yields of four strange hadrons (K^0_s, Λ, Ξ, Ω) to the pion one as a function of charged-particle multiplicity measured at midrapidity. A clear smooth transition from pp to p–Pb, and to Pb–Pb collisions is observed for all the ratios. In addition, the ratios at high multiplicity events in pp collisions reach values comparable to those measured at low multiplicity of Pb–Pb collisions. The comparison to the calculations from MC models is also presented in the figure [26–28]. PYTHIA 8.2 and EPOS LHC event generator calculations describe the production of K^0_s, while they underestimate the results of the other particles.

Elliptic flow of charged particles in small systems: since it is hard to define the reaction plane in small systems, the two-particle angular correlation is the technique used to study the collective behavior of pp and pA collisions. The two-particle $\Delta\Phi$–$\Delta\eta$ correlation of charged particles in pp and pA collisions is dominated by the near-side jet peak structure at ($\Delta\Phi$, $\Delta\eta$) = (0,0), and by the away-side structure along the $\Delta\eta$-axis at $\Delta\Phi = \pi$. The distribution of the two-particle angular correlation of charged particles as a function of $\Delta\Phi$ and $\Delta\eta$

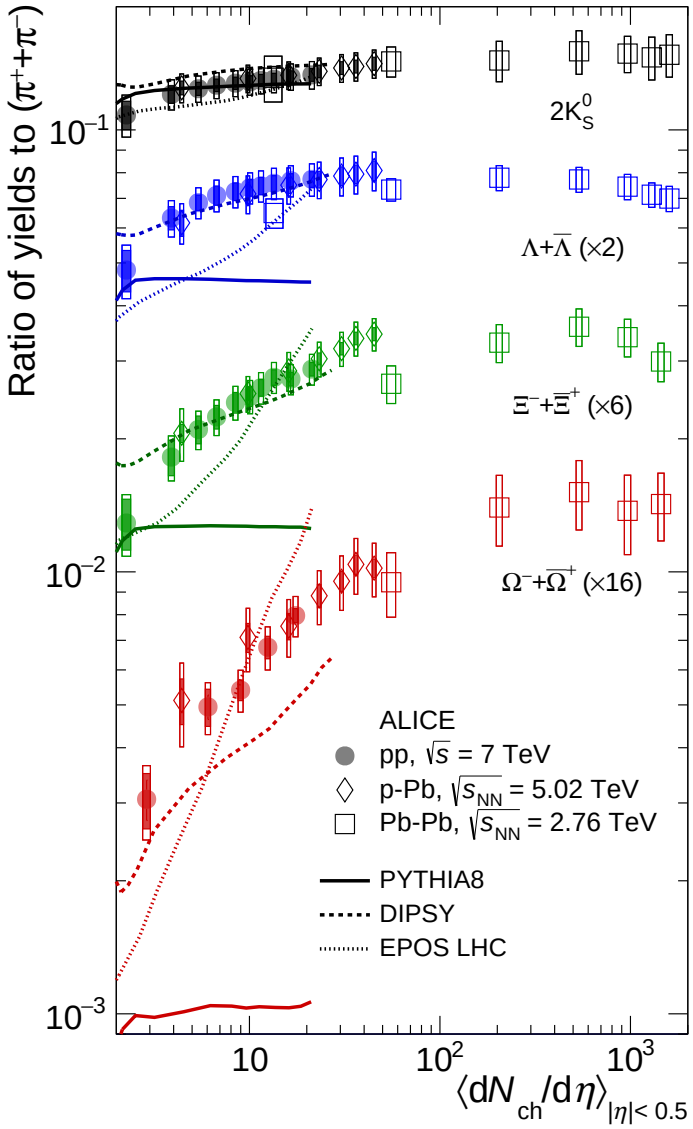

Figure 1.6: Ratios of strange to pion yields ($\pi^+\pi^-$) as a function of charged-particle multiplicity measured at midrapidity $|y| < 0.5$. The presented results are shown for pp, p–Pb, and Pb–Pb systems at $\sqrt{s} = 7$ TeV, $\sqrt{s_{\rm NN}} = 5.02$ TeV and $\sqrt{s_{\rm NN}} = 2.76$ TeV, respectively [24, 25, 22]. The results are compared to the calculations from PYTHIA8, DIPSY, and EPOS LHC [26–28].

is presented in Fig.1.7. The analysis is performed by CMS collaboration in p–Pb collisions at $\sqrt{s_{\mathrm{NN}}}$ = 5.02 TeV [29]. In the left panel of Fig.1.7, corresponding to the low multiplicity events (less than 35 tracks/event), both the near-side and the away-side structures are observed. However, the right panel, representing the high multiplicity of events (more than 110 tracks/event), reveals an additional long-range near-side structure in the two-particle correlation distribution. Such structure was expected to be only observed in AA collisions as it is interpreted as a signature of QGP creation. The origin of this behavior in small systems is yet to be fully understood. similar measurements for the two-particle angular correlation performed at the LHC for pp and p–Pb collisions can be found in the following references [30–32].

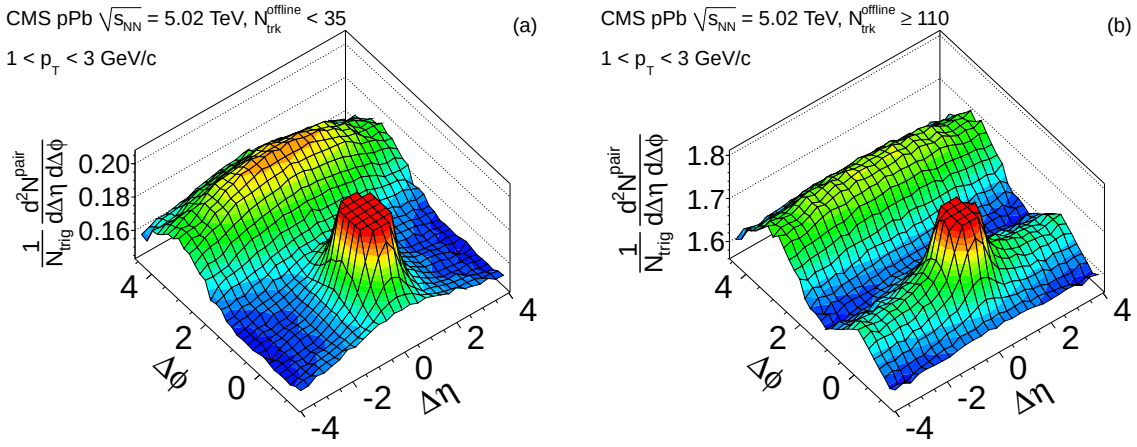

(a) (b)

Figure 1.7: 2D particle correlation in p–Pb collisions $\sqrt{s_{\mathrm{NN}}}$ = 5.02 TeV for pairs of charged-particles with $1 < p_{\mathrm{T}} < 3$ GeV/c for particles with multiplicity (a) $N_{trk} < 35$, (b) $N_{trk} \geq 110$ [29].

How to explain QGP-like behaviors in small systems: the origin of the QGP-like behaviors observed in small systems remains unclear. Such observables are typically interpreted as QGP signatures in AA collisions. Several interpretations have been proposed to understand these findings, such as the formation of QGP droplets or the influence of Multi-Parton Interactions (MPI). The QGP droplets refer to events with local high-density regions created in the high multiplicity events of pp or pA collisions. On the other hand, MPI are defined as several parton-parton interactions that take place in a single hadron-hadron collision. Due

to the composite nature of hadrons, it is possible to have multiple parton hard scatterings in a single pp collision at the LHC.

1.4 Charmonium production in small systems

Quarkonia are bound states of heavy quark and anti-quark pairs ($Q\bar{Q}$). Mesons made up of charm and anti-charm quarks are called charmonia ($c\bar{c}$), while those made up of bottom and anti-bottom quarks are called bottomonia ($b\bar{b}$). Quarkonia are excellent tools to study the QGP. Due to their heavy masses, they are produced in the initial stages of the collision, during the hard processes, and experience the full evolution of the created medium. In addition, their production is sensitive to both soft and hard QCD scales. In this thesis, we study J/ψ and $\psi(2S)$ production, which are the first and the second excited states of spin-1 charmonia, respectively.

1.4.1 Charmonia production mechanisms in pp collisions

Color Evaporation Model (CEM): CEM assumes that a heavy quark pair will hadronize into a quarkonium state if its invariant mass is below a threshold required to create the lightest open-heavy flavor pair. The model assumes that the color state of the pair at its hadronization is independent of that at its production. The production cross-section is expressed as:

$$\sigma_{\psi}^{CEM} = F_{\psi} \int_{2M_c}^{2M_D} \frac{d\sigma_{c\bar{c}}}{dm_{c\bar{c}}} dm_{c\bar{c}}, \tag{1.3}$$

where F_{ψ} is a phenomenological factor related to probability of the heavy quark pair hadronizing into a quarkonium state. One of the main limitations of this model is that it cannot describe the polarization observables for the charmonia production and some discrepancies in the transverse momentum spectra [33].

Color Singlet Model (CSM): CSM is based on the factorization approach to describe charmonium production [33]. The model separates the cross-section into perturbative parts related to the production of the heavy quark pair, and non-perturbative parts associated to the hadronization of the charmonium state. Hadronization is then described by a quarkonium wave function that is process and flavor independent. The cross-section is written as

follows:

$$d\sigma^{CSM}_{\psi+X} = \sum_{i,j} \int dx_i dx_j \, f_i(x_i,\mu_F) \, f_j(x_j,\mu_F) \times \mathrm{d}\hat{\sigma}_{i+j\to(Q\bar{Q})+X}(\mu_R,\mu_F) \times \langle|\psi(0)|^2\rangle \tag{1.4}$$

where $f_i(x_i,\mu_F)$ and $f_j(x_j,\mu_F)$ are the parton densities of the colliding hadrons, and $\mathrm{d}\hat{\sigma}_{i+j\to(Q\bar{Q})+X}$ is equivalent to the partonic cross section of a pair of heavy quarks with zero heavy-quark relative velocity ($v = 0$). $|\psi(0)|^2$ is the universal wave function. Unlike the CEM, CSM assumes that the final charmonium state is produced with the same quantum numbers as the heavy quark pair.

Color Octet Mechanism (COM) and Non-Relativistic QCD (NRQCD): COM+NRQCD includes aspects of both CEM and CSM [34]. This model is based on the factorization approach to describe the cross-section of the charmonium production as in the CSM. In addition, COM+NRQCD assumes that the quantum numbers (n) change between the production of the heavy quark pair and the hadronization process. In this model, the hadronization is described by the universal Long-Distance Matrix Elements (LDME) $\mathcal{O}^n_Q$. The cross-section is written as follows:

$$d\sigma^{NRQCD}_{\psi+X} = \sum_{i,j} \int dx_i dx_j \, f_i(x_i,\mu_F) f_j(x_j,\mu_F) \times \mathrm{d}\hat{\sigma}_{i+j\to(Q\bar{Q})_n+X}(\mu_R,\mu_F,\mu_\Lambda) \times \langle\mathcal{O}^n_Q\rangle \tag{1.5}$$

The LDMEs can be obtained by fitting experimental distributions, e.g., p_{T} spectra at different energies. The model allows the transition from color octet states to final physical mesons.

1.4.2 Cold nuclear matter effects

From a theoretical point of view, charmonium production in pA collisions is expected to be affected by several nuclear effects, the so-called Cold Nuclear Matter (CNM) effects.

Gluon (anti)shadowing: the parton distribution function represents the probability of finding a parton that carries a fraction x of the nucleon momentum at an energy scale Q^2. It is known that the parton distribution functions are modified in the nucleus compared to the proton. Early deep inelastic experiments revealed such an effect, suggesting that the measured nuclear effects are due to the modification of the parton distribution functions. The nuclear Parton Distribution Functions (nPDF) have a dependence on both x and Q^2. The modification of PDFs for a parton type i in a nucleus A can be expressed via the factor

R_i^A as:

$$R_i^A(x,Q^2) = \frac{f_i^A(x,Q^2)}{f_i(x,Q^2)}, \tag{1.6}$$

where f_i^A (f_i) is the parton distribution function of a parton type i in the nucleus (proton). Fig.1.8 presents the R_i^A factor as a function of x in the EPPS16 parametrization. The plot shows four distinct regions as a function of x:

- Shadowing which corresponds to the region $x \lesssim 10^{-2}$. This effect is described as a depletion in the nucleus compared to the proton. Shadowing can be explained by the recombination of low-x gluons in nuclei due to the high phase-space density, reducing the effective probability to find low-x gluons, and increasing the probability to find higher-x gluons (low-x gluons recombine into a higher-x one).
- Anti-shadowing points to the enhancement observed in the region $10^{-2} \lesssim x \lesssim 10^{-1}$. This enhancement is interpreted as a result of the increase of the gluon density due to the recombination of lower x gluons.
- European Muon Collaboration (EMC) effect, which dominates the region $10^{-1} \lesssim x < 1$. The origin of this effect is still unclear [35].
- Fermi motion, corresponds to an excess observed in the region of $x \to 1$. This effect is due to the non-stationary nucleons in the nucleus.

It is worth noting that the values of the transition points between the different regions are only rough estimates.

Gluon saturation: at low-x values, the gluon PDF shows an increase of the gluon density. The larger the energy, the larger the density is. When the gluon occupation reaches a maximum of $\sim 1/\alpha_s$, the density becomes very large, leading to a saturation of the partonic distribution [37, 38]. The framework where the saturation approach is employed is called Color Glass Condensate (CGC).

Fully coherent energy loss: the model assumes that the heavy quark pair is produced in a color octet state and remains in a color octet for much longer than the hard process time. During this time, and at any x_F (where x_F is defined as the longitudinal fraction momentum between the J/ψ and the projectile proton in pA collisions), the gluon radiation from the quarks is assumed to be soft. At sufficiently high energy, the quarkonium hard production process looks like a small angle scattering of color charges [39]. As discussed in Ref.[40],

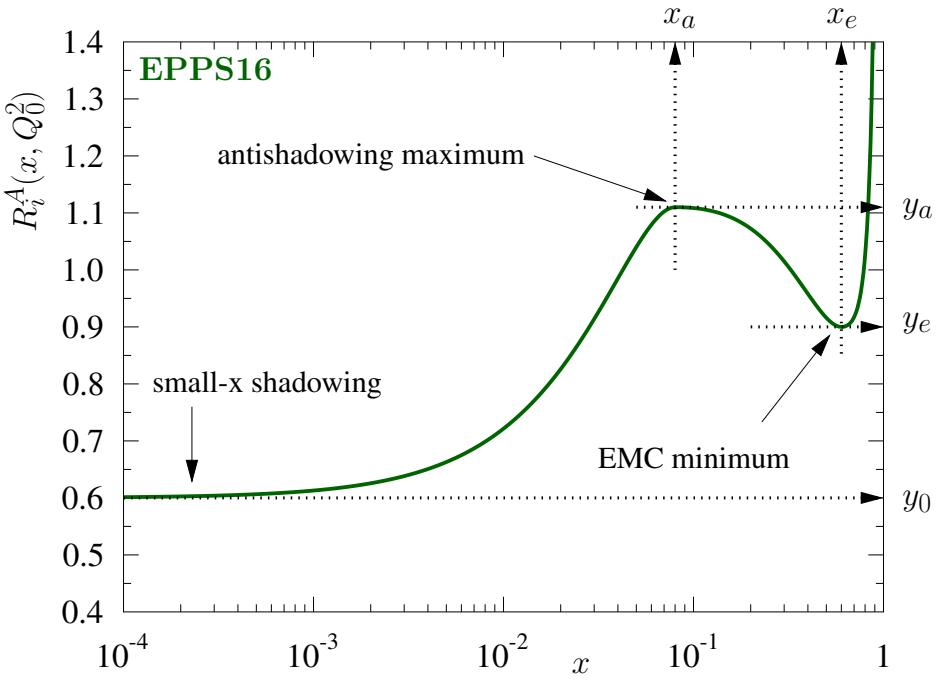

Figure 1.8: The x-dependence of the factor R in the EPPS16 parameterization [36].

quarkonia are expected to be suppressed at large x_F, or large rapidity, due to gluon radiation and the associated energy loss.

Comover: the comover framework considers the possibility for quarkonia to dissociate due to the interaction with the produced soft particles (the comovers) that travel along with the heavy-quark pair. In this model, the dissociation is stronger for quarkonium states with a larger size due to their weaker binding. Additionally, suppression is stronger where the comover density is larger. It is important to note that, besides the comover interaction, the model includes the shadowing effect in the calculation to describe the nuclear modification of the parton distribution functions in the nucleus [41].

Nuclear absorption: when a $c\bar{c}$ passes through a nuclear medium, it may undergo breakup of the heavy-quark pair due to the interaction with the primordial nucleus, the so-called nuclear absorption. This approach suggests that the time spent by the $c\bar{c}$ to pass through the nucleus is larger than charmonium formation time. As $\psi(2S)$ meson has a larger formation time than the J/ψ, it will be more suppressed due to the stronger break-up effect [42]. This effect is negligible at the LHC energies, as the charmonium formation time is expected to be larger than the nuclei crossing time.

1.4.3 Experimental results of charmonium production in pA collisions

In this section, we present selected experimental results on J/ψ and ψ(2S) production in p–Pb collisions performed by ALICE. We focus on the nuclear modification factor measurements ($R_{\rm pPb}$) in p–Pb collisions. The nuclear modification factor is an observable used to quantify the nuclear effects by evaluating the ratio of the production of a particle in pA collisions relative to its production in pp collisions properly normalized. $R_{\rm pA}$ can be evaluated as:

$$R_{pPb}(y_{\rm cms}, p_{\rm T}) = \frac{d^2\sigma^{\rm J/\psi}_{pPb}/dy_{\rm cms}dp_{\rm T}}{A_{Pb}\cdot d^2\sigma^{\rm J/\psi}_{pp}/dy_{\rm cms}dp_{\rm T}} \tag{1.7}$$

where the p–Pb production cross section is divided by the corresponding quantity for pp collisions, normalized by times the atomic mass number of the Pb nucleus ($A_{\rm Pb} = 208$).
Figure 1.9 presents the $R_{\rm pA}$ for the J/ψ yields measured in p–Pb collisions at $\sqrt{s_{\rm NN}} = 8.16$ TeV [43]. The $R_{\rm pA}$ in the backward rapidity region, -4.46 < $y_{\rm cms}$ < -2.96, is compatible with unity ($y = 1$) within uncertainties. At forward rapidity, 2.03 < $y_{\rm cms}$ < 3.53, the $R_{\rm pA}$ varies from 0.8 to 0.6, showing a clear suppression of J/ψ production in p–Pb collisions with respect to pp collisions. ALICE results are compatible, within uncertainties, with a similar measurement performed by the LHCb collaboration (depicted in blue in the same figure) [44]. Theoretical models based on shadowing fairly describe the results when nCTEQ15 [45] or EPPS16 [36] parametrization sets of nPDFs are adopted. EPS09NLO nPDF parametrization, which is also based on shadowing, shows a slightly worse agreement with the data at forward rapidity [46]. Moreover, models which include Color Glass Condensate (CGC) approach show a good agreement in their domain of validity [47, 48]. The parton coherent energy loss model describes quantitatively the results at both rapidity regions [49]. Finally, the calculations of the transport and the comover model, which include contributions from the interaction of the final state heavy-quark pair with the parton/hadron system, describe the results as well in the probed region [41, 50].
In Fig.1.10, the J/ψ and ψ(2S) nuclear modification factor in p–Pb collisions at $\sqrt{s_{\rm NN}} = 8.16$ TeV are compared. Both particles are reconstructed from their decay channel into dimuon in the muon spectrometer. A stronger suppression is observed for the ψ(2S) yields relative to the J/ψ in the backward rapidity region. At forward rapidity, both particles exhibit a similar suppression. The results are compared to the theoretical calculations from CGC+ICEM [48] and comover models [41]. The CGC+ICEM model describes fairly the observed suppression for both particles. Note that the CGC+ICEM calculations are only available at forward rapidity, corresponding to the low Bjorken-x values in the Pb nucleus. The comover model

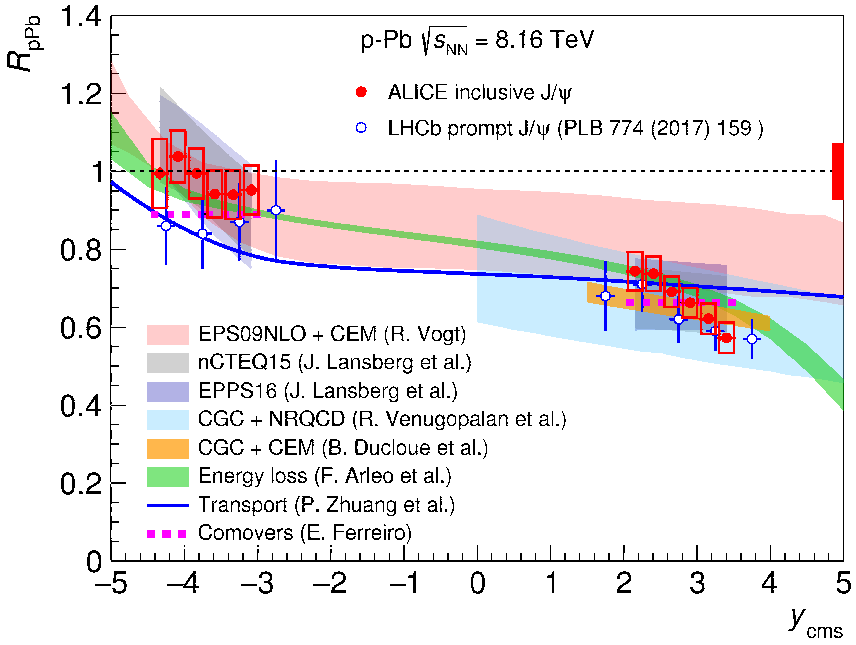

Figure 1.9: Comparison of the ALICE and LHCb [43, 44] results on the y_{cms}-dependence of the J/ψ nuclear modification factor in p–Pb collisions at $\sqrt{s_{NN}}$ = 8.16 TeV. The horizontal bars correspond to the bin size. For ALICE, the vertical error bars represent the statistical uncertainties, the boxes around the points the uncorrelated systematic uncertainties, and the filled box around unity the correlated uncertainties. For LHCb, the vertical error bars represent the combination of statistical and systematic uncertainties. The results are also compared to several model calculations [41, 51, 52, 47–50].

predicts a stronger suppression for the states with a larger size, i.e., a weaker binding. In the case of charmonia, it suggests a stronger suppression of $\psi(2S)$ relative to the J/ψ. Comover model calculations describe fairly the results of both J/ψ and $\psi(2S)$ at forward and backward rapidity.

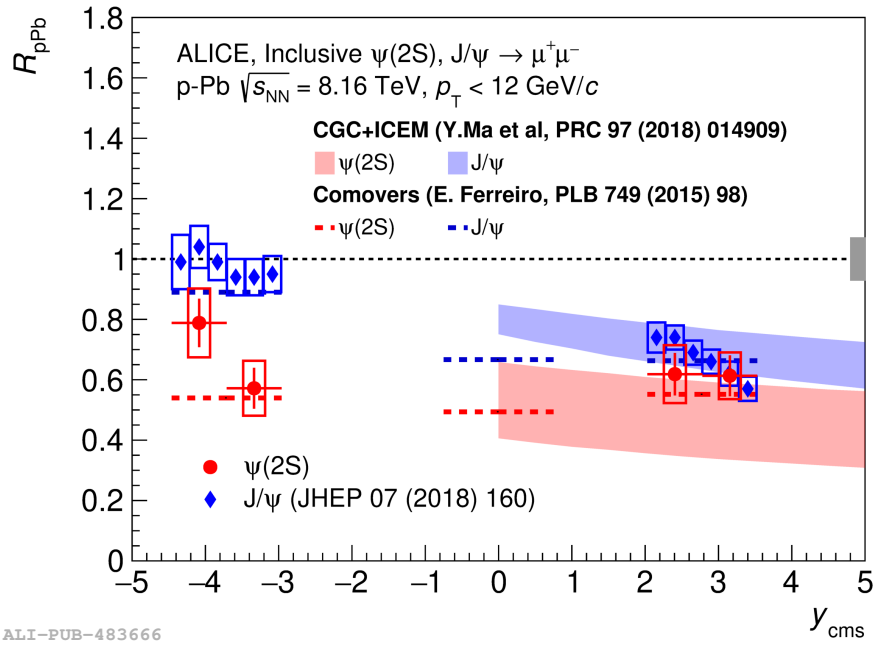

Figure 1.10: The nuclear modification factor of the $\psi(2S)$ and J/ψ production in p–Pb collisions at forward and backward rapidity regions [53]. The results are compared to the theoretical calculations from CGC+ICEM and comover models [47, 41]

In conclusion, the results of the nuclear modification factor of charmonium production in pA collisions were discussed. The observed behavior of R_{pA} is reproduced by several models considering different CNM effects. However, none of these models is favored by the data. More differential analyses are needed to understand which of the CNM effects plays a major role in charmonium production.

1.5 Quarkonium studies as a function of charged-particle multiplicity

The scrutiny of quarkonium yields as a function of the impact parameter of the collision, or the collision centrality, is a common and long standing practice in heavy-ion physics. The extension of these studies to small systems, i.e. pp and p–A, is limited due to the difficulty to determine the collision centrality in such cases, where the unknowns on the shape and

fluctuations of the initial geometry of the collision are important. The study of particle yields as a function of charged-particle multiplicity have emerged as an alternative to cope with such difficulties and to allow us to compare the results in all collision systems (from the small to the large ones). This section summarises the quarkonium studies as a function of charged-particle multiplicity at the LHC.

Figure 1.11 presents the results of the inclusive production of J/ψ yields as a function of charged-particle multiplicity, both measured at midrapidity ($|y| < 0.9$), in pp collisions at $\sqrt{s} = 13$ TeV [54]. In this study, the J/ψ yields and the charged-particle multiplicity are normalized to their average values obtained from the integrated multiplicity interval. The yields show a faster than a linear increase with increasing charged-particle multiplicity. This result is compared to several models attributing the observed behavior to different initial and/or final state effects. In particular, the trend of the data is described quantitatively by the coherent particle production model (CPP) [55], the color glass condensate model (CGC) [38], and the 3-Pomeron CGC model [56]. The percolation model describes the data trend up to at least four-to-five times the average multiplicity [57, 58], while EPOS3 [59] and PYTHIA 8.2 [26] event generators describe a faster than linear increase but not as strong as observed in the data.

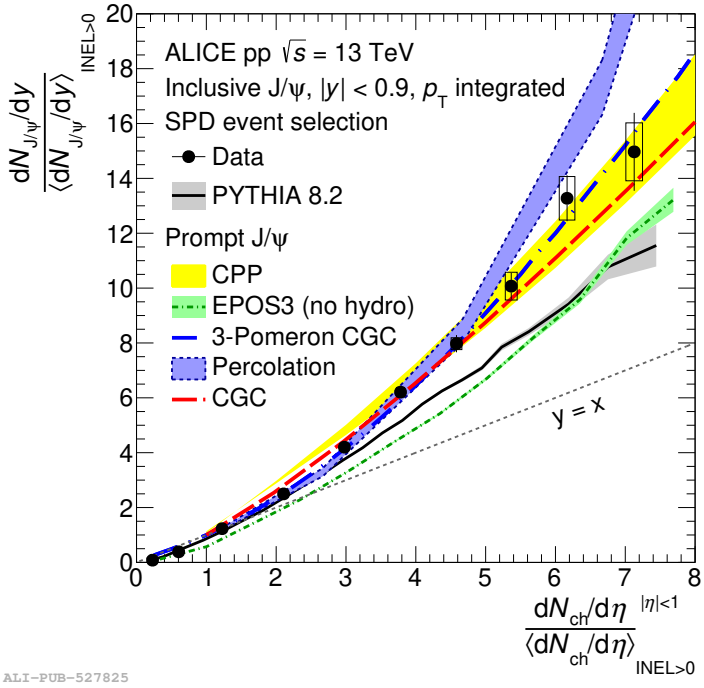

Figure 1.11: J/ψ self-normalized yields as a function of charged-particle multiplicity in pp collisions at $\sqrt{s} = 13$ TeV, both measured at midrapidity [54]. The results are compared with several theoretical models.

The comparison between forward and midrapidity J/ψ yields as a function of midrapidity charged-particle multiplicity in pp collisions at $\sqrt{s}$ = 13 TeV is reported in Ref.[60] (see also Fig. 4.8 in Sec. 4.2). The J/ψ self-normalized yields at forward rapidity also increase with charged-particle multiplicity, the increase is compatible with a linear trend within uncertainties. This increase is less rapid than that of the J/ψ measurement at midrapidity shown in Fig.1.11. The trend at forward rapidity is also described qualitatively by the theoretical computations of CPP, 3-pomeron CGC, percolation, and CGC+ICEM models, as well as EPOS3 and PYTHIA 8.2 event generators. One observes that most of model calculations expect such variation when studying J/ψ yields in different rapidity intervals. The CMS collaboration has investigated the multiplicity dependence of the production of a heavier quarkonium state, namely bottomonia, in pp and p–Pb collisions at different collision energies [61, 62]. Figure 1.12 presents the ratio of the excited to the ground state

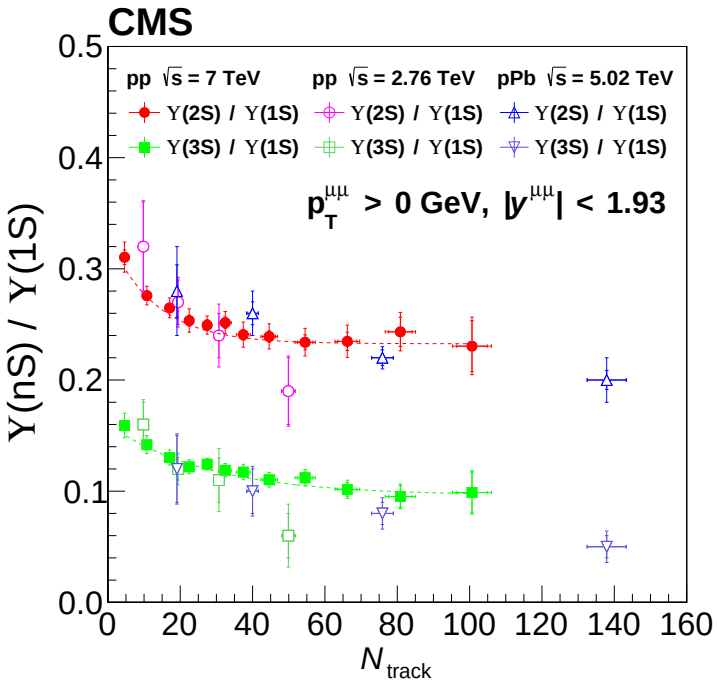

Figure 1.12: The ratios of the Υ(2S)-over-Υ(1S) and Υ(3S)-over-Υ(1S), with $p_T > 0$ GeV, as a function of the number of tracks (N_{track}) in various collision systems. The lines are fits to the data with an exponential function. The vertical error bars represent the combined statistical and systematic uncertainties on the bottomonia ratio, while the horizontal error bars represent the uncertainty on N_{track} [61, 62].

bottomonium yields as a function of the number of tracks (N_{track}). The Υ(2S)-over-Υ(1S) ratio shows a decrease as we move from the lowest to the highest multiplicity interval. A similar trend is observed for the results in pp collisions at $\sqrt{s}$ = 7 TeV and $\sqrt{s}$ = 2.76 TeV, as well as

for p–Pb results at $\sqrt{s_{\rm NN}}$ = 5.02 TeV. The same behavior is observed for the Υ(3S)-over-Υ(1S) as a function of $N_{\rm tracks}$. It is worth mentioning that the CMS measurement cannot be directly compared to the charmonium measurements carried out by the ALICE collaboration, as the multiplicity estimator is different in the two measurements. Additionally, in the CMS results, the bottomonium yields and the number of tracks are not normalized to their average value, as is done in charmonia results from the ALICE collaboration. Despite the caveats, the ALICE and CMS results are consistent within the limited measurement precision.
Several nuclear effects may affect the production of hadrons in pA collisions compared to pp collisions, as discussed in Sec. 1.4.2. To understand the influence of the nuclear environment on quarkonium production, ALICE measured the J/ψ normalized yields as a function of charged-particle multiplicity in p–Pb collisions at $\sqrt{s_{\rm NN}}$ = 8.16 TeV [63]. The J/ψ yields show an increasing trend with increasing multiplicity at both forward and backward rapidity as presented in Fig.1.13. For the yields reconstructed at backward rapidity, this increase is faster than a linear with increasing multiplicity. While the yields reconstructed at forward rapidity exhibit a slower than a linear increase with increasing multiplicity. In this study, the measurement is sensitive to multiple parton interactions and multiple nucleon-nucleon interactions, in addition to the cold nuclear matter effects which are expected to play a role in p–Pb collisions due to the presence of the heavy nuclei. The results are described by EPOS3 [59] calculation. However, it remains unclear which is the dominant effect at the origin of the differences observed when studying quarkonium production at various rapidity intervals.

1.6 Motivation of this thesis

This thesis focuses on the production of the excited charmonium state ψ(2S) as a function of charged-particle multiplicity in p–Pb collisions at $\sqrt{s_{\rm NN}}$ = 8.16 TeV. The ψ(2S) production yields are studied and compared to those of the ground state J/ψ. As mentioned in Sec. 1.5, these studies represent an alternative to look at particle production as a function of the collision impact parameter or the collision centrality, and to compare the results in all collision systems (from pp up to A–A collisions). The results are sensitive to multiple parton interactions, multiple nucleon interactions, and the influence of cold nuclear matter effects. In particular, the measurements reported in this thesis bring additional information on the role of final state effects at play in p–Pb collisions, as the role of initial state effects is expected to be similar for ground and excited quarkonium states. Therefore, in the ratio of the excited-to-ground state quarkonium yields initial state effects are expected to cancel.

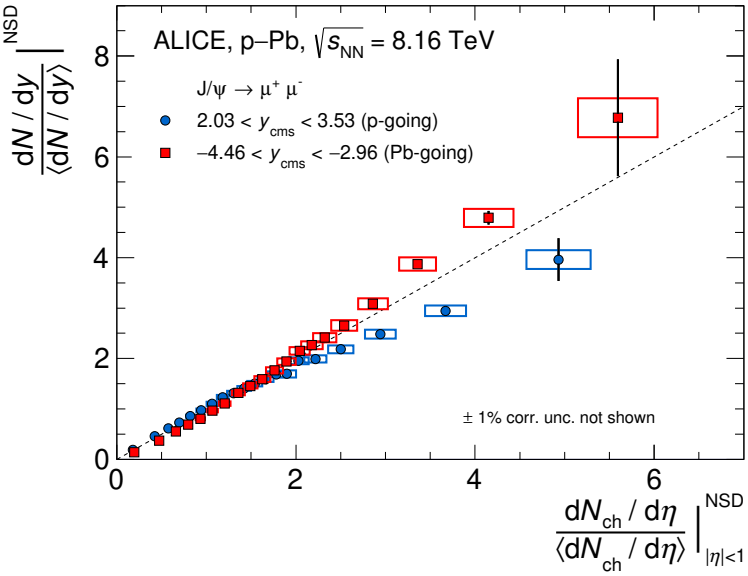

Figure 1.13: Self-normalised J/ψ yields as a function of midrapidity charged-particle multiplicity in p–Pb collisions at $\sqrt{s_{NN}}$ = 8.16 TeV [63]. The results at forward (backward) rapidity are represented by blue (red) points in the figure. The vertical lines represent statistical uncertainties, while the boxes depict the systematic uncertainties. The dashed line represents the one-to-one correlation to guide the eye.

The experimental setup is introduced in chapter 2, the analysis details are described in chapter 3, whereas the results are presented and discussed in chapter 4.

Part II

ALICE Run 2

2

A Large Ion Collider Experiment (ALICE)

In this chapter, we present an overview of the ALICE experiment at the LHC. In Sec.2.1, we introduce the Large Hadron Collider (LHC) and discuss the particle acceleration process. In Sec.2.2, we present the sub-detectors used to perform the analysis.

2.1 The Large Hadron Collider

The Large Hadron Collider (LHC) is the largest and the most powerful particle collider ever built [64]. The LHC is operated by the European Council for Nuclear Research (CERN)[1], and is located at the Swiss-French border. The LHC accelerates hadrons, such as protons and lead ions, to nearly the speed of light, making them collide at a center-of-mass energy of up to $\sqrt{s} = 13$ TeV in pp collisions. The full acceleration process involves a series of interconnected linear and circular accelerators. Each accelerator boosts the particles up to the highest energy they should achieve before injecting them into the next accelerator in the sequence. The CERN accelerator complex is schematically depicted in Fig.2.1, which includes the LINAC3 and the LINAC4 as sources of the beams, as well as the Booster and the Proton Synchrotron (PS). The LINAC4 accelerates negative hydrogen ions up to 160 MeV, and prepares them to be injected into the PS Booster. Before being injected into the PS Booster, the ions are stripped of their two electrons. The PS Booster, which consists of four superimposed synchrotron rings, accelerates the protons up to 2 GeV and injects them into

[1]The acronym CERN was defined for the French appellation for Conseil Européen pour la Recherche Nucléaire.

the PS, where they receive further acceleration to reach energies of up to 26 GeV. Protons are then injected into the Super Proton Synchrotron (SPS), where they are accelerated up to 450 GeV, and transferred to the two beam pipes of the LHC.

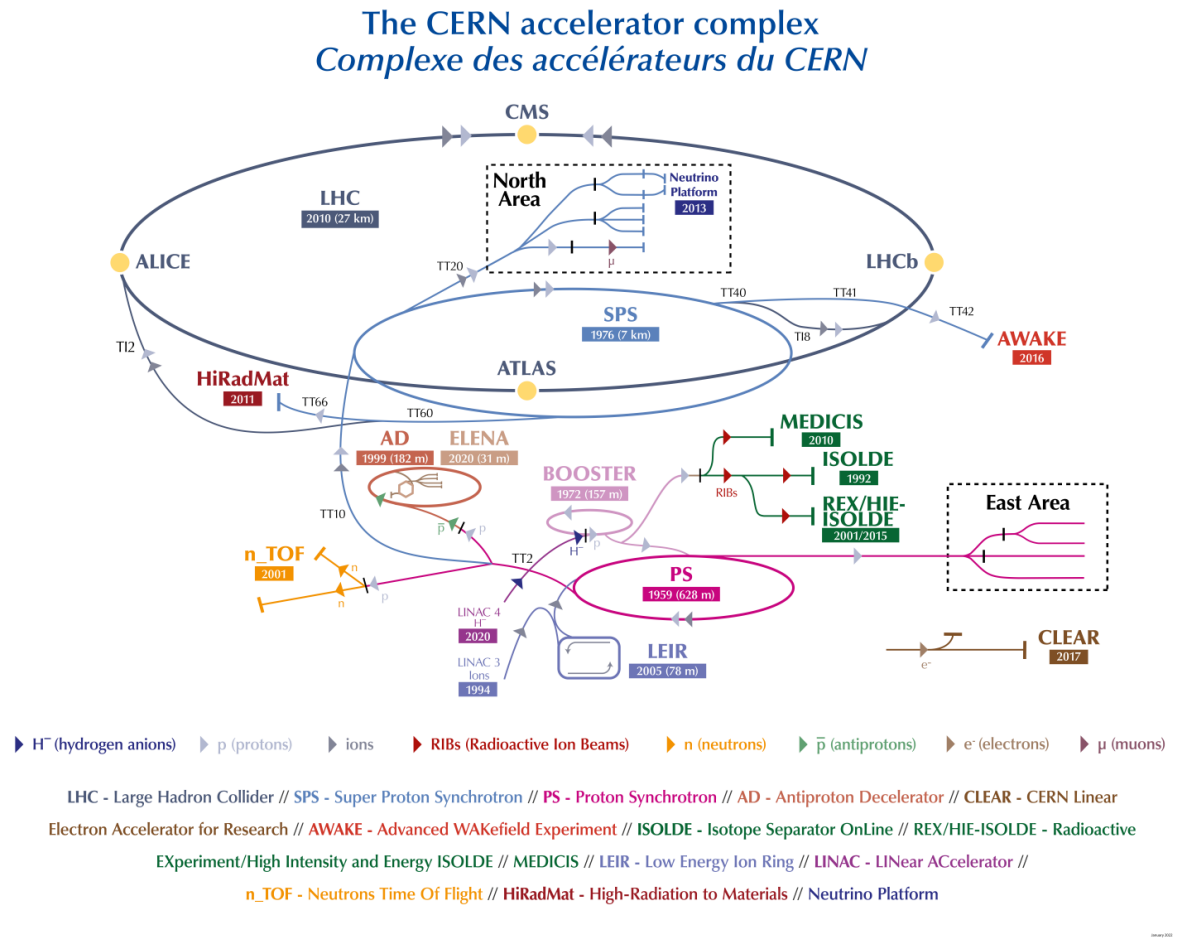

Figure 2.1: The CERN accelerator complex.

In the case of lead ions, the acceleration process starts at the LINAC3. The LINAC3 uses radiofrequency cavities to charge cylindrical conductors where the lead ions pass. As the ions move through these conductors, which are alternately charged with positive and negative charges, they are accelerated. The resulting accelerated ions are then injected into the Low Energy Ion Ring (LEIR), where they are gathered into dense bunches and further accelerated for injection into the PS. The PS accelerates both the protons injected from the PS Booster or lead ions injected from the LEIR. The ions are then injected into the SPS, which operates up to 450 GeV. The SPS accelerates the bunches and injects them as trains of bunches into the LHC ring. In the LHC ring, the beams travel in opposite directions in two separated beam

pipes and are made to collide at four interaction points around the LHC ring. These four points correspond to the location of the four main experiments at the LHC: ALICE, ATLAS, LHCb, and CMS. A Large Ion Collider Experiment (ALICE) [65, 66] is a heavy-ion dedicated experiment at the LHC. It is designed to study the physics of strongly interacting matter at extreme energy densities. ALICE is described in detail in Sec.2.2. A Toroidal LHC Apparatus (ATLAS) [67] and the Compact Muon Spectrometer (CMS) [68] are multipurpose detectors that scrutinize the largest range of physics possible at the LHC. The Large Hadron Collider beauty experiment (LHCb) [69] studies the difference between matter and anti-matter by studying b-quark physics.

2.2 ALICE experiment

ALICE consists of 19 sub-detectors, which allow for studying a broad range of observables. These sub-detectors can be classified into three main categories. First, the forward detectors measure general quantities such as particle multiplicity, luminosity, and collision's centrality. Second, central barrel detectors at mid-rapidity are important for reconstructing and identifying the trajectories of charged hadrons, photons, and electrons. Third, the muon spectrometer, at forward rapidity, reconstructs and identifies muons. The muon spectrometer aims to measure the production of heavy quark resonances, open heavy flavor decays, and Z-bosons down to zero transverse momentum (p_{T}). Fig.2.2 presents the sub-detectors of ALICE during the Run 2 data-taking period. Only the main sub-detectors are outlined in the following subsections.

2.2.1 Central detectors

Inner Tracking System (ITS)

The ITS consists of six cylindrical layers of silicon detectors [70]. The layers are located at radii ranges between 4 and 43 cm, covering a pseudorapidity range of $|\eta|< 0.9$. To achieve the required resolution and cope with the high particle density expected in heavy-ion collisions, different technologies are used to design the different ITS layers. Specifically, the two innermost layers use silicon pixel detectors (SPD), the following two layers use silicon drift detectors (SDD), and the outer two layers are equipped with double-sided microstrip detectors (SSD) as they face a low particle density. The SDD and SSD layers are equipped with analog readout so that they can be used to measure the energy loss for low-p_{T} reconstructed particles. The inner tracking system contributes to the majority of the physics topics

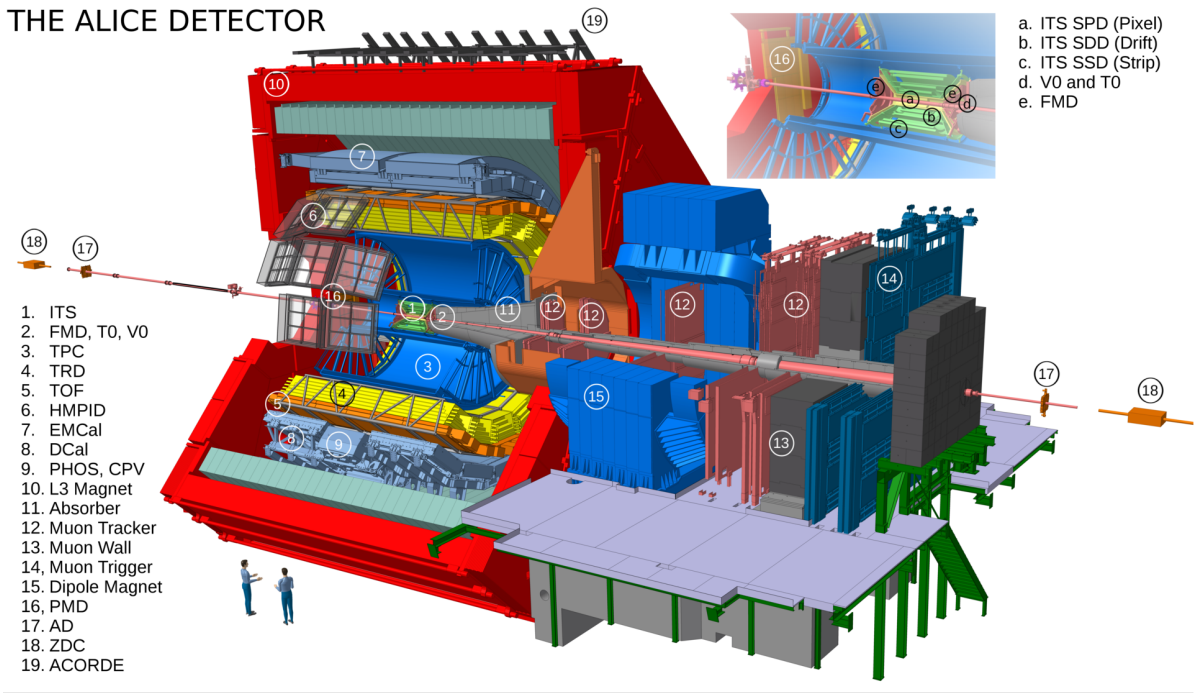

Figure 2.2: ALICE detector schematic during Run 2, superimposed a zoom-in of the region close to the interaction point.

addressed by the ALICE experiment as discussed in the physics performance report [71]. The main tasks of the ITS are to reconstruct the primary vertex with a resolution of at least 100 μm, to localize the secondary vertices for the decay of D and B hadrons, to track charged particles with $p_{\mathrm{T}} < 200$ MeV/c, and to improve the momentum and resolution of particles reconstructed by the Time Projection Chamber. In this thesis, we are exploiting the SPD detector to reconstruct the primary vertex and measure the charged-particle multiplicity.

Time Projection Chamber (TPC)

The TPC is a large cylindrical field cage with an inner radius of 85 cm and an outer radius of 250 cm [72]. The detector has an active volume of 90 m^3 filled with Ne/CO_2/N_2. The volume of the TPC is separated by an electrode in the middle. The TPC is the main tracking system of the central barrel. It is used for particle identification and to track and measure charged-particle momentum.

2.2.2 Forward detectors

Zero Degree Calorimeter (ZDC)

The ZDC consists of two sets of hadronic calorimeters, ZP and ZN, optimized to measure the spectator protons and neutrons, respectively [73]. The spectator protons are separated from the interaction beam by means of the dipole magnet, while the spectator neutrons are moving at zero degrees. Therefore, the ZN is located at zero degrees with respect to the beam pipe, and the ZP is located externally to the outgoing beam pipe on the side where positive protons are deflected. The hadronic calorimeters are quartz-fiber calorimeters with silica optical fibers as active material embedded in a dense absorber and located along the beam pipe at a $z = \pm 116$ m from the interaction point. The hadronic calorimeters are completed by two Zero Electromagnetic calorimeters (ZEM) located at $z = \pm 7$ m. The ZP and ZN measure the energy deposited by the spectator neutrons and protons, which provide information about the collision geometry. The smaller number of spectators, the more central the collision is. On the other hand, the ZEM mainly measures the energy deposit of photons emitted at forward rapidity. In this thesis, the information from the ZDC is used to reject background events from beam-gas interactions.

V0 detector

The V0 detector comprises two arrays of plastic scintillators, V0-A, and V0-C, placed at either side of the interaction point at $z = 329$ cm and -86 cm, respectively [74]. Each V0 ring is segmented into four rings in the radial direction, and each ring is divided into eight sections in the azimuthal direction. The V0 detectors cover the pseudorapidity regions of $2.8 < \eta < 5.1$ and $-3.7 < \eta < -1.7$. The V0 has different functionalities. It serves as a minimum bias trigger. In addition, the V0 detector serves as centrality estimator by measuring the multiplicity of the particles, as well as to measure the charged-particle multiplicity, to determine the collision event plane, and to reject background events from beam-gas interactions. In the analysis of this thesis, the V0 detector serves as a MB trigger and to reject beam-gas events.

2.2.3 Muon Spectrometer

The Muon Spectrometer is designed to reconstruct quarkonia, i.e., J/ψ, ψ(2S) and Υ(nS), as well as ϕ, and heavy-flavor decays, in their decay channel into dimuon with the highest possible accuracy and down to zero p_{T} [75]. The spectrometer triggers and reconstructs the trajectory of muons in the pseudorapidity window $-4 < \eta < -2.5$. Fig.2.3 presents the main

parts of the spectrometer. It consists of the following sub-detectors: a front absorber needed to reduce the flux of hadrons and photons at large rapidity, ten planes of muon tracking chambers, a muon filter required to reduce the fake muon tracks, followed by four planes of trigger chambers. In this thesis, the information from the Muon Spectrometer is exploited to reconstruct the charmonium yields.

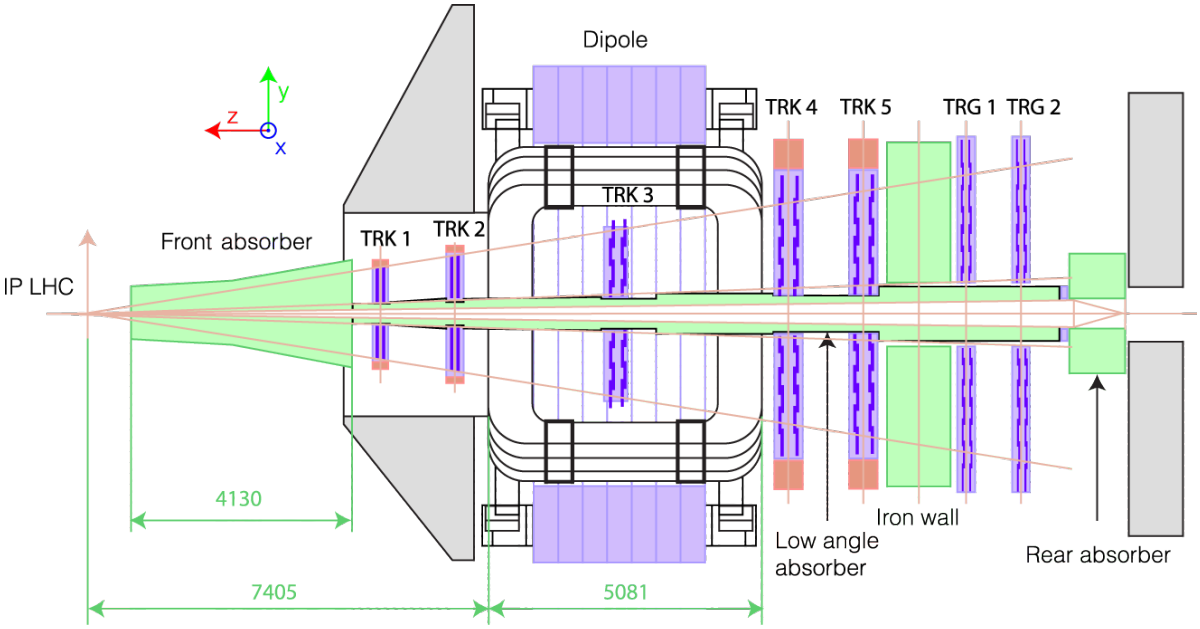

Figure 2.3: The ALICE muon spectrometer. The figure shows the absorbers, the tracking, and the trigger systems. The red lines depicted in the figure define the muon spectrometer acceptance [76].

Absorbers

The front passive absorber is the closest part of the muon spectrometer to the interaction point and is located inside the solenoid magnet. The absorber is made of carbon and concrete, which helps to limit multiple scattering and energy loss experienced by traversing muons. Moreover, the absorber protects the other ALICE detectors from the secondary interactions that occur within the absorbing material. The spectrometer is shielded throughout its length by an inner beam shield, which is made of tungsten, lead, and stainless steel. This shield is required to minimize the background from primary particles produced in the collisions and their decay products produced in the beam pipe and the shield itself. In order to have additional protection for the trigger chambers, a 1.2 m iron wall, the muon filter, is placed in front of the first station of the trigger chambers. The front absorber and the filter wall combined stop muons with total momentum of less than 4 GeV/c.

Tracking system

The muon tracking (MCH) system is located after the front absorber. It comprises five stations, with two detection planes each, consisting of 4.2 and 5 mm gas gap Multi-Wire Proportional Chambers (MWPC) called cathode pad chambers. The first two stations are placed before the dipole magnet. They consist of four detection planes of quadrant-designed cathode pad chambers. The third station is placed inside the dipole magnet, while the fourth and fifth stations are located after the dipole magnet. The cathode pad chambers of the last three stations have a rectangular shape design called slats. A schematic view of the quadrant and slat structures is presented in Fig.2.4. The main requirement of the tracking system is to track the muons with a minimum spatial resolution of 100 μm necessary to reconstruct Υ with an invariant mass resolution of 100 MeV/c^2. In addition, it is required to operate with high efficiency at the maximum hit density of about 5×10^{-2} expected in central Pb–Pb collisions.

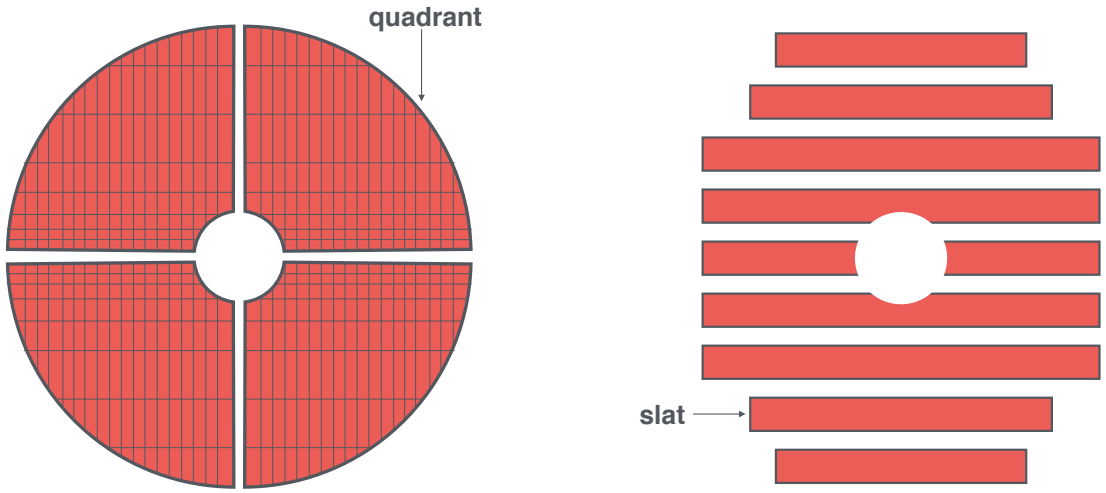

Figure 2.4: A schematic view of the quadrant and slat structures.

The MWPCs operate on the principle of gas ionization and electron amplification. The detector comprises a set of parallel and equally spaced anode wires placed between two cathode planes. The anode wires have a high voltage ~ 1650 V, while the cathode planes are connected to the ground. This develops an electric field with the maximum being at the wire surface. The volume between the two cathodes is filled with Ar+CO_2 gas. Fig.2.5

presents a schematic cross-section of the MWPC structure. When a charged particle crosses the detector, it ionizes the gas. The electric field drifts the freed electrons toward the anode wires, generating a cascade of secondary electrons. This induces a charge distribution on the cathode pads near the avalanche.

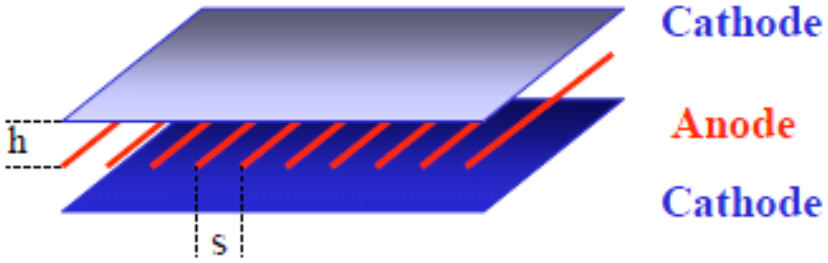

Figure 2.5: Schematic cross section of a MWPC.

Trigger system

The muon trigger (MTR) system is located behind the muon iron filter, at about 16 m from the interaction point. It consists of four planes of Resistive Plate Chambers (RPC) grouped in two stations (labeled TRG1 and TRG2 on Fig. 2.3), one meter apart from each other. The RPCs are made of low-resistivity bakelite electrodes, an anode, and a cathode. The electrodes are coated with linseed oil necessary to improve the smoothness of their surfaces. They are separated by a 2 mm gap filled with gas. The role of MTR is to select events containing muons from quarkonia, heavy-flavors or electro-weak bosons decays. Since the background is mostly composed of low-p_{T} muons from pions and kaons decays, the selection is based on an online estimate of the p_{T} of the reconstructed tracks. The trigger algorithm principle is depicted in Figure 2.6. It begins by reconstructing the (x, y, z) position of the muon track in the first MTR station. This reconstructed track is then projected into the second station. Next, the algorithm calculates the y deviation (δy) of the reconstructed track from a hypothetical track with infinite momentum that crosses the first trigger station at the same y coordinate. The value of δy is inversely proportional to the p_{T} of the reconstructed track. Two programmable thresholds (low and high p_{T}) are embedded in the trigger readout electronics. The values of the p_{T} thresholds range between $\sim$ 0.5 to $\sim$ 2 GeV/c and are combined with the sign of the track to provide MTR inputs to ALICE Central Trigger Processor. These inputs can also be combined logically to compose like-sign or unlike-sign dimuon triggers, which are of prime importance in the following analysis.

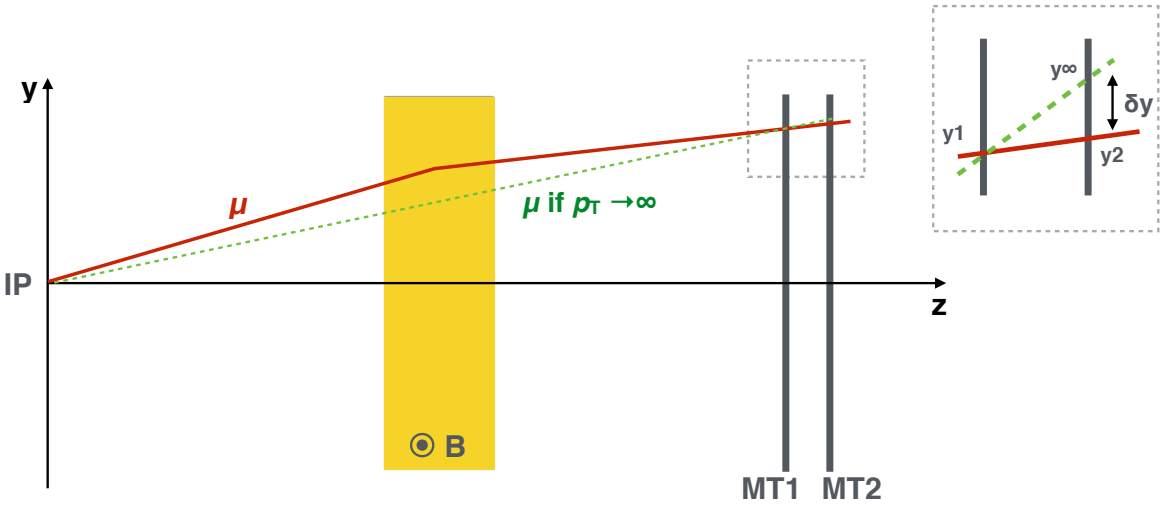

Figure 2.6: Working principle of the muon trigger system algorithm to estimate the tracks p_T (figure from Ref.[77]).

3

Multiplicity determination and charmonium production analysis

In this chapter, we present the step-by-step procedure to extract and evaluate the self-normalized charmonium yields as a function of the self-normalized charged-particle multiplicity. In Sec.3.1, we define the observables studied in this chapter. In Sec.3.2, we present the analyzed data sample and the event and track selections. In Sec.3.3, we discuss the methodology used to evaluate the charged-particle multiplicity and its associated uncertainty. In Sec.3.4, we explain the fit procedure followed to extract the raw charmonium yields and relative yields, as well as the ratio of the excited-to-ground state yields ratio. In Sec.3.5, we discuss the corrections applied to the raw yields to obtain the self-normalized charmonium yields. Finally, in Sec.3.6, we report the different sources of systematic uncertainties on the self-normalized charmonium yields.

3.1 Observable definition

The analysis is performed in the non-single diffractive event class (NSD). The non-single diffractive class is defined as the sum of non-diffractive, diffractive, and double diffractive events in the collision. In a single-diffractive collision, only one of the beam particles breaks up and produces particles at large rapidity on one side of the detector. Two observables are discussed in this chapter to obtain the final physics results. The first one is the self-

normalized charged-particle multiplicity. In this analysis, the number of tracklets, or track segments ($N_{\rm tr}$), reconstructed by joining pairs of hits in the SPD layers in the rapidity range $|y_{lab}| < 1$, serves as charged-particle multiplicity estimator. We assume that the number of tracklets is proportional to the number of charged particles ($\mathrm{dN_{ch}/d}\eta$) as follows:

$$\frac{dN_{ch}}{d\eta} \propto \frac{N_{\rm tr}}{\Delta\eta}, \tag{3.1}$$

we obtain the proportionality factor from Monte Carlo (MC) simulations. Then, the self-normalized charged-particle multiplicity can be calculated as follows:

$$\left(\frac{dN_{ch}/d\eta}{<dN_{ch}/d\eta>}\right)^{i} \propto \frac{1}{\Delta\eta}\frac{<N_{\rm tr}^{i}>}{<dN_{ch}/d\eta>}, \tag{3.2}$$

where $<dN_{ch}/d\eta>$ is the average number of the charged particles in the NSD event class, and the superscript i denotes the charged-particle multiplicity interval.
The second observable discussed in this chapter is the self-normalized charmonium yields. The yields of the charmonium ground state (J/ψ) and its radial excited state (ψ(2S)) are extracted from the fit to the dimuon invariant mass spectrum. The measurement is performed for both the integrated sample, and for multiple intervals of charged-particle multiplicity. The raw yields are then corrected to obtain the self-normalized charmonium yields as follows:

$$\left(\frac{\mathrm{d}N/\mathrm{d}y}{\langle \mathrm{d}N/\mathrm{d}y\rangle}\right)^{i} = \frac{N^{i}}{N}\frac{N_{\rm MB}^{\rm eq}}{N_{\rm MB}^{i,\rm eq}}\frac{(A\epsilon)}{(A\epsilon)^{i}}\frac{\epsilon_{\rm MB}^{i}}{\epsilon_{\rm MB}}, \tag{3.3}$$

where N is the raw yield of the charmonia (either J/ψ or ψ(2S)), $N_{\rm MB}^{\rm eq}$ is the number of equivalent minimum bias (MB) events corresponding to the analyzed data sample, $A\epsilon$ is the detector acceptance times efficiency, and $\epsilon_{\rm MB}$ is the efficiency of the minimum bias trigger to select the event class of the analyzed data sample. Whenever the quantity is marked with the index i, it refers to the value in each charged-particle multiplicity interval i; otherwise, it refers to the multiplicity integrated quantity.

3.2 Data sample and event and track selection

The analysis of the multiplicity dependence of charmonium production is performed in p–Pb collisions, at center-of-mass energy per nucleon pair of $\sqrt{s_{\rm NN}}$ = 8.16 TeV. Data was collected during November and December 2016 by the ALICE experiment at the CERN LHC. The asymmetry of the p–Pb collisions leads to a shift in the center-of-mass rapidity ($y_{\rm cms}$)

with respect to the laboratory frame (y_{lab}). This shift (Δy) depends on the charges (Z_1, Z_2) and the atomic numbers (A_1, A_2) of the colliding particles, and can be computed as follows:

$$\Delta y = \frac{1}{2} \ln\left(\frac{Z_1 A_2}{Z_2 A_1}\right), \tag{3.4}$$

which results in $\Delta y = \pm 0.465$ for p–Pb collisions. Two beam configurations are defined due to the rapidity shift for p–Pb collisions:

- the forward rapidity region refers to the scenario in which the proton beam is directed from the interaction point (IP) towards the muon spectrometer. In this configuration, the center-of-mass rapidity range covered by the muon spectrometer is $2.03 < y_{\text{cms}} < 3.53$.
- the backward rapidity region refers to the situation in which the lead beam is directed from the IP towards the muon spectrometer. In this configuration, the center-of-mass rapidity range covered by the muon spectrometer is $-4.46 < y_{\text{cms}} < -2.96$.

A scheme of the two configurations for p–Pb collisions is depicted in Fig.3.1.

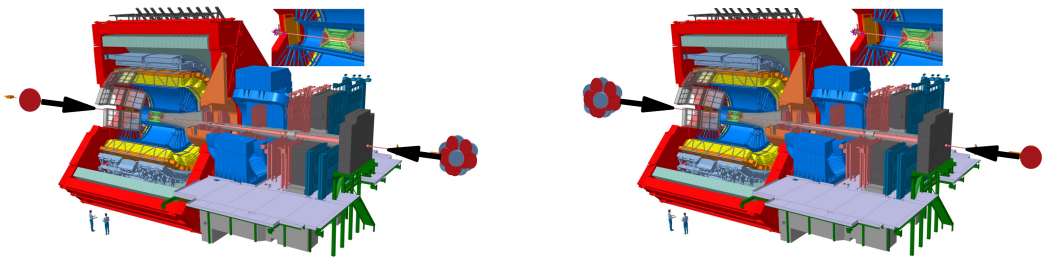

(a) Forward rapidity ($2.03 < y_{\text{cms}} < 3.53$) (b) Backward rapidity ($-4.46 < y_{\text{cms}} < -2.96$)

Figure 3.1: Schemes of the two configurations for p–Pb collisions. On the left is the forward rapidity configuration, where the proton beam is directed towards the muon spectrometer. On the right panel, the backward rapidity configuration, in which the lead beam is directed towards the muon spectrometer.

Two data sets are used in this analysis, one per collision configuration, to extract the charmonium raw yields. The data collected from the forward and the backward configurations were named in the ALICE internal scheme as LHC16r and LHC16s, respectively. Each data sample is subdivided in different *runs*, corresponding to a limited period of time. The full list of the *run numbers* analyzed for each data set can be found in Appendix A.

3.2.1 Event selection

The charmonium yields are measured using the dimuon triggered data sample, while the charged-particle multiplicity is evaluated using the MB triggered data sample. The following trigger classes are utilized to perform the measurement:

- **CINT7-B-NOPF-MUFAST** (CINT7-MUFAST) is a MB trigger that requires a signal coincidence in the V0A and V0C detectors. We use this trigger class to evaluate the charged-particle multiplicity.
- **CINT7-B-NOPF-CENT** (CINT7-CENT) is also a MB trigger that requires a signal coincidence in the V0A and V0C detectors. This trigger class is used to evaluate the normalization factor correction for the charmonium yield measurement.
- **CMSL7-B-NOPF-MUFAST** (CMSL7) is a single muon low p_{T} trigger. It requires the detection of at least one muon having an online $p_{\mathrm{T}}^{\mu} \gtrsim 0.5$ GeV/c in coincidence with a signal in the V0A and V0C detectors. This trigger is used to evaluate the normalization factor correction for the charmonium yields.
- **CMUL7-B-NOPF-MUFAST** (CMUL7) is a dimuon low p_{T} trigger cut. It requires the detection of two muons of opposite charge having both an online $p_{\mathrm{T}}^{\mu} \gtrsim 0.5$ GeV/c in coincidence with a signal in the V0A and V0C detectors. This trigger is used to extract the charmonium raw yields.

The ALICE physics offline selection removes background contamination from beam-gas or beam-collider interaction events. Additionally, this selection allows the application of a set of predefined cuts that removes the pile-up events from the data sample. However, the pile-up rejection criteria are customized for MB events rather than the dimuon-triggered events. Since the muon tracks reconstructed in the muon spectrometer originate from the initial hard scattering events, these events usually produce more charged particles than the MB events. As a result, the rejection criteria may remove many good events in the dimuon-triggered sample. Consequently, the offline physics selections are modified to avoid removing good high multiplicity events in the p–Pb multiplicity-dependent analysis.

SPD pile-up selection criteria

The ALICE pile-up selection algorithm is based on identifying the main vertex in the SPD detector for a single event and then looping over all the other vertices corresponding to the same event. The algorithm criteria defines a threshold distance between the two vertices (d),

and a minimum number of contributing tracklets per vertex ($N_{\text{contributors}}$) to find the vertices. In the default case, if two vertices are found within a distance $d > 0.8$ cm and have at least $N_{\text{contributors}} > 3$, the event is identified as a pile-up event and rejected from the analysis. In the p–Pb multiplicity dependent analysis, the rejection depends on the number of tracklets produced in the event. For the events with fewer tracklets than 50, the events with two vertices found within a distance $d > 0.6$ cm and $N_{\text{contributors}} > 3$ are rejected. For the events with a number of tracklets larger than 50, the rejection is done if two vertices are found within a distance $d > 0.8$ cm and $N_{\text{contributors}} > 5$.

Correlation between the number of clusters and number of tracklets

A customized cut is applied to the correlation between the number of clusters (N_{cl}) and the number of tracklets (N_{tr}), as discussed in Ref.[78]. The cut is defined as in the following:
if ($N_{\text{tr}} < 165$):

$$N_{\text{cl}} = 65 + 5.5 \cdot N_{\text{tr}} - 0.009 \cdot N_{\text{tr}}^2,$$

and if ($N_{\text{tr}} > 165$):

$$N_{\text{cl}} = 65 + 4 \cdot N_{\text{tr}}^2.$$

Figure 3.2 presents the distributions of the correlation between N_{cl} and N_{tr} in the forward

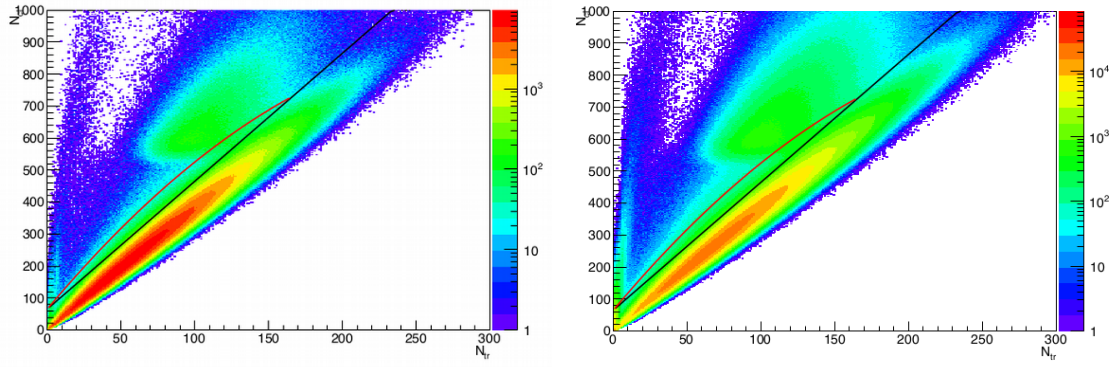

(a) CMUL7 events in the forward rapidity region (b) CMUL7 events in the backward rapidity region

Figure 3.2: The correlation between the N_{cl} and the N_{tr}. The black line represents the default cut, while the red line represents the customized cuts used for the p–Pb multiplicity-dependent analysis.

and backward rapidity regions. The SPD default cut is shown by a black line in the figure, while the red line represents the customized cuts defined in the previous equations.

3.2.2 Muon track selection

The following cuts are applied to the muon tracks to remove fake tracks. For the single muon track selections:

- **The geometrical acceptance**: the muon spectrometer acceptance is $-4 < \eta_{\rm lab} < -2.5$. Any muon track reconstructed outside of this interval is rejected.
- **MID-MCH matched tracks**: the muon track candidate is considered a true track if the tracks reconstructed in the muon chambers matched a track segment in the trigger chambers.
- **Polar angle of the muon tracks**: this cut considers the polar angle of the muon track at the end of the front absorber ($\theta_{\rm abs}$). This requires that $\theta_{\rm abs}$ must fall in the range $2^\circ < \theta_{\rm abs} < 10^\circ$. This cut ensures the selected muon track did not experience significant multiple scattering, by rejecting the tracks that traverse the front absorber through the high Z-material part.
- **The track total momentum and distance of closest approach (pDCA)**: the DCA is defined as the distance between the primary vertex and the straight line extrapolation of the track exiting the front absorber. The product of the track momentum (p) and its DCA (pDCA) must be within 6σ, which helps to reject the beam-induced interaction and particles produced in the front absorber.

In the case of the dimuon selections, the criteria also requires that the muon pair is within the acceptance of the muon spectrometer, i.e., $2.5 < y_{\rm lab} < 4$.

3.3 Multiplicity determination

3.3.1 Multiplicity estimator

We use the number of tracklets ($N_{\rm tr}$), as multiplicity estimator for the charged-particle multiplicity ($\mathrm{d}N_{\rm ch}/\mathrm{d}\eta$). The tracklets are formed by combining hits in both SPD layers that point towards a primary vertex. The SPD detector also determines the position of the primary vertex.
Figure 3.3 presents the average number of tracklets $< N_{\rm tr} >$ as a function of the z-coordinate of the primary vertex in the SPD. The blue points in the figure show a dependence of the raw number of tracklets on the z-coordinate of the vertex. However, we would expect the

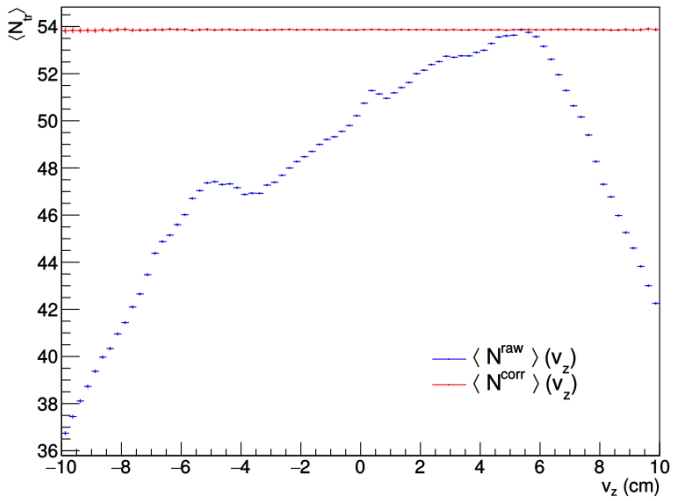

Figure 3.3: Average number of tracklets $< N_{\rm tr} >$ as a function of the z-coordinate of the SPD vertex v_z before (blue) and after (red) applying the Poissonian correction [78].

average number of tracklets per event to remain constant regardless of where in the detector the collision occurs. The observed z-dependence of the $< N_{\rm tr} >$ is due to inefficiencies of the SPD. For the p–Pb multiplicity dependent analysis, the method mentioned in Refs. [78, 63] is used to equalize the average number of the $\langle N_{\rm tr} \rangle$, and evaluate the average number of corrected tracklets $< N^{\rm corr} >$. For each event, the number of missing or excessive tracklets ΔN with respect to a reference value $(N_{\rm tr}(v_z^0))$ is evaluated as:

$$\Delta N = N_{\rm tr}(v_z) \frac{N_{\rm tr}(v_z^0) - N_{\rm tr}(v_z)}{< N_{\rm tr}(v_z) >} \tag{3.5}$$

Then, the number of raw tracklets $N_{\rm tr}$ per event is randomized by Poisson smearing the excess ΔN to obtain the number of corrected tracklets; i.e. N^{corr}

$$N^{\rm corr} = N_{\rm tr} \pm {\rm gRandom} \rightarrow {\rm Poisson}(\Delta N)\,. \tag{3.6}$$

This correction corresponds to a data-driven event-by-event procedure to take into account the detector inefficiencies. Figure 3.3 presents the resultant values of the average number corrected tracklets per event, represented with red markers. The corrected distribution is independent of the z-vertex location of the interaction, as expected.

3.3.2 From corrected tracklets to charged-particle multiplicity

To obtain the number of charged particles ($N_{\rm ch}$) from the number of corrected tracklets ($N^{\rm corr}$), one needs to evaluate the correlation factor between the two quantities. DPMJET event generator [79] is used to evaluate the correlation distribution as it cannot be obtained from the data. In this analysis, two methods are used to extract and cross-check the $N_{\rm ch}$ value corresponding to a given $N^{\rm corr}$ interval:

1. Fit the 2D $N^{\rm corr}$-$N_{\rm ch}$ distribution over the integrated interval, and in bins of $N^{\rm corr}$. Then, $N_{\rm ch}$ is computed for each $N^{\rm corr}$ bin as follows:

$$< N_{\rm ch} >_i = f(< N^{\rm corr} >),$$

   where (i) is the $N^{\rm corr}$ bin and f is the fitting function. The uncertainty of each value is taken from the uncertainty of the fit.

2. Project the 2D distribution, in the selected $N^{\rm corr}$ interval i, on the $N_{\rm ch}$ axis. Then, the projected distribution in each bin of $N^{\rm corr}$ is fitted by a Gaussian function. The $N_{\rm ch}$ value is obtained from the mean of the Gaussian, and the standard deviation is the assigned uncertainty.

In Fig.3.4, the 2D $N^{\rm corr}$-$N_{\rm ch}$ distribution is shown for the forward rapidity data set in the top panel, and the backward rapidity data set in the bottom panel. The black points in the figure represent the profile of the $N_{\rm ch}$ on the 2D distribution, while the lines represent the functions used to fit the distribution.
For each bin of $N^{\rm corr}$, a linear fit to the 2D $N^{\rm corr}$-$N_{\rm ch}$ distribution is used to extract the correlation factor and evaluate the corresponding $N_{\rm ch}$. In the case of the integrated 2D $N^{\rm corr}$-$N_{\rm ch}$ distribution, the following fit functions are used:

1. Linear fit to the 2D distribution, fixing the origin of the function at zero

$$f(N^{\rm corr};\alpha) = \alpha(N^{\rm corr}),$$

   where $N_{\rm ch}$ is evaluated as:

$$N_{\rm ch} = f(N^{\rm corr};\alpha) \rightarrow {\rm Eval}\left(N^{\rm corr}\right).$$

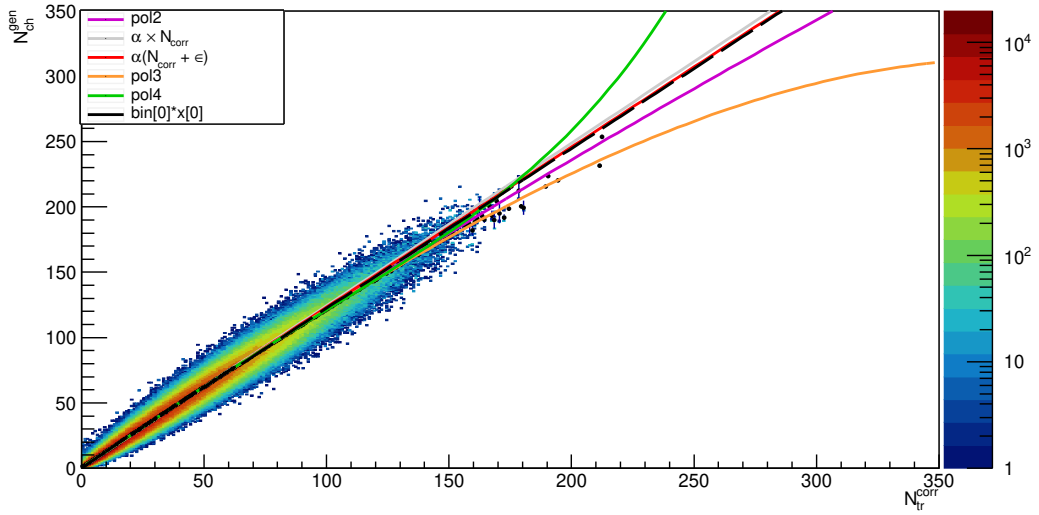

(a) Forward rapidity

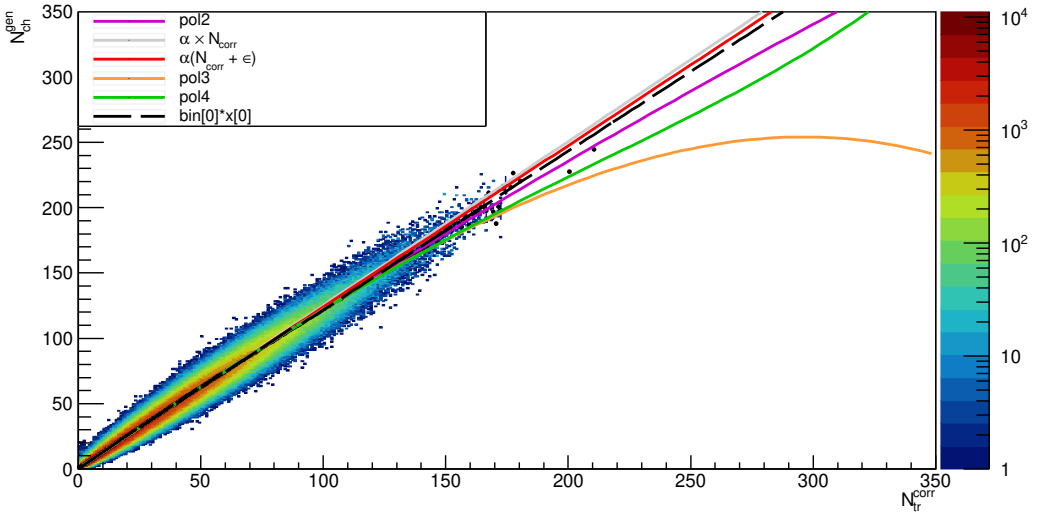

(b) Backward rapidity

Figure 3.4: 2D correlation of charged-particle multiplicity and corrected number of tracklets simulated by DPMJET for forward (backward) rapidity region in the top (bottom) panel.

2. Linear fit to the 2D distribution with free parameters at the origin

$$f(N^{\mathrm{corr}};\alpha,\epsilon) = \alpha(N^{\mathrm{corr}}+\epsilon)\,,$$

$$N_{\mathrm{ch}} = f(N^{\mathrm{corr}};\alpha,\epsilon) \rightarrow \mathrm{Eval}\left(N^{\mathrm{corr}}\right).$$

3. A second-order polynomial fit function with free fitting parameters

$$N_{\mathrm{ch}} = \mathrm{pol2} \rightarrow \mathrm{Eval}\left(N^{\mathrm{corr}}\right).$$

4. A third-order polynomial fit function with free fitting parameters

$$N_{\mathrm{ch}} = \mathrm{pol3} \rightarrow \mathrm{Eval}\left(N^{\mathrm{corr}}\right).$$

5. A fourth-order polynomial fit function with free fitting parameters

$$N_{\mathrm{ch}} = \mathrm{pol4} \rightarrow \mathrm{Eval}\left(N^{\mathrm{corr}}\right).$$

The fit functions are shown in Fig.3.4. The fits to the distribution are similar at the intermediate N^{corr} range and start to diverge at large N^{corr}. To assess the possible dispersion of these fits, N_{ch} is evaluated in each N^{corr} bin for each fit function. Then, the results are compared to the corresponding value extracted from the fit of the projection on the N_{ch} axis. Fig.3.5 shows the result of the N_{ch} values obtained from the different fit functions in each N^{corr} bin for both forward and backward rapidity regions. Figure 3.6 presents the ratio of the N_{ch} extracted from the different fits to the value extracted from the projection on the N_{ch} axis for each N^{corr} bin. In this result, we conclude that the N_{ch} values evaluated from the linear bin-by-bin fit and the second-order polynomial are the closest to the ones extracted from the projections onto the N_{ch} axis. In the J/ψ multiplicity-dependent analysis, which was performed using the same data set, the second-order polynomial was used to evaluate the N_{ch}, as the bin-by-bin linear fit was not stable due to the low statistics in the MC for the highest multiplicity intervals [63]. To be consistent with the J/ψ analysis, the second-order polynomial fit is also used to compute the charged-particle multiplicity in this analysis. The uncertainty of this measurement is obtained by comparing the values extracted from the second-order polynomial and the maximum spread of the values extracted from the other fit functions, as depicted in Fig.3.7. The values of the systematic uncertainties in each bin for both forward and backward rapidity regions are tabulated in Tab.3.1.

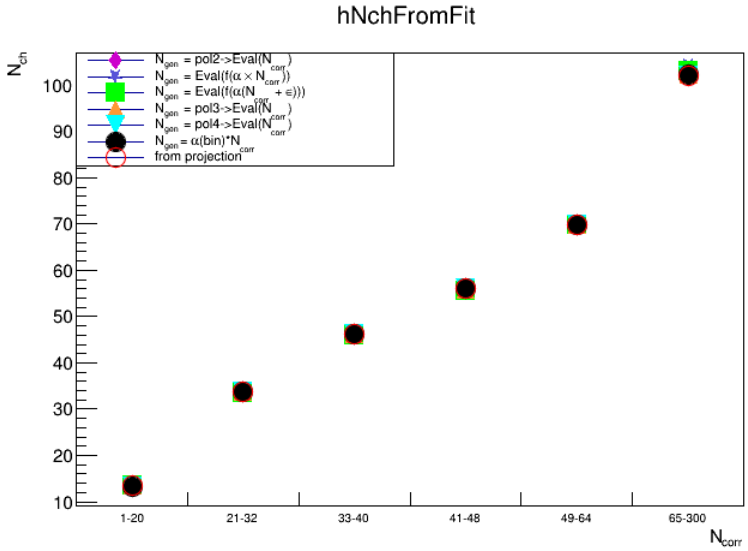

(a) Forward rapidity

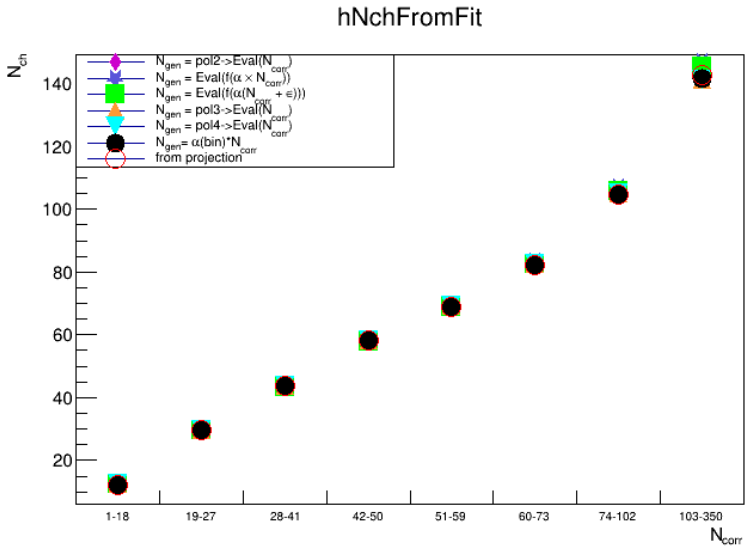

(b) Backward rapidity

Figure 3.5: Extracted N_{ch} values in each N^{corr} bin for each fit function, for the forward rapidity in the top panel and the backward rapidity in the bottom panel.

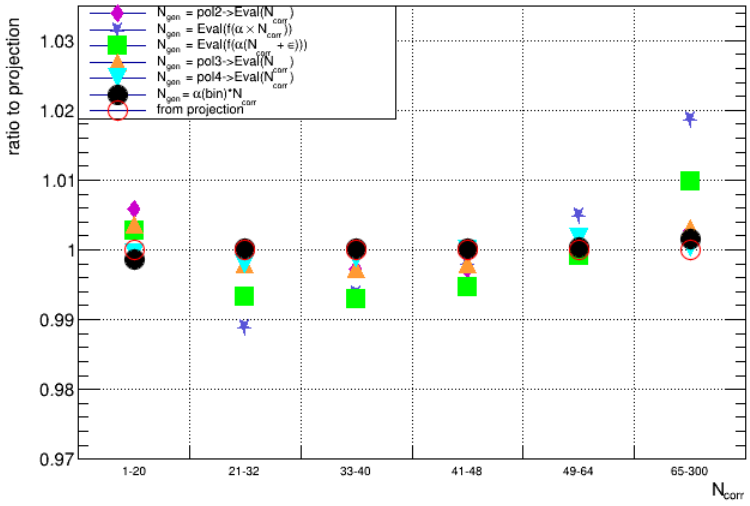

(a) Forward rapidity

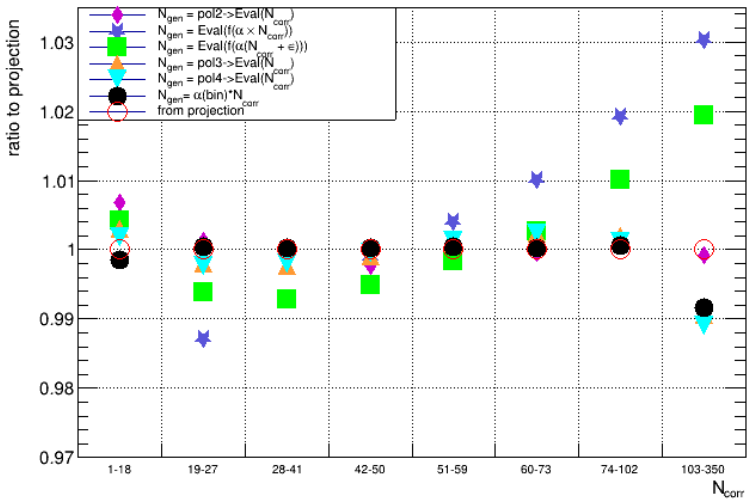

(b) Backward rapidity

Figure 3.6: Ratio of N_{ch} extracted from the different fits to the corresponding value extracted from the projection of N^{corr} on the N_{ch} axis in each N^{corr} bin.

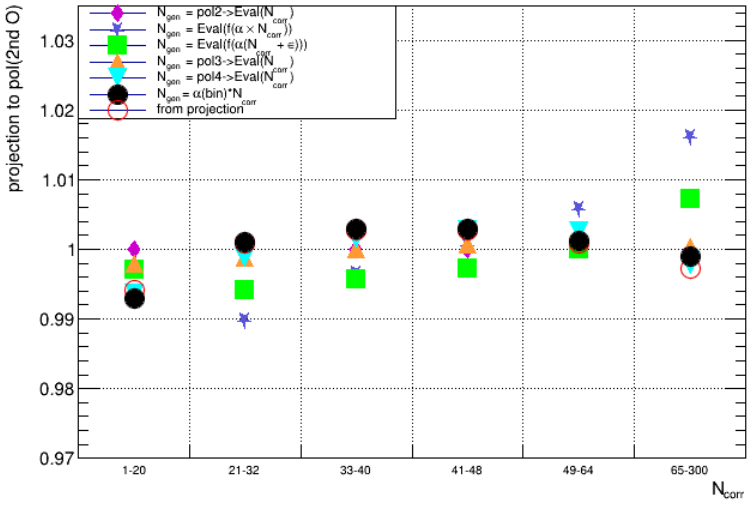

(a) Forward rapidity

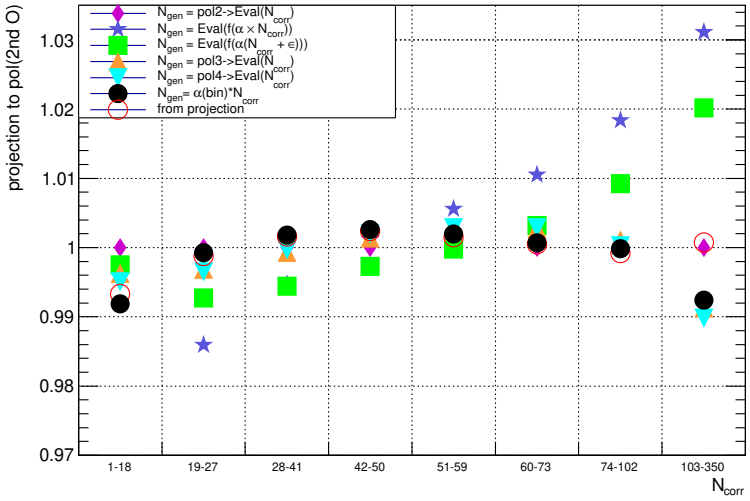

(b) Backward rapidity

Figure 3.7: Ratio of N_{ch} extracted from the different fits to the corresponding value extracted from second-order polynomial in each multiplicity interval, for both (a) forward rapidity and (b) backward rapidity. The maximum spread of N_{ch} from unity is considered as the systematic uncertainty.

Forward rapidity region		Backward rapidity region	
N^{corr} bin	syst.(%)	N^{corr} bin	syst.(%)
1-20	3.66	1-18	3.99
21-32	1.01	19-27	1.4
33-40	0.43	28-41	0.53
41-48	0.30	42-50	0.27
49-64	0.59	51-59	0.55
65-300	1.61	60-73	1.05
		74-102	1.84
		103-350	3.11

Table 3.1: Systematic uncertainty on the $N_{ch} - N^{corr}$ correlation for the forward and backward rapidity regions. The uncertainty is obtained by comparing the values extracted from the second-order polynomial and those extracted from the other fit functions. The maximum spread of the values is assigned as systematic uncertainty.

3.3.3 Average charged-particle multiplicity (<$dN_{ch}/d\eta$>) in the integrated N^{corr} bin

The $< dN_{ch}/d\eta >$ is measured in an independent analysis performed in p–Pb collisions at $\sqrt{s_{NN}}$ = 8.16 TeV (see Ref.[80]). In this analysis, the average charged-particle multiplicity is extracted from p–Pb collisions at $\sqrt{s_{NN}}$ = 8.16 TeV in the rapidity range $|\eta_{lab}| < 1$. The obtained values and their systematic uncertainties are presented in Tab.3.2.

	$\langle dN_{ch}/d\eta \rangle_{|\eta_{lab}|<1}$
Forward rapidity	20.33 ± 0.83
Backward rapidity	20.32 ± 0.83

Table 3.2: $\langle dN_{ch}/d\eta \rangle$ at midrapidity in $|\eta_{lab}| < 1$.

3.3.4 Systematic uncertainties on the multiplicity measurements

In this section, we discuss the sources of systematic uncertainties considered for the charged-particle multiplicity measurements.

Charged-particle multiplicity evaluation

Several fit functions were used to evaluate the correlation factor between N^{corr} and N_{ch} from MC. Either from fits over the full range of N^{corr}, or from the distributions obtained in bins of N^{corr}. In summary, the systematic uncertainty is extracted from the maximum spread of

the N_{ch} using all the fit functions with respect to the values extracted from the second-order polynomial (the central value). More details in Sec. 3.3.3.

MC input

This uncertainty is assessed using two different MC event generators to extract the correlation factor between the number of corrected tracklets and the charged-particle multiplicity. In Ref.[78], EPOS and DPMJET event generators were used to extract the correlations and evaluate the N_{ch} values. The uncertainty was determined by comparing the result evaluated from each generator for each data set. The uncertainty from this source amounts to 2% in both rapidity regions.

z-vertex equalization

This is due to the non-flat distribution of the average number of reconstructed tracklets as a function of the z-coordinate of the primary vertex. As explained in Sec. 3.3.1, an event-by-event correction is applied to the number of tracklets to correct for this effect. The uncertainty on the correction procedure is determined by comparing the results varying the reference value (from the maximum to the minimum of the average number of tracklets), as well as varying the randomization procedure (using a binomial distribution instead of a poissonian one). Details can be found in Ref. [78]. The systematic uncertainty due to the z-vertex equalization amounts to 3%.

Total systematic uncertainty

The uncertainty sources on the charged-particle multiplicity are presented in Tab.3.3.

source	forward rapidity	backward rapidity
$N_{\mathrm{ch}} - N^{\mathrm{corr}}$ correlation	0.3–3.7%	0.3–4%
MC input	2%*	2%*
residual z-vertex dependence	3%*	3%*
$\langle \mathrm{d}N_{\mathrm{ch}}/\mathrm{d}\eta \rangle$	4%*	4%*
total	5.4–6.5 %	5.4–6.1 %

Table 3.3: Systematic uncertainty sources on the charged particle multiplicity measurement. Values marked with an asterisk are correlated in multiplicity.

3.3.5 Self-normalized charged particle multiplicity

The final values obtained for the charged-particle multiplicity and its corresponding self-normalized charged-particle multiplicity are summarized in Tab.3.4.

Forward rapidity region				Backward rapidity region			
N^{corr}	$\langle N^{\mathrm{corr}} \rangle$	$\langle N_{\mathrm{ch}} \rangle$	$\frac{\mathrm{d}N_{\mathrm{ch}}/\mathrm{d}\eta}{\langle \mathrm{d}N_{\mathrm{ch}}/\mathrm{d}\eta \rangle}$	N^{corr}	$\langle N^{\mathrm{corr}} \rangle$	$\langle N_{\mathrm{ch}} \rangle$	$\frac{\mathrm{d}N_{\mathrm{ch}}/\mathrm{d}\eta}{\langle \mathrm{d}N_{\mathrm{ch}}/\mathrm{d}\eta \rangle}$
1-20	10.4	13.47	0.33	1-18	9.50	12.40	0.31
21-32	26.85	33.76	0.83	19-27	23.42	29.78	0.73
33-40	36.90	46.07	1.13	28-41	34.73	43.76	1.08
41-48	44.88	55.78	1.37	42-50	46.33	58.00	1.43
49-64	56.35	69.66	1.72	51-59	55.29	68.91	1.70
65-300	83.95	102.64	2.53	60-73	66.38	82.32	2.03
				74-102	85.26	104.93	2.58
				103-350	118.24	143.65	3.53

Table 3.4: Mean number of corrected tracklets ($\langle N^{\mathrm{corr}} \rangle$), average charged particle multiplicity ($\langle N_{\mathrm{ch}} \rangle$), and corresponding relative charged particle multiplicity $\left(\frac{\mathrm{d}N_{\mathrm{ch}}/\mathrm{d}\eta}{\langle \mathrm{d}N_{\mathrm{ch}}/\mathrm{d}\eta \rangle} \right)$ in p–Pb collisions.

3.4 Charmonium signal extraction

The charmonium yields are extracted exploiting the low-p_{T} dimuon triggered data sample (CMUL7)[1]. For each selected pair of opposite-charge muon tracks (the selection criteria are discussed in Sec.3.2.2), the dimuon invariant mass ($M_{\mu\mu}$) is computed as follows:

$$M_{\mu\mu} = \sqrt{2m_{\mu}^2 + 2E_{\mu_1}E_{\mu_2}(1-\cos\theta_{12})}, \tag{3.7}$$

where m_{μ} is the mass of the muon, E_{μ} is the energy of the muon, and θ_{12} is the angle between the two muon tracks. The number of J/ψ and ψ(2S) particles are evaluated by fitting the invariant mass distribution in the mass range of the J/ψ and ψ(2S). The following sections describe the fit procedure to extract charmonium raw and relative yields, as well as their corresponding uncertainties.

3.4.1 Fit procedure

The charmonium signal is fitted using either a double crystal ball (CB2) or a pseudo-Gaussian function with power-law tails (as implemented first by the NA60 Collaboration) [81]. Both of these functions consist of a Gaussian core which describes the detector resolution, and power-law tails on both sides of the Gaussian core. The tails account for detector effects such as the energy loss and multiple scatterings experienced by the muon tracks traversing the front absorber. The tail parameters are fixed to values obtained from either data or MC simulations. Three sets of parameters extracted from data are used; one from pp collisions at $\sqrt{s}$ = 13 TeV and two sets from p–Pb collisions at $\sqrt{s_{\mathrm{NN}}}$ = 8.16 TeV with and without z-vertex cuts and pile-up rejection. Additionally, the MC parameters were extracted from simulations of pp collisions at $\sqrt{s}$ = 13 TeV and from p–Pb collisions at $\sqrt{s_{\mathrm{NN}}}$ = 8.16 TeV, with the z-vertex cut and pile-up rejection applied. All the aforementioned sets of tail parameters are used when fitting the signal with the CB2 signal shape. In contrast, only the parameter set extracted from MC simulations of the p–Pb collisions at $\sqrt{s_{\mathrm{NN}}}$ = 8.16 TeV is considered when fitting with the NA60 signal shape. Figure 3.8 shows the sets of tail parameters used when fitting with the CB2 and NA60 on the top and bottom panels, respectively. Appendix B summarizes the functional fit forms and tail parameters considered in the fit procedure.
The ψ(2S) signal is modeled with the same functional form and tail parameters as the J/ψ signal. The ψ(2S) mass and width parameters are bound to the J/ψ ones, which are left free in the fit procedure. The mass difference between the J/ψ and ψ(2S) is taken from the

[1] See Sec.3.2.1 for the details about the trigger classes.

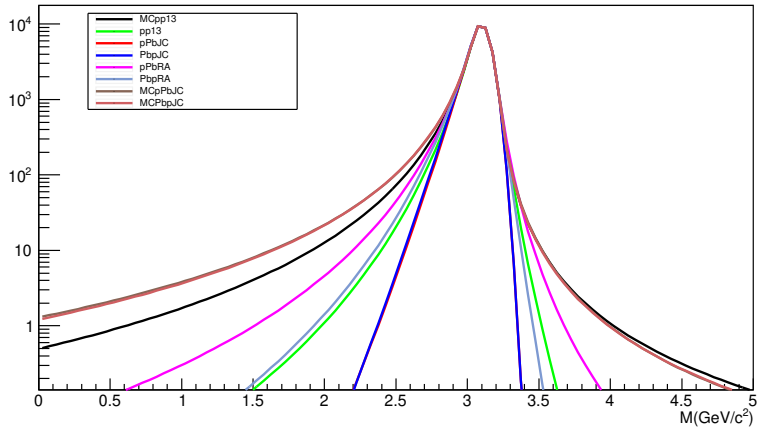

(a) CB2

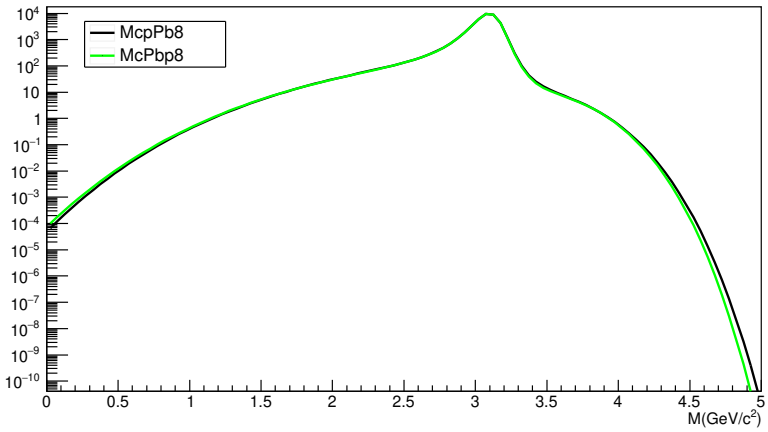

(b) NA60

Figure 3.8: The set of tails used when fitting the signal shape with (a) CB2 on the top panel or with (b) NA60 function on the bottom panel.

particle data group (PDG) [5], such as:

$$m_{\psi(2S)} = m_{J/\psi} + (m^{PDG}_{\psi(2S)} - m^{PDG}_{J/\psi}) . \tag{3.8}$$

The width correlation between the two particles is evaluated from MC simulations by PYTHIA for pp collisions at $\sqrt{s}$ = 13 TeV, which amounts to 5%. This ratio could also be calculated by exploiting the large data set from pp collisions at a $\sqrt{s}$ = 13 TeV. The high statistics of this data sample allowed for the J/ψ and ψ(2S) widths to be left as free parameters during the fit process. This results in a ratio of 1.01 ± 0.05 [82]. To account for the possible variation in the width of the ψ(2S) peak, both ratios, 1.05 and 1.01, are used to evaluate the ψ(2S) raw yields and the corresponding systematic uncertainty.
The background shape is delineated using two functions: a sum of two exponential functions (`SumExp`) or a fourth-order polynomial convoluted with an exponential function (`expo*pol4`). Finally, two mass ranges are used in the fit to extract charmonium raw yields: [1.7,4.8] GeV/c^2 and [2.0-5.0] GeV/c^2. Taking into account all the aforementioned fit configurations, the number of tests performed in a given multiplicity interval with the CB2 signal shape is:

$$5 \text{ tails} \times 2 \text{ widths} \times 2 \text{ backgrounds} \times 2 \text{ invariant mass ranges} = 40,$$

and with the NA60 signal shape:

$$2 \text{ tails} \times 2 \text{ widths} \times 2 \text{ backgrounds} \times 2 \text{ invariant mass ranges} = 8.$$

A total of 40 + 8 = 48 different fit configurations are used to extract charmonium raw yields and their uncertainties. An example of the dimuon invariant mass fit is displayed in Fig.3.9 for the integrated multiplicity interval in p–Pb collisions at $\sqrt{s_{NN}}$ = 8.16 TeV at the forward (backward) rapidity region in the top (bottom) panel. The figure shows the J/ψ and ψ(2S) signal shapes as red and yellow shaded areas, respectively. The background is depicted with a grey dashed line. Finally, the total mass fit is displayed as a continuous blue line.
The raw yields extracted as a function of fit configuration are presented in Fig.3.10 and Fig.3.11, for the J/ψ and ψ(2S), respectively. The most significant influence on yield extraction originates from the sets of tail parameters used in the fit (be it data or MC). As we do not use the same number of tails from data and MC, to account for this influence, the yields obtained from each fit configuration are weighted when averaging over all configurations to obtain the resultant yield and its corresponding uncertainty. The weighting is done to

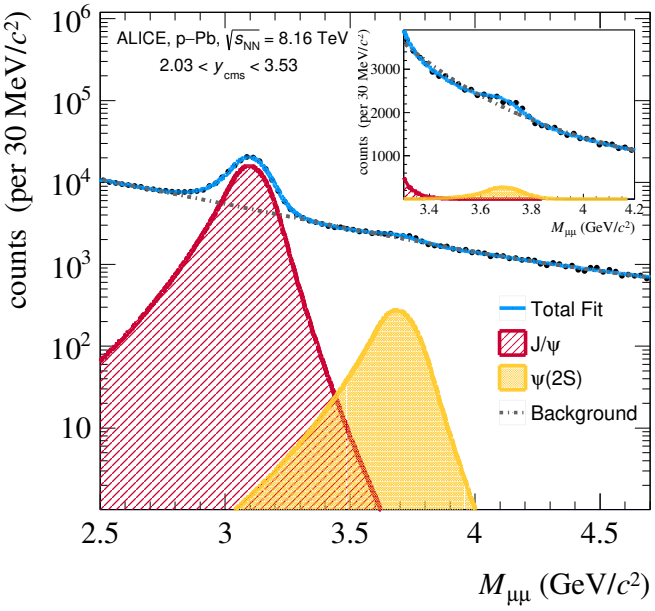

(a) Forward rapidity

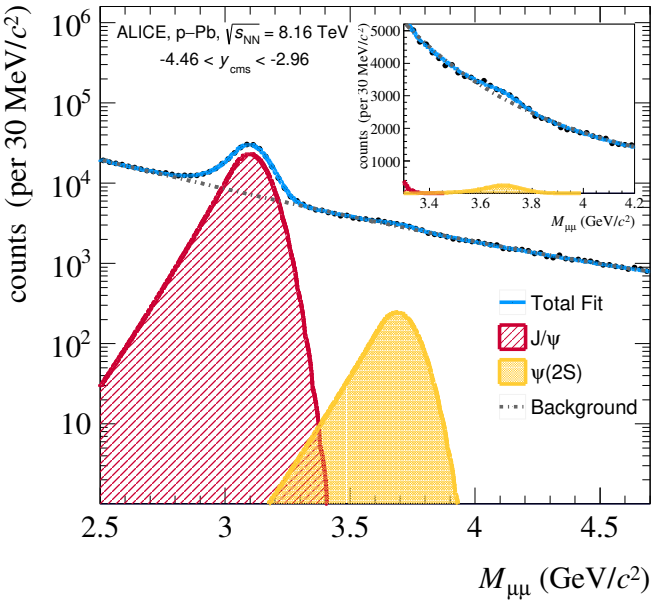

(b) Backward rapidity

Figure 3.9: Invariant-mass distribution of opposite-sign muon pairs in (a) forward and (b) backward rapidity, integrated in multiplicity [83]. Superimposed is a typical fit function, shown as a solid blue line (see text for details). The J/ψ and ψ(2S) contributions are shown as red and yellow shaded areas, respectively. The background is depicted as a dashed grey line. The inset shows the region of the ψ(2S) mass.

balance the number of tests using tails from data and MC. The yields and the statistical uncertainties are evaluated from the weighted average. The systematic uncertainty is obtained using the root-mean-square (RMS) of the values.

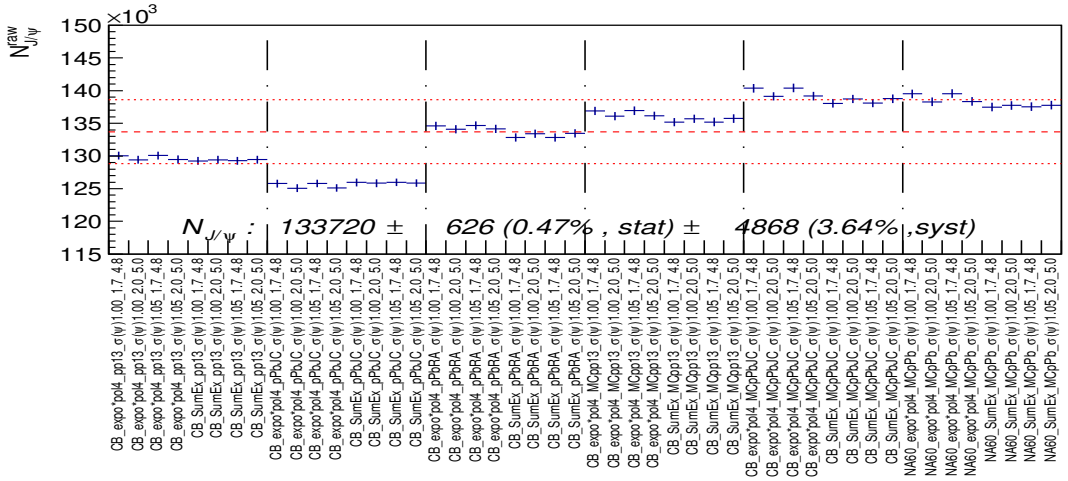

(a) Forward rapidity

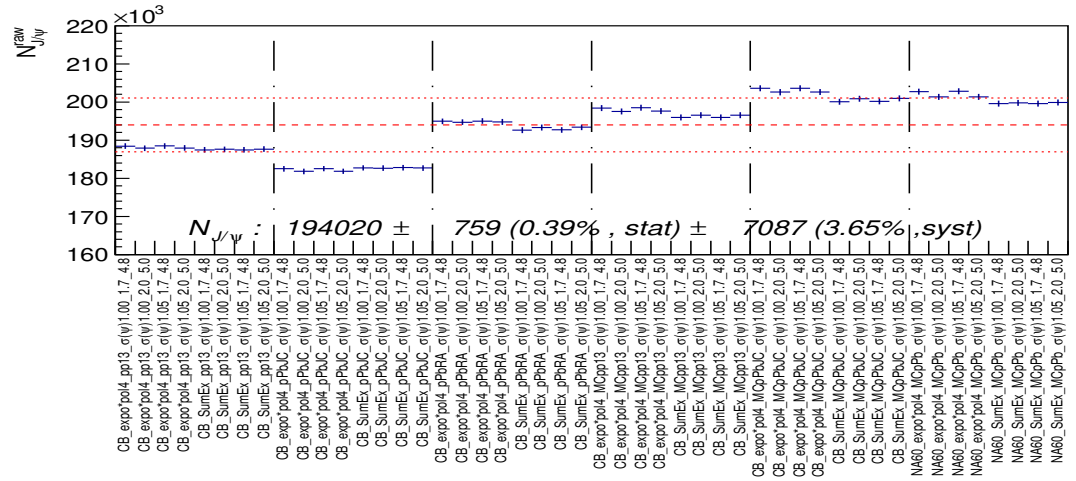

(b) Backward rapidity

Figure 3.10: J/ψ raw yields as a function of the fit configuration for forward rapidity in the top panel, and for backward rapidity in the bottom panel. The yields are extracted over integrated multiplicity, p_{T}, and y.

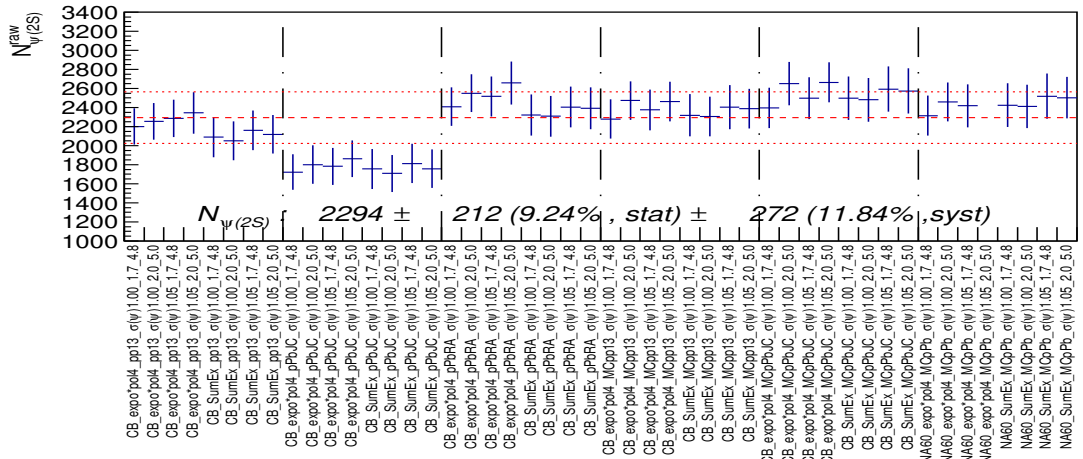

(a) Forward rapidity

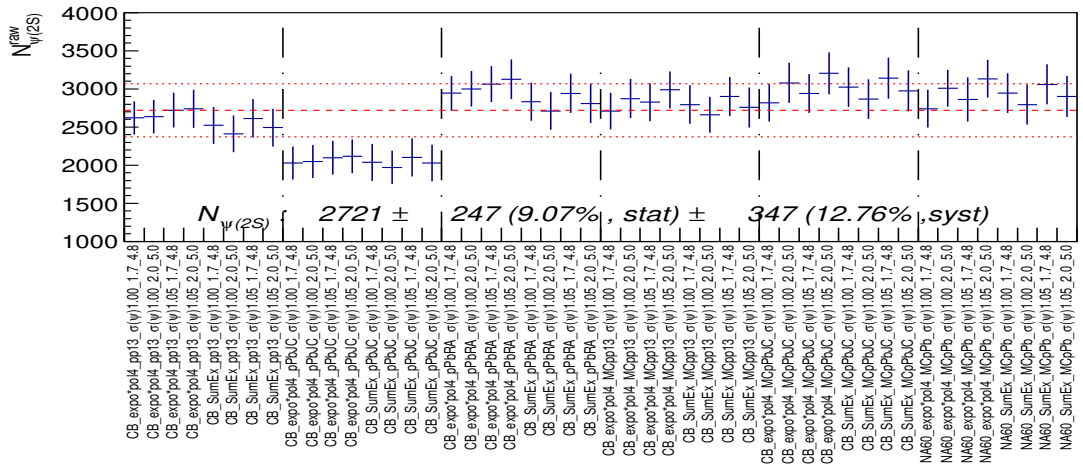

(b) Backward rapidity

Figure 3.11: $\psi(2S)$ raw yields as a function of fit configuration for forward (backward) rapidity in the top (bottom) panel. The yields are extracted over integrated multiplicity, p_T, and y.

3.4.2 Raw yield extraction

Integrated multiplicity, p_{T} and y raw charmonium yields

This section presents the results of J/ψ and ψ(2S) raw yields integrated in multiplicity, p_{T}, and y. The raw yields as a function of fit configuration are shown in Fig. 3.10 and Fig. 3.11 for J/ψ and ψ(2S), respectively. The plots show the raw yields extracted for the forward rapidity data set in the top panels, and the backward rapidity data set in the bottom panels. The yields are grouped by the tail parameters used in the fit (notice the vertical dashed lines in the figures). The horizontal red dashed line presents the weighted average over all the fit trials, whereas the dotted line presents the standard deviation, which is used to evaluate the systematic uncertainty. The J/ψ and ψ(2S) raw yield results are summarized in table 3.5.

	$\mathrm{N}_{\mathrm{J}/\psi}$	$N_{\psi(2S)}$
Forward	133720 ± 626 (stat.) ± 4868 (syst.)	2301 ± 212 (stat.) ± 272 (syst.)
Backward	194020 ± 759 (stat.) ± 7087 (syst.)	2721 ± 247 (stat.) ± 347 (syst.)

Table 3.5: J/ψ and ψ(2S) raw yields integrated over multiplicity, p_{T} and y for both forward and backward rapidity.

Multiplicity differential raw yield extraction

The charmonium raw yields are also extracted in multiplicity intervals, where the binning was determined by the available statistics and the stability of the fits. The choice of the multiplicity intervals is driven by the statistics of the ψ(2S) yields. The results of the raw yields extracted for each fit configuration, and for each multiplicity interval can be found in App.C and App.D, for J/ψ and ψ(2S), respectively. Tab. 3.6 and Tab. 3.7 summarize the results obtained for J/ψ and ψ(2S) raw yields for the forward and backward rapidity regions. The bottom row of each table shows the difference between the yields extracted in the integrated multiplicity interval and the total summation of the yields extracted in the multiplicity intervals. The difference is found to be negligible in both rapidity regions (with respect to the statistical uncertainty).

3.4.3 Relative raw yield evaluation

The relative raw yield in a multiplicity interval i, is defined as the ratio of the raw yield extracted in the multiplicity interval (i) to the raw yield extracted in the integrated multiplicity

Forward rapidity region		Backward rapidity region	
N^{corr} bin	$N_{J/\psi}$ ± stat ± syst	N^{corr} bin	$N_{J/\psi}$ ± stat ± syst
0-300	133720 ± 626 ± 4868	0-350	194020± 759±7087
1-20	16082 ± 203(1.26%) ± 568 (3.53%)	1-18	14037± 187(1.33%) ± 489(3.48%)
21-32	19915 ± 232 (1.17%) ± 709 (3.56%)	19-27	16306± 204(1.25%) ± 578(3.54%)
33-40	15800 ± 212 (1.34%) ± 580(3.67%)	28-41	34020± 304(0.89%) ± 1216(3.57%)
41-48	15594 ± 213 (1.36%) ± 572(3.67%)	42-50	25093± 265(1.06%) ± 909(3.62%)
49-64	27525± 285(1.03%) ± 1028(3.73%)	51-59	23736± 266(1.12%) ± 853(3.59%)
65-300	38754 ± 352(0.91%) ± 1430(3.69%)	60-73	31013± 312(1.01%) ± 1129(3.64%)
		74-102	36449± 346(0.95%) ± 1361(3.73%)
		103-350	13182± 218(1.65%) ± 518(3.93%)
Σ in bins	133670	Σ in bins	193836
Δ	50	Δ	184

Table 3.6: J/ψ raw yield integrated p_T and y, in multiplicity intervals. Σ is the sum over all multiplicity intervals and Δ is the difference between Σ and integrated result.

Forward rapidity region		Backward rapidity region	
N^{corr} bin	$N_{\psi(2S)}$ ± stat ± syst	N^{corr} bin	$N_{\psi(2S)}$ ± stat ± syst
0-300	2301 ± 212 ± 277	0-350	2721 ± 247 ± 347
1-20	290 ± 61(21%) ± 34 (11.8%)	1-18	206± 51(24.7%) ± 29(14.2%)
21-32	325 ± 76 (23.3%) ± 43 (13.3%)	19-27	224± 59(26.5%) ± 32(14.3%)
33-40	371 ± 75 (20.3%) ± 36 (9.6%)	28-41	393± 92(23.4%) ± 63 (16.0%)
41-48	311 ± 80 (25.7%) ± 38 (12.3%)	42-50	385± 84(21.7%) ± 49 (12.6%)
49-64	456 ± 111 (24.4%) ± 58 (12.6%)	51-59	298 ± 91 (30.7%) ± 39 (13.0%)
65-300	555 ± 131 (23.6%) ± 85 (15.3%)	60-73	417 ± 108 (25.9%) ± 54 (13.0%)
		74-102	542 ± 125 (23.07%) ± 78 (14.3%)
		103-350	235 ± 86 (36.4%) ± 36 (15.1%)
Σ in bins	2308	Σ in bins	2700
Δ	7	Δ	21

Table 3.7: ψ(2S) raw yield integrated p_T and y, in multiplicity intervals. Σ is the sum over all multiplicity intervals and Δ is the difference between Σ and integrated result.

interval (N^{tot}):

$$N_R^i = \frac{N_{\text{raw}}^i}{N^{\text{tot}}}. \tag{3.9}$$

The relative raw yield is computed by assuming that the signal part (the signal shape function, the tail parameters, and the width) is correlated in the numerator and the denominator of equation 3.9. On the other hand, the combinatorial background component is assumed to be uncorrelated as a function of multiplicity, which was verified by comparing the invariant mass distributions in different multiplicity intervals, i.e., different background shapes are observed at low multiplicity compared to high multiplicity interval. Having all the different combinations of the fitting model in the integrated and differential multiplicity, we obtained 192 variations to evaluate the charmonium relative raw yields, with 162 variations for CB2 and 32 for NA60 signal shapes. The mean over all these combinations gives the central value for each multiplicity interval, and its corresponding statistical uncertainty is evaluated as the mean over all the statistical uncertainties of the combinations. The systematic uncertainty is evaluated as the standard deviation. The relative raw yields in the differential multiplicity intervals and their corresponding uncertainties are summarized in Tab. 3.8 and Tab. 3.9, for J/ψ and ψ(2S), respectively. While the J/ψ statistical uncertainties are of the order of 1%, the uncertainty of the ψ(2S) yields ranges between 20%–30%, apart from the last interval at backward rapidity where the uncertainty increases to 38%.

3.4.4 ψ(2S)-over-J/ψ relative ratio

We are also interested in studying the difference in the behavior of the J/ψ and ψ(2S) as a function of charged-particle multiplicity. To do so, one needs to evaluate the $\psi(2S) - \text{over} - J/\psi$ relative ratio. The ratio is computed considering the correlation on the signal part of the fit function, as described in the previous section for the relative yield. The values extracted for each multiplicity interval are summarized in Tab.3.10 for both the forward and backward rapidity regions.

3.5 Charmonium yield corrections

The charmonium corrected yields are computed as expressed in Eq. 3.3 (see Sec. 3.1).

Forward rapidity		Backward rapidity	
N^{corr}	$N^{R}_{J/\psi}$ ± stat ± syst	N^{corr}	$N^{R}_{J/\psi}$ ± stat ± syst
1-20	0.1203 ± 0.0016 (1.34%) ± 0.0008 (0.63%)	1-18	0.0724 ± 0.0010 (1.39% ± 0.0004 (0.6%)
21-32	0.1489 ± 0.0019 (1.26%) ± 0.0009 (0.56%)	19-27	0.0840 ± 0.0011 (1.31%) ± 0.0006 (0.74%)
33-40	0.1182 ± 0.0017 (1.42%) ± 0.0008 (0.66%)	28-41	0.1754 ± 0.0017 (0.97%) ± 0.0011 (0.61%)
41-48	0.1166 ± 0.0017 (1.44%) ± 0.0008 (0.67%)	42-50	0.1293 ± 0.0015 (1.13%) ± 0.0009 (0.73%)
49-64	0.2058 ± 0.0023 (1.14%) ± 0.0016 (0.80%)	51-59	0.1223 ± 0.0015 (1.19%) ± 0.0008 (0.66%)
65-300	0.2898 ± 0.0030 (1.02%) ± 0.0020 (0.69%)	60-73	0.1598 ± 0.0017 (1.08%) ± 0.0010 (0.65%)
		74-102	0.1878 ± (1.03%) 0.0019 ± 0.0016 (0.73%)
		103-350	0.0680 ± 0.0012 (1.7%) ± 0.0010 (1.41%)

Table 3.8: Relative J/ψ yield per multiplicity interval at forward and backward rapidity.

Forward rapidity region		Backward rapidity region	
N^{corr}	$N^{R}_{\psi(2S)}$ ± stat ± syst	N^{corr}	$N^{R}_{\psi(2S)}$ ± stat ± syst
1-20	0.1260 ± 0.0292 (23.2%) ± 0.0048 (3.8%)	1-18	0.0758 ± 0.0202 (26.7%) ± 0.0045 (5.9%)
21-32	0.1413 ± 0.0358 (25.0%) ± 0.0078 (5.5%)	19-27	0.0821 ± 0.0235 (28.6%) ± 0.0041 (5.0%)
33-40	0.1619 ± 0.0364 (22.5%) ± 0.0106 (6.5%)	28-41	0.1440 ± 0.0369 (25.7%) ± 0.0094 (6.5%)
41-48	0.1353 ± 0.0371 (27.4%) ± 0.0091 (6.7%)	42-50	0.1418 ± 0.0338 (23.4%) ± 0.0066 (4.7%)
49-64	0.1983 ± 0.0524 (26.4%) ± 0.0127 (6.4%)	51-59	0.1096 ± 0.0355 (32.4%) ± 0.0050 (4.7%)
65-300	0.2408 ± 0.0618 (25.7%) ± 0.0189 (7.8%)	60-73	0.1535 ± 0.0426 (27.8%) ± 0.0089 (5.8%)
		74-102	0.1993 ± 0.0500 (25.%) ± 0.0173 (6.7%)
		103-350	0.0872 ± 0.0330 (37.8%) ± 0.0111 (12.8%)

Table 3.9: Relative $\psi(2S)$ yield per multiplicity interval at forward and backward rapidity.

Forward rapidity region		Backward rapidity region	
N_{trk}^{corr}	$N_{\psi(2S)}$-over-$N_{J/\psi}$ ± stat ± syst	N_{trk}^{corr}	$N_{\psi(2S)}$-over-$N_{J/\psi}$ ± stat ± syst
1-20	0.0180 ± 0.0038 (27.0%) ± 0.0016(3.8%)	1-18	0.0147 ± 0.0036 (27.0%) ± 0.0017 (6.0%)
21-32	0.0163 ± 0.0038 (25.4%) ± 0.0017 (5.5%)	19-27	0.0137 ± 0.0036 (28.6%) ± 0.0016 (5.0%)
33-40	0.0234 ± 0.0048 (22.5%) ± 0.0017 (6.7%)	28-41	0.0115 ± 0.0027 (25.7%) ± 0.0015 (6.6%)
41-48	0.0199 ± 0.0051 (27.5%) ± 0.0020 (6.9%)	42-50	0.0153 ± 0.0033 (24.0%) ± 0.0015 (4.5%)
49-64	0.0165 ± 0.0042 (26.5%) ± 0.0017 (6.5%)	51-59	0.0125 ± 0.0038 (32.4%) ± 0.0013 (4.7%)
65-300	0.0143 ± 0.0034 (25.7%) ± 0.0018 (7.7%)	60-73	0.0134 ± 0.0035 (27.8%) ± 0.0014 (6.0%)
		74-102	0.0148 ± 0.0034 (25.%) ± 0.0018 (8.6%)
		103-350	0.0178± 0.0065 (37%) ± 0.0024 (11.8%)

Table 3.10: Relative ψ(2S)-over-J/ψ yield ratio per multiplicity interval at forward and backward rapidity.

3.5.1 Normalization factor

The data sample used to extract charmonium yields includes only MB events with two opposite charge muons, i.e., CMUL7 events. We correct the number of CMUL7 events in each multiplicity interval i, N^i_{CMUL7}, by a normalization factor to evaluate the equivalent number of MB events where no specific selections are applied. The equivalent number of MB events $N^{\mathrm{eq}}_{\mathrm{MB}}$, which corresponds to the number of dimuon analyzed events N_{CMUL7}, is obtained as:

$$N^{\mathrm{eq},i}_{\mathrm{MB}} = F^i_{\mathrm{norm}} \times N^i_{\mathrm{CMUL7}}, \tag{3.10}$$

where:

- $N^{\mathrm{eq},i}_{\mathrm{MB}}$ is the number of MB events in the multiplicity interval i.
- F^i_{norm} is the normalization factor in the multiplicity interval i.
- N^i_{CMUL7} is the number of CMUL7 events in the multiplicity interval i.

To obtain the F^i_{norm}, two different "offline" methods are used in this analysis. Both methods compare the physics-selected MB event sample to those containing dimuon trigger (MUL) input. The first offline method can be obtained as in the following equation:

$$F^{\mathrm{off1},i}_{\mathrm{norm}} = \frac{N^i_{\mathrm{MB}}}{N^i_{\mathrm{MB\&0MUL}}}, \tag{3.11}$$

in which the normalization factor is evaluated directly from the ratio of the MB events to a sub-sample of the MB events, which requires an opposite-charge dimuon trigger (0MUL) to be fired. This method suffers from the low statistics in the MB&0MUL events sample. To improve the statistical precision of the method, an indirect normalization approach is followed:

$$F^{\mathrm{off2},i}_{\mathrm{norm}} = \frac{N^i_{\mathrm{MB}}}{N^i_{\mathrm{MB\&0MSL}}} \times \frac{N^i_{\mathrm{CMSL7}}}{N^i_{\mathrm{CMSL7\&0MUL}}}, \tag{3.12}$$

where the MSL trigger is used as an intermediate trigger to evaluate the normalization factor. The MSL trigger requires at least one single muon to be detected in coincidence with a MB trigger. This trigger has higher statistics than the 0MUL trigger.
The normalization factor as a function of the run number evaluated by the indirect method is presented in Fig.3.12 for the forward and backward rapidity regions. The central F_{norm} value is evaluated as the weighted average over all the run numbers in a data-taking period,

for the forward and backward rapidity data set, as in the following equation:

$$F_{\text{norm}} = \frac{\sum_{i=1}^{n} F_{\text{norm}}^{i} \times N_{\text{CMUL7}}^{i}}{\sum_{i=1}^{n} N_{\text{CMUL7}}}, \tag{3.13}$$

where n is the number of runs analyzed. In Fig.3.12, we observe that the F_{norm} values at forward rapidity are about twice those at backward rapidity. This is due to the fact that the muon spectrometer in the backward rapidity region measures the muons in the Pb fragmentation side, which increases the probability of detecting a muon or a dimuon in a MB event. The values of the normalization factor over integrated multiplicity as well as in multiplicity intervals are reported in Tab.3.11 and Tab.3.12 for the forward and backward rapidity region data sets, respectively. In this analysis, we consider the $F_{\text{norm}}^{\text{off2}}$ for the charmonium corrected yields determination.

Forward rapidity region			
N^{corr}	$F_{\text{norm}}^{\text{off1}}$	$F_{\text{norm}}^{\text{off2}}$	$F_{\text{norm}}^{\text{off1}} / F_{\text{norm}}^{\text{off2}}$
0-300	680.67 ± 5.76	680.03 ± 1.53	1.001 ± 0.008
1-20	2418.37 ± 45.06	2397.46 ± 14.33	1.009 ± 0.019
21-32	892.28 ± 21.38	879.15 ± 5.23	1.015 ± 0.024
33-40	649.83 ± 19.51	625.91 ± 4.18	1.038 ± 0.031
41-48	494.66 ± 8.76	510.52 ± 3.26	0.969 ± 0.017
49-64	410.93 ± 7.77	407.98 ± 2.47	1.007 ± 0.013
65-300	281.24 ± 7.63	276.52 ± 1.13	1.017 ± 0.028

Table 3.11: Normalization factor measurement in the forward rapidity region.

Backward rapidity region			
N^{corr}	$F_{\text{norm}}^{\text{off1}}$	$F_{\text{norm}}^{\text{off2}}$	$F_{\text{norm}}^{\text{off1}} / F_{\text{norm}}^{\text{off2}}$
0-350	372.89 ± 1.14	372.59 ± 0.42	1.001 ± 0.003
1-18	2517.31 ± 40.74	2484.21 ± 11.27	1.013 ± 0.016
19-27	867.88 ± 10.96	843.36 ± 3.57	1.029 ± 0.013
28-41	462.83 ± 3.63	463.17 ± 1.30	0.999 ± 0.008
42-50	299.41 ± 2.68	296.95 ± 0.97	1.008 ± 0.009
51-59	223.41 ± 1.96	222.95 ± 0.73	1.002 ± 0.009
60-73	166.86 ± 1.23	165.95 ± 0.47	1.005 ± 0.007
74-102	109.99 ± 0.72	110.31 ± 0.29	0.997 ± 0.007
103-350	66.01 ± 0.80	65.45 ± 0.28	1.009 ± 0.012

Table 3.12: Normalization factor measurements in the backward rapidity region.

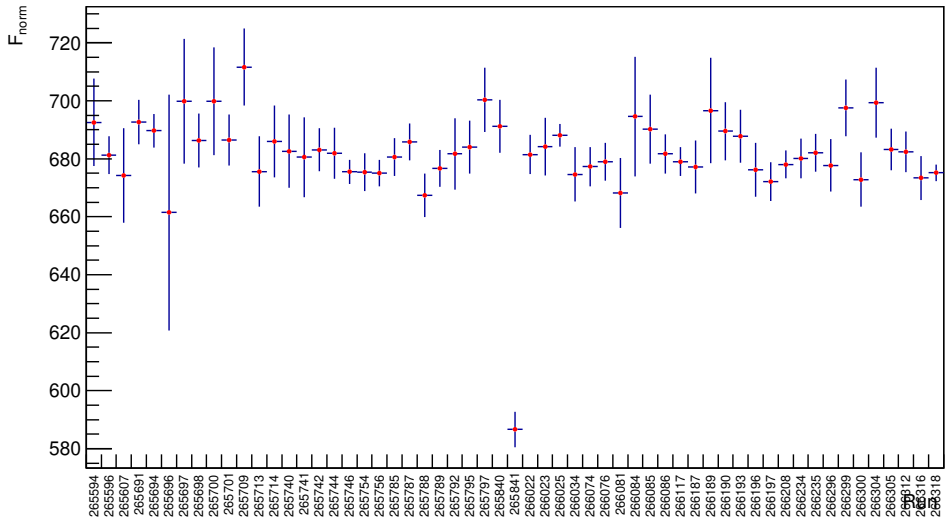

(a) Forward rapidity

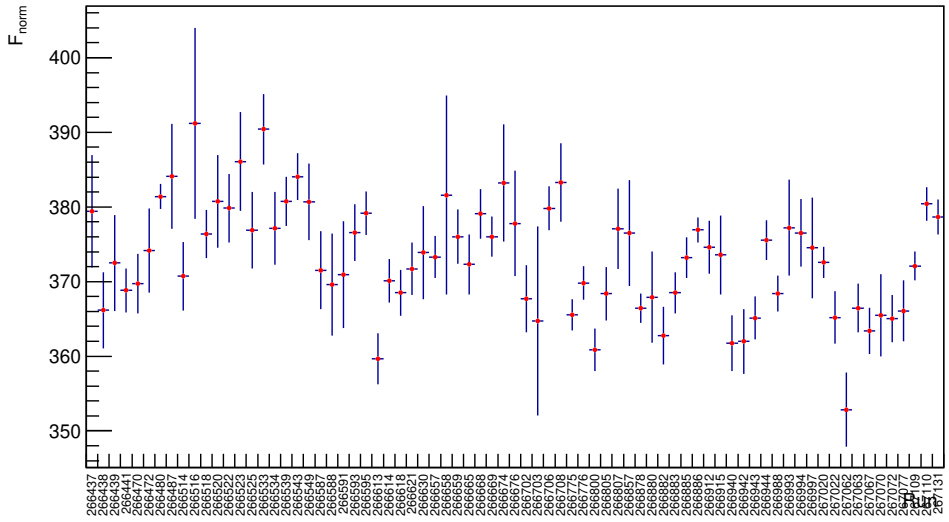

(b) Backward rapidity

Figure 3.12: Dimuon trigger normalization factor at forward and backward rapidity as a function of the *run number*. The normalization factor in this plot is evaluated using the indirect offline ($F_{\text{norm}}^{\text{off2},i}$) method over the integrated multiplicity.

3.5.2 Dimuon acceptance times efficiency

This section investigates the possible variations of the $A \times \varepsilon$ as a function of charged-particle multiplicity. No $A \times \varepsilon$ variation is expected in p–Pb collisions in terms of detector occupancy. However, the p_{T}, y distributions of the charmonium yields may change as a function of multiplicity which may lead to such effect [83]. A data-driven iterative procedure is performed in order to tune the MC p_{T} and y distributions to the ones extracted from the data. The $A \times \varepsilon$ is evaluated for the integrated multiplicity interval and for each multiplicity interval. Due to the limited statistics of $\psi(2S)$, it was not possible to extract p_{T} and y distributions from data in all multiplicity intervals, and do the iterative procedure. As a consequence, the exercise was performed for J/ψ, and we assumed that the evolution of the $A \times \varepsilon$ as a function of charged-particle multiplicity is the same for both charmonium states.

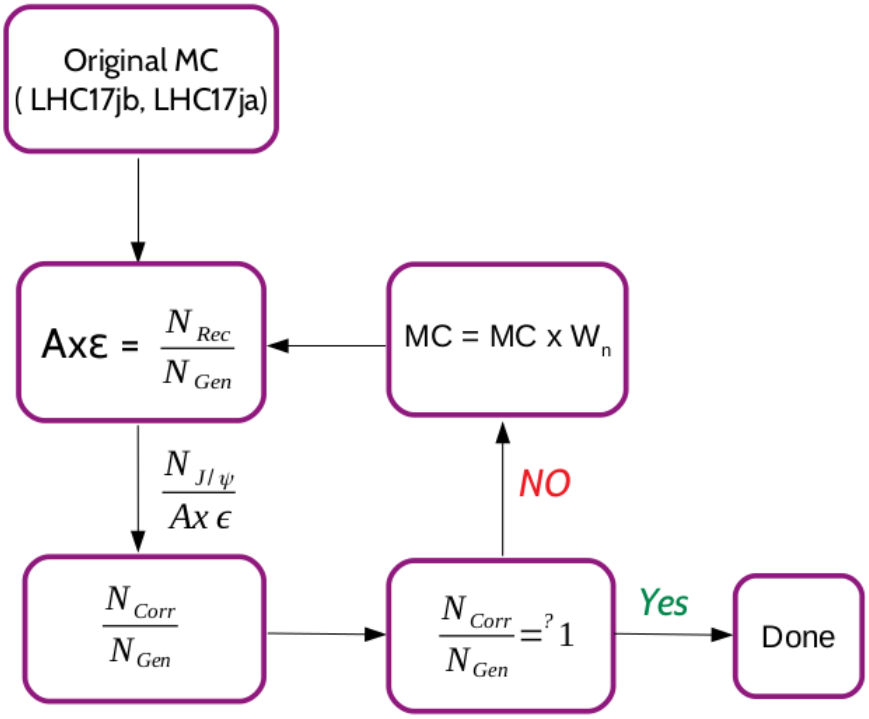

Figure 3.13: Flowchart of the data-driven iterative procedure.

The flow chart of Fig.3.13 illustrates the data-driven iterative procedure. First, the p_{T} and y distributions are extracted from MC. Then, the initial value of the $A \times \varepsilon$ is evaluated as the ratio of the MC reconstructed to generated distributions. In order to tune the MC distributions on data, for each multiplicity interval, the J/ψ raw yields are extracted in five p_{T}

ranges for the integrated y range, and four y ranges for the integrated p_{T} range. To perform this extraction, the invariant mass spectra in each p_{T} and y range are fitted using the same fit configurations mentioned in Sec.3.4.1. The p_{T} and y distributions extracted from data are then corrected by the $A \times \varepsilon(y, p_{\mathrm{T}})$ to obtain the corrected yields $N^{\mathrm{corr}}(y, p_{\mathrm{T}})$. Next, the corrected yield distributions are compared to their corresponding generated distributions by evaluating their respective ratio. This ratio tends to be unity if the MC simulations are realistic. Otherwise, a weight ($w(p_{\mathrm{T}}, y)$) is evaluated from this ratio (via a fit) and applied to the MC distributions at the next iteration step. Figure 3.14 presents the resultant J/ψ p_{T} and y integrated $A \times \varepsilon$ values for different iterations in each multiplicity interval, for the forward rapidity region in the top panel and backward rapidity region in the bottom panel. It can be seen that 2-3 iterations are enough to converge. The $A \times \varepsilon$ values increase slightly from the initial, i.e., no-weight case, to the first iteration and then tend to fluctuate. No multiplicity dependence of the $A \times \varepsilon$ is observed in the measurement multiplicity intervals. As a consequence, the procedure has been repeated for the integrated-multiplicity sample, to benefit from the higher statistics in the integrated case.

The results of the multiplicity integrated exercise, performed in fine p_{T} and y intervals, showed no influence on the simulated distributions, as expected for measurements in fine bins. The iterative procedure was also done using the same number of p_{T} and y bins that can be used in the multiplicity intervals measurement to observe possible discrepancies. Five bins of p_{T} and four bins of y were considered to extract and correct J/ψ raw yields. The considered variation of the simulated distributions per iteration in the multiplicity-integrated exercise is shown in Fig.3.15. The influence of these variations on the p_{T} and y averaged efficiency is presented in Fig.3.16, and amounts to 3% and 6% for forward and backward rapidity ranges. These values are consistent with those obtained in multiplicity intervals. These results are summarized in Tab. 3.13.

Forward rapidity			Backward rapidity		
N^{corr}	$A \times \epsilon$	$\frac{A \times \epsilon}{A \times \epsilon(\mathrm{integrated})}$.	N^{corr}	$A \times \epsilon$	$\frac{A \times \epsilon}{A \times \epsilon(\mathrm{integrated})}$.
int.	0.2733	1.0	int.	0.2446	1.0
1-20	0.2708	0.9908	1-27	0.2358	0.9638
21-32	0.2727	0.9978	28-41	0.2478	1.0129
33-40	0.2765	1.0117	42-50	0.2455	1.0035
41-48	0.2702	0.9886	51-59	0.2474	1.0112
49-64	0.2748	1.0054	60-88	0.2384	0.9744
65-300	0.2737	1.0015	89-350	0.2455	1.0035

Table 3.13: Multiplicity dependence of J/ψ $A \times \epsilon$ in the last iteration step. The ratio to the integrated value is also quoted.

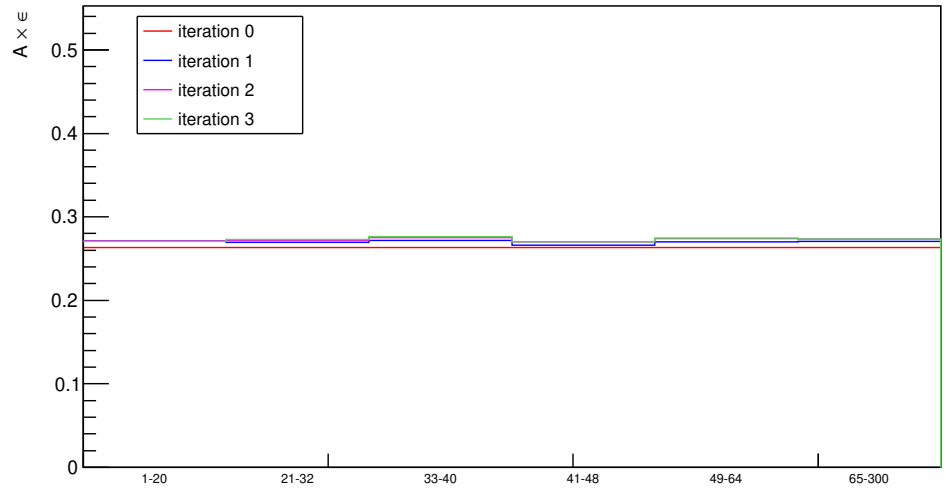

(a) Forward rapidity

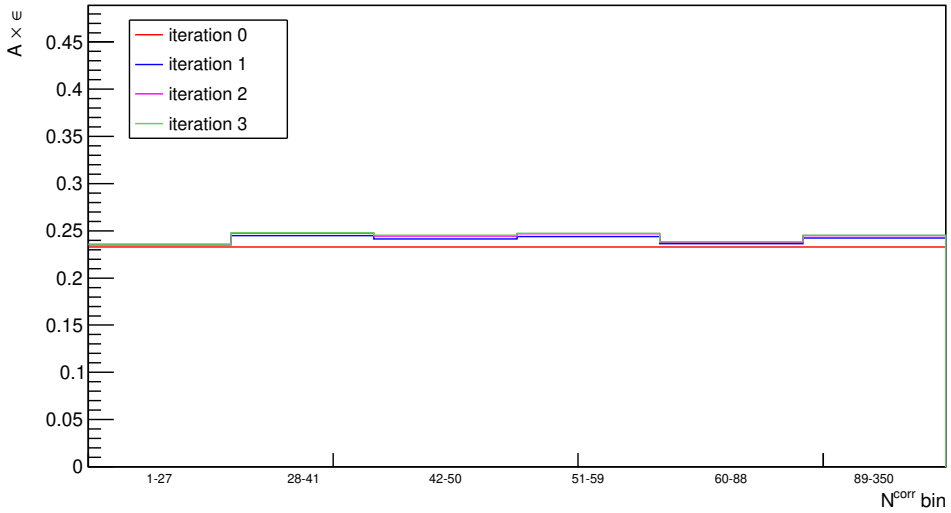

(b) Backward rapidity

Figure 3.14: Result of the iterative procedure for the J/ψ $A \times \varepsilon$ for each multiplicity interval at forward (a) and backward (b) rapidity.

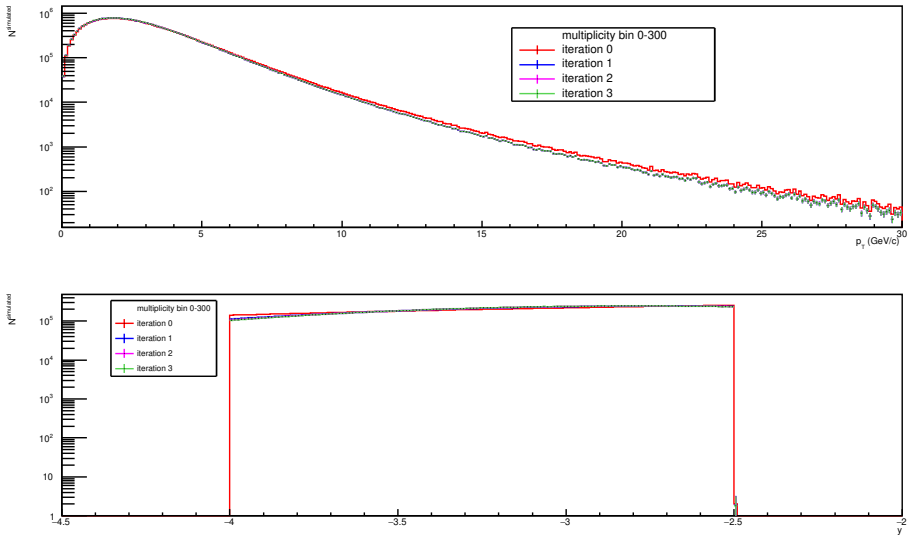

(a) Forward rapidity

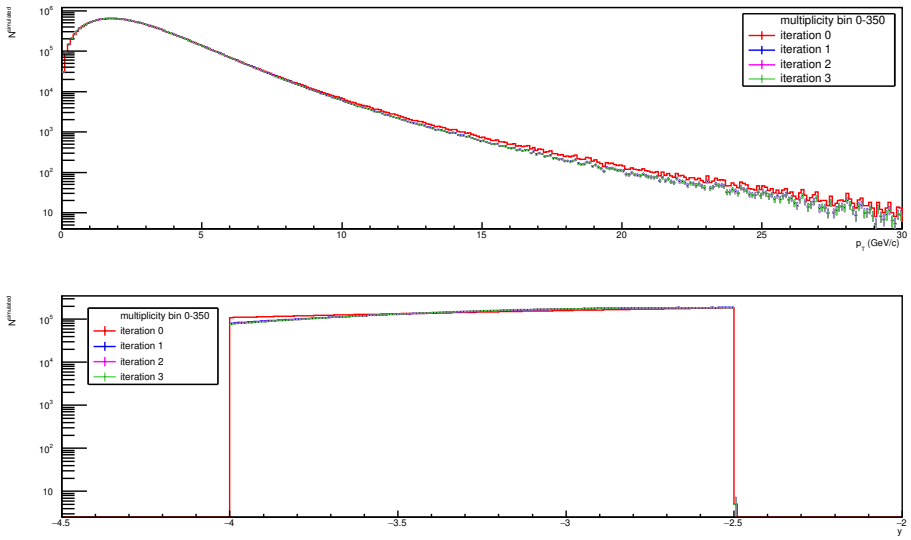

(b) Backward rapidity

Figure 3.15: Generated J/ψ p_{T} and y distributions at each iteration step.

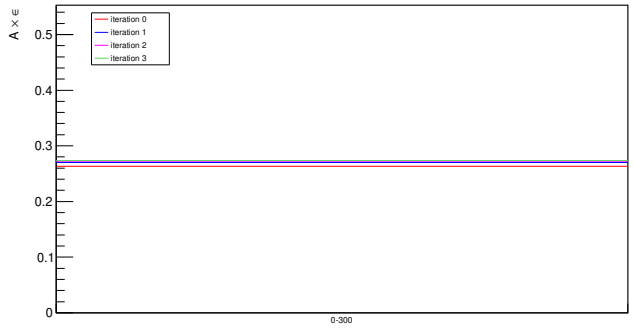

(a) Forward rapidity

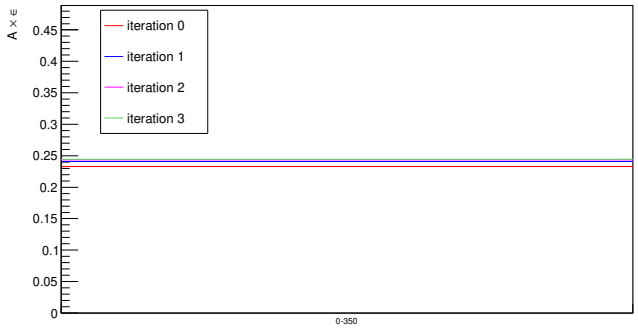

(b) Backward rapidity

Figure 3.16: Average J/ψ $A \times \epsilon$ for various iteration steps for the multiplicity-integrated case.

3.5.3 Trigger efficiency evaluation

The multiplicity measurement is performed in the non-single diffractive (NSD) event class. The measurement needs to be corrected by the efficiency of the MB trigger to select NSD events with a reconstructed SPD vertex that passes the QA criteria.

Trigger efficiency evaluation in the integrated multiplicity interval

The trigger efficiency evaluation for the integrated multiplicity interval was carried out in an independent analysis [78]. The trigger efficiency was assessed from two MC samples, using one run for each of the forward and backward data sets of p–Pb collisions. One of the MC samples was generated with the HIJING event generator, and the other one with the DPMJET event generator. The ESD[1] data was used to perform the estimation. HIJING 1.36 [84] is based on combining the perturbative QCD process with the soft interactions. DPMJET [79] is based on the Gribov-Glauber approach and treats both soft and hard scatterings similarly. The particles generated with the previous event generators are then transported through the detector using GEANT 3 software package [85]. The trigger efficiency for the NSD events with vertex reconstructed that passed the selections is $\epsilon^{\mathrm{MB}} = 97.4 \pm 1\%$ [78].
In this analysis, we adopt the same procedure to evaluate the trigger efficiency in multiplicity intervals as in Ref.[78]. The trigger efficiency in the integrated multiplicity interval was evaluated using the ESD data, while we are using AOD[2] data for the data analysis. To understand the potential impact of evaluating the efficiency using AOD instead of ESD on the result, we compute the trigger efficiency in the integrated multiplicity interval for one run from AOD data, and compare it to the corresponding value estimated using ESD data. The MB trigger efficiency to select the NSD events is defined as:

$$\epsilon^{MB} = 1 + f^{NSD}_{noVtx} - f^{data}_{noVtx}/\rho_{MC}\,, \tag{3.14}$$

where,

- f^{NSD}_{noVtx} is the fraction of NSD-generated events in which no vertex is reconstructed or selected.
- f^{data}_{noVtx} is the fraction of reconstructed events in data with no vertex selected.
- ρ_{MC} is the MC efficiency for events with no vertex.

[1] ESD stands for Event Summary Data.
[2] AOD stands for Analysis Object Data, and is a filtered and reduced version of ESD.

The value of f^{NSD}_{noVtx} is evaluated as:

$$f^{NSD}_{noVtx} = \frac{N^{MC}_{NSD} - N^{MC}_{selectedVtx}}{N^{MC}_{MB}}, \tag{3.15}$$

where N^{MC}_{NSD} is the number of NSD generated events, $N^{MC}_{selectedVtx}$ is the number of reconstructed events with selected vertex, and N^{MC}_{MB} is the number of generated MC events that pass the MB trigger. To compute ρ_{MC}, one needs to define the fraction of reconstructed events in MC with no selected vertex, which can be evaluated as:

$$f^{MB-MC}_{noVtx} = \frac{N^{MC}_{MB} - N^{MC}_{selectedVtx}}{N^{MC}_{MB}}, \tag{3.16}$$

where $N^{MC}_{selectedVtx}$ is the number of reconstructed MC events with selected vertex. Then, ρ_{MC} can be evaluated as

$$\rho_{MC} = \frac{f^{MB-MC}_{noVtx}}{f^{NSD}_{noVtx}}. \tag{3.17}$$

Finally, we obtain

$$f^{data}_{noVtx} = \frac{N^{data}_{MB} - N^{data}_{selectedVtx}}{N^{data}_{MB}}, \tag{3.18}$$

where N^{data}_{MB} is the number of reconstructed MB events, $N^{data}_{selectedVtx}$ is the number of reconstructed MB events with selected vertex.
Using AOD sample for run 266318: $f^{NSD}_{noVtx} = 0.0125$ and $f^{MB-MC}_{noVtx} = 0.0042$. Using Eq.3.17, $\rho_{MC} = 33.88\%$. From data, $N^{data}_{MB} = 0.0177$. The ϵ^{MB} estimated from our DPMJET AODs was $\epsilon^{MB} = 0.9779$, which is consistent with the value evaluated in Ref.[78].

Trigger efficiency evaluation in multiplicity intervals

We used the equations in the previous section to evaluate the MB trigger efficiency to select NSD events per multiplicity interval in each period. First, the trigger efficiency is evaluated for each *run number* and for each multiplicity interval. Then the central value is computed as the weighted average over all the run numbers. We used the number of CINT7 events in each run as a weight. The values obtained for the integrated multiplicity interval and multiplicity intervals for each period are reported in Tab.3.14. A decrease of the trigger efficiency is found for the two lowest multiplicity intervals. This points to the fact that the vertex finding algorithm encounters difficulties in finding track candidates to reconstruct the vertex at low multiplicity.

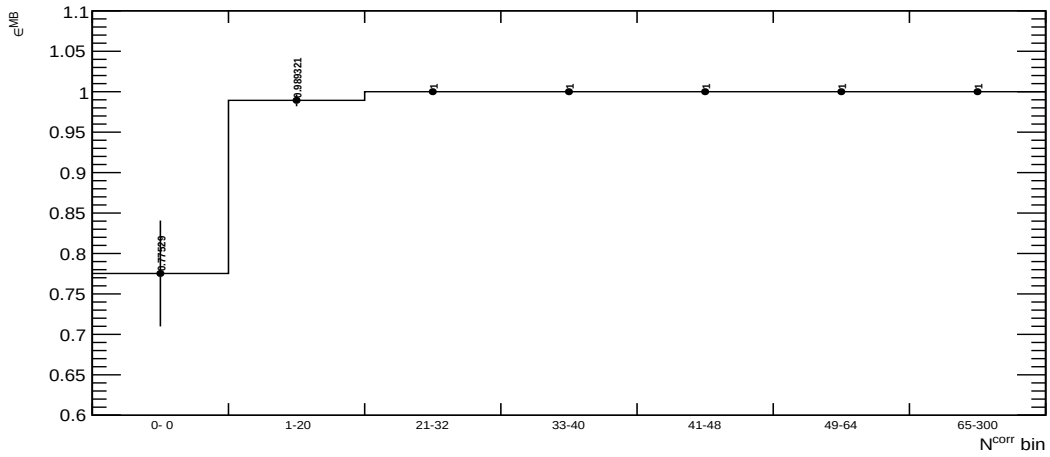

(a) Forward rapidity

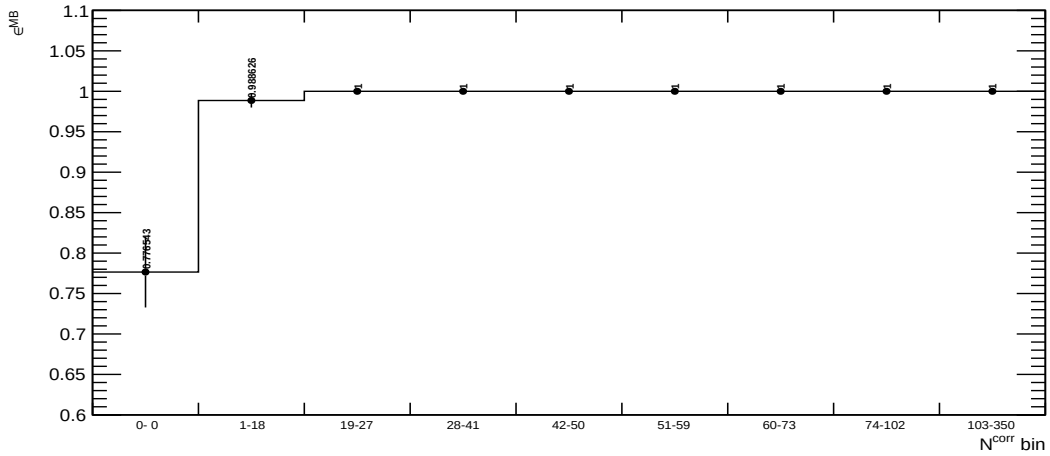

(b) Backward rapidity

Figure 3.17: MB trigger efficiency in multiplicity intervals.

Forward rapidity region		Backward rapidity region	
N^{corr} bin	ϵ^{NSD} (%)	N^{corr} bin	ϵ^{NSD} (%)
0-300	96.89 ± 0.74	0-350	96.90 ± 0.51
1-300	99.59 ± 0.28	1-350	99.60 ± 0.30
0-1	77.53 ± 6.54	0-1	77.65 ± 4.38
1-20	98.93 ± 0.73	1-18	98.86 ± 0.87
21-32	100	19-27	100
33-40	100	28-41	100
41-48	100	42-50	100
49-64	100	51-59	100
65-300	100	60-73	100
		74-102	100
		103-350	100

Table 3.14: NSD trigger efficiency in the measurement multiplicity intervals (in percentage).

3.6 Sources of systematic uncertainties

Several sources of systematic uncertainties contribute to charmonium yield extraction. These are: (i) signal extraction, (ii) normalization factor, (iii) the effect of the resolution and pile-up on the multiplicity classification, (iv) vertex equalization, (v) the acceptance times efficiency correction and (vi) the MB trigger efficiency. The following sections discuss these sources of systematic uncertainties.

3.6.1 Signal extraction

The uncertainty on the signal extraction was discussed in Sec.3.4.2. To summarize, several signal and background configuration combinations are used to extract the charmonium yields in two mass fit ranges. The largest impact on the number of candidates originates from the different tail parametrizations used (data vs. MC). The average yield and the uncertainties extracted over all the trials are weighted to balance the number of tests using tails from MC and data. In the integrated multiplicity, the uncertainty amounts to about 3.6% (3.7%) and 12.0% (12.8%) in the forward (backward) rapidity range for the raw yields of J/ψ and ψ(2S), respectively. In multiplicity intervals, the systematic uncertainty ranges between (3.5 – 3.9)% and (9.6 – 16.0)% for the raw yields of J/ψ and ψ(2S), respectively.
In the case of the relative raw yields, we assumed that the uncertainty is partially correlated with multiplicity. The systematic uncertainty ranges between (0.6–1.4)% and (3.8-12.8)% for the relative yields of J/ψ and ψ(2S), respectively. In the case of the ψ(2S)-over-J/ψ relative

yields, we found that the systematic uncertainty varies between (3.8-11.8)%.

3.6.2 Normalization factor

Two methods are used to compute the normalization factor from which the systematic uncertainty is estimated. We studied the bin-by-bin spread of the normalization factor evaluated from each method. In both periods, all the values are found to be within 2.5% of the central values. We assign the 2.5% as the systematic uncertainty from the normalization factor for the relative J/ψ and ψ(2S) relative yield measurement. In the case of ψ(2S)-over-J/ψ, the uncertainty resulting from the normalization factor cancels out.

3.6.3 The multiplicity axis resolution and pile-up

Similar to the J/ψ analysis [63], the uncertainty on the multiplicity axis resolution and the pile-up is evaluated as a single contribution. Two effects are considered to evaluate the uncertainty due to the multiplicity resolution: the bin flow due to randomization seed and the bin flow due to edge effect. The uncertainty coming from pile-up and multiplicity resolution is estimated by extracting the charmonium yields with a different randomization seed for the event-by-event correction, or introducing a small shift to the N^{corr} intervals ($\mathrm{bin}_{\mathrm{offset}} = \pm 0.1$), or by changing the pile-up rejection criteria. The maximum spread of the yields extracted from these variations from the central values in both forward and backward rapidity regions is within 2%, which is assigned as a systematic uncertainty. The major contribution to this uncertainty comes from the pile-up rejection criteria, meaning the same influence is expected for J/ψ and ψ(2S). The limited statistics of the ψ(2S) analysis do not allow for a more precise determination of this uncertainty. Therefore, a 2% uncertainty is also assigned to the raw yields of ψ(2S). In the case of the relative yields, the systematic uncertainty is considered to be negligible.

3.6.4 Vertex equalization

The uncertainty from vertex equalization is estimated by comparing the values of the charmonium yields extracted when considering a variation on the equalization procedure to correct the data. In particular, in one case the Poissonian vertex equalization with respect to the maximum of $N_{\mathrm{tr}}(v_z)$ was used, while in the other the binomial vertex equalization with respect to the minimum of the $N_{\mathrm{tr}}(v_z)$ was considered. The systematic uncertainty from the vertex equalization is taken from Ref.[78] and amounts to 2%.

3.6.5 Acceptance times efficiency

We described the $A \times \varepsilon$ measurement in Sec.3.5.2. In summary, the iterative procedure is performed considering a realistic p_{T} and y distribution for J/ψ, resulting in a small increase of the average value by a similar amount in all measurement multiplicity intervals. Table 3.13 summarizes the iterative procedure results for J/ψ. The values of the $A \times \epsilon$ for the last iteration step fluctuate by at most 1% (4%) in the measurement multiplicity intervals for the forward (backward) rapidity range.

3.6.6 Summary of systematic uncertainties

Tab.3.15 summarizes the systematic uncertainties for ψ(2S) raw and relative yields. Similarly, Tab.3.16 summarizes the systematic uncertainties of the J/ψ-over-ψ(2S) raw and relative yields.

sources	Forward rapidity region		Backward rapidity region	
	raw yields	rel. yields	raw yields	rel. yields
signal extraction	10-13% (11.8%) $\diamond$	4-8% $\diamond$	13-16% (12.8%) $\diamond$	5-13% $\diamond$
F_{norm}	2.5%	–	2.5%	–
bin-flow and pile-up	2.0%	2.0%	2.0%	2.0%
vertex equalisation	2.1%	2.1%	2.1%	2.1%
$A \times \epsilon$	1.0%	–	4.0%	–
event class norm.	1.0%*	1.0%*	1.0%*	1.0%*

Table 3.15: Summary of the systematic uncertainties for ψ(2S). The $*$ ($\diamond$) marker points to the values that are (partially) correlated with multiplicity.

sources	Forward rapidity region		Backward rapidity region	
	raw yields	rel. yields	raw yields	rel. yields
signal extraction	7-13% (9%) $\diamond$	4-8% $\diamond$	11-13% (10%) $\diamond$	5-12% $\diamond$
F_{norm}	negl.	negl.	negl.	negl.
bin-flow and pile-up	negl.	negl.	negl.	negl.
vertex equalisation	negl.	negl.	negl.	negl.
$A \times \epsilon$	1.0%	–	4.0%	–
event class norm.	1.0%*	1.0%*	1.0%*	1.0%*

Table 3.16: Summary of the systematic uncertainties for ψ(2S)-over-J/ψ. The $*$ ($\diamond$) marker points to the values that are (partially) correlated with multiplicity.

4

Results and discussion on multiplicity dependence of charmonium production

In this chapter, we present the measurement of the self-normalized charmonium (J/ψ and ψ(2S)) yields as a function of charged-particle multiplicity in p–Pb collisions at $\sqrt{s_{\rm NN}}$ = 8.16 TeV, using the ALICE detector at the LHC (CERN). The charmonium yields are measured at forward (2.03 < $y_{\rm cms}$ < 3.53) and backward (-4.46 < $y_{\rm cms}$ < -2.96) rapidity regions in their decay channel into dimuon, while the charged-particle multiplicity is measured at midrapidity ($|y_{\rm lab}| < 1$). The multiplicity dependent measurement of the charmonium yields and the excited-over-ground state ratio in p–Pb collisions are discussed in the first section. The comparison to the available model calculations is displayed for each measurement. In the second section, the measurements of the multiplicity dependence of the charmonium and bottomonium yields in pp collisions are reported. The third section discusses the open-heavy flavor multiplicity dependent measurements in pp collisions.

4.1 Charmonium multiplicity dependence in p–Pb collisions at $\sqrt{s_{\rm NN}}$ = 8.16 TeV

4.1.1 ψ(2S) results

The measured ψ(2S) self-normalized yields, in p–Pb collisions at $\sqrt{s_{\rm NN}}$ = 8.16 TeV, are presented in Fig.4.1 as a function of midrapidity ($|y_{\rm lab}| < 1$) charged-particle multiplicity. The results presented in this thesis have been published in Ref.[83]. The results are reported for the charmonium yields extracted at forward ($2.03 < y_{\rm cms} \leq 3.53$) and backward ($-4.46 < y_{\rm cms} < -2.96$) rapidity. The statistical and systematic uncertainties are depicted with

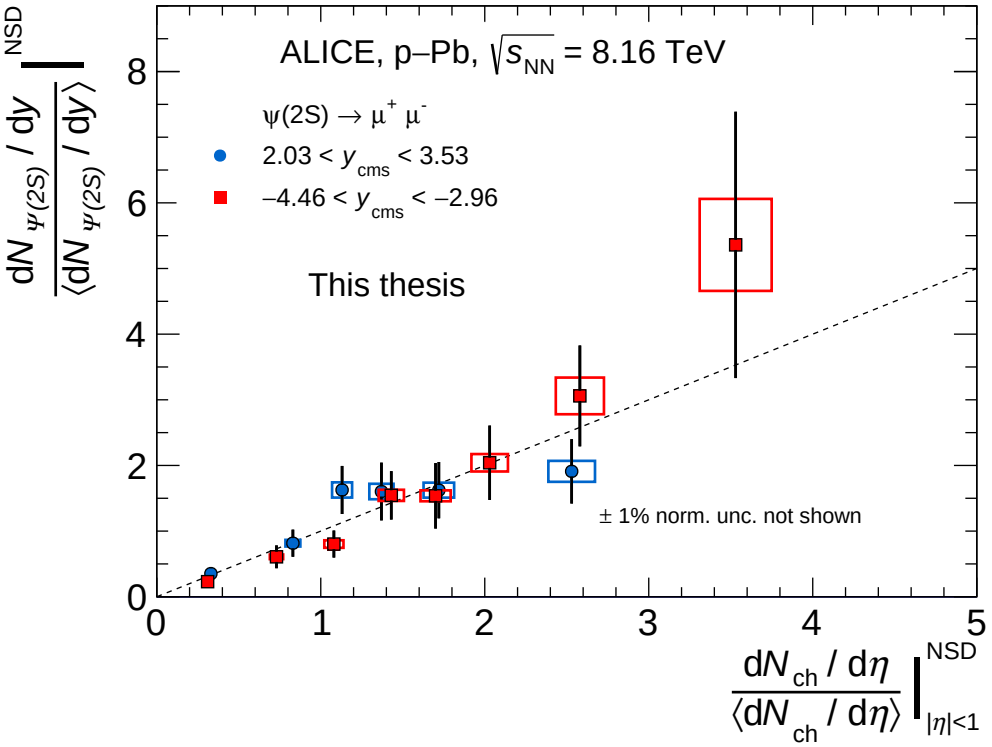

Figure 4.1: ψ(2S) self-normalized yields as a function of charged-particle multiplicity in p–Pb collisions at $\sqrt{s_{\rm NN}}$ = 8.16 TeV. The yields are measured at the forward (backward) rapidity region depicted with the blue (red) marker. The vertical error bars represent the statistical uncertainties of the yields, whereas the width and the height of the box give the systematic uncertainty of the multiplicity and the yields, respectively. The dashed line is the one-to-one correlation between the x- and y-axis to guide the eye.

vertical lines and boxes, respectively. In both rapidity regions, the measurement shows an

increase of the self-normalized yields with increasing multiplicity, compatible with a linear ($y = x$) increase depicted with a dashed line in the plot.

In Fig.4.2, the ψ(2S) self-normalized yields are compared to the theoretical calculation from the percolation + comover + EPS09 model [41, 57, 58, 86–88]. The percolation model is based on parton saturation or string interactions. The main assumption of this model is that in high-energy heavy ion collisions, a high-density partonic medium is formed with characteristic properties such as shear viscosity and high opacity. Each parton-parton collision contains the formation of the fundamental source of particle production, called flux tubes (strings), as considered by the model. In this framework, the number of parton-parton interactions is reflected by the number of produced strings. These strings have a certain transverse size and different space-time rapidity, and they can interact (overlap) with each other reducing their total effective number. In the case of quarkonium production, particularly of charmonia, the number of initially produced charmonia is proportional to the number of collisions in analogy to any hard process; in this model, it is then proportional to the number of produced strings. On the other hand, the charged-particle multiplicity distribution, mainly soft particles, is proportional to the number of participant strings [57, 58]. In the theoretical calculation presented in Fig.4.2, the percolation model is coupled to the calculation from the comover model and the parameterization from EPS09 nuclear parton distribution functions. The comover model describes the dissociation of charmonia due to their interaction with the produced soft particles that travel along with them. There are two common features of the comover model. First, the comover dissociation affects the ψ(2S) more than the J/ψ, due to the larger size of the first, i.e., a weaker binding between the two quarks of the charmonia state. Second, the comover suppression is stronger when the comover densities are larger [41, 86], i.e., at larger multiplicity. EPS09 is a parameterization at LO and NLO, of the nuclear parton distribution functions (nPDF). EPS09 uses the data from deep-inelastic lepton-nucleus scattering measurements, the Drell-Yan dilepton production data from fixed target proton-nucleus collisions, and the neutral-pion production data measured in d+A and pp collisions at RHIC. The uncertainty of the model originates from the uncertainty on data and is evaluated using the Hessian method [87, 88]. As shown in Fig.4.2, the percolation + comover + EPS09 model describes the multiplicity dependence of the self-normalized ψ(2S) production within uncertainties at both forward and backward rapidity.

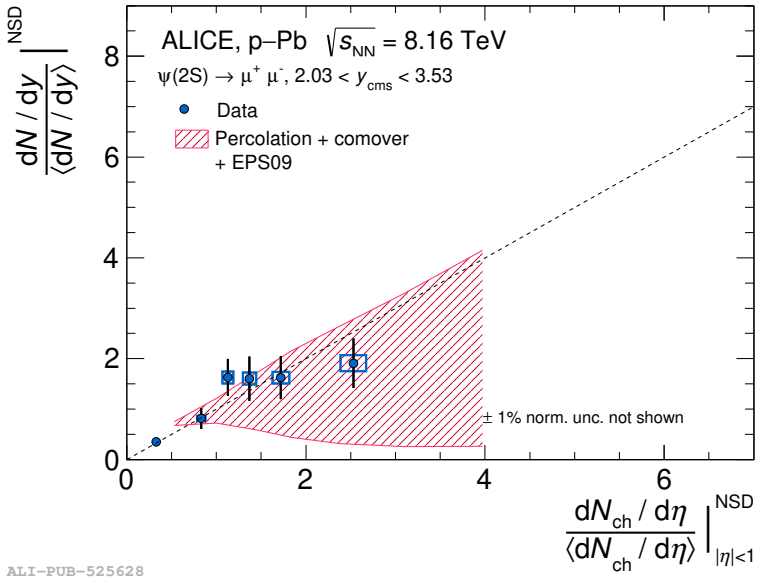

(a) Forward rapidity

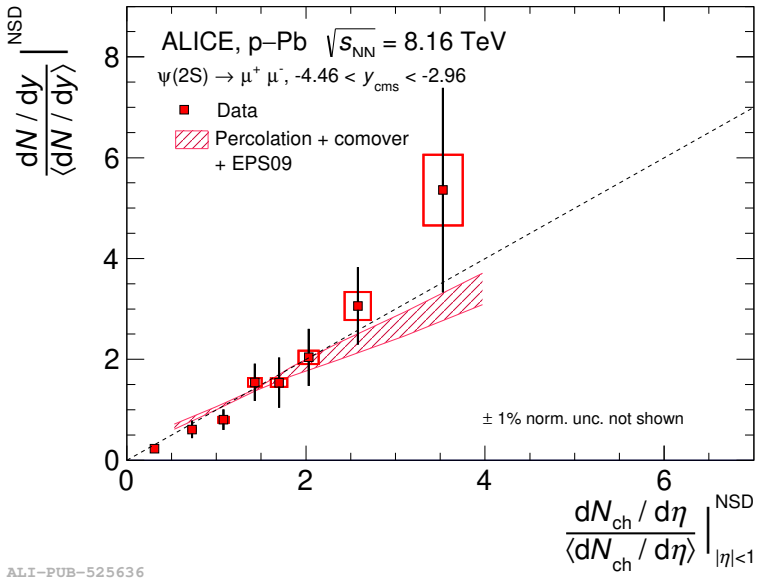

(b) Backward rapidity

Figure 4.2: Self-normalized ψ(2S) yields as a function of self-normalized charged-particle multiplicity from p–Pb collisions at $\sqrt{s_{NN}}$ = 8.16 TeV [83], for ψ(2S) measured at (a) forward rapidity, and (b) backward rapidity in the top and bottom panel, respectively. The results are compared to the percolation + comover + EPS09 model calculation [41, 57, 58, 86–88].

4.1.2 J/ψ results

The self-normalized yields of J/ψ as a function of the self-normalized charged-particle multiplicity have been measured by ALICE in p–Pb collisions at $\sqrt{s_{\rm NN}}$ = 8.16 TeV [63]. The J/ψ yields are measured at forward ($2.03 < y_{\rm cms} < 3.53$) and backward ($-4.46 < y_{\rm cms} < -2.96$) rapidity from their decay channel into dimuon. The charged-particle multiplicity is measured at midrapidity ($|\, y_{\rm lab}\,| < 1$). The J/ψ results are presented as a function of charged-particle multiplicity in Fig.4.3 [63]. Thanks to the larger abundance of J/ψ, with respect to ψ(2S),

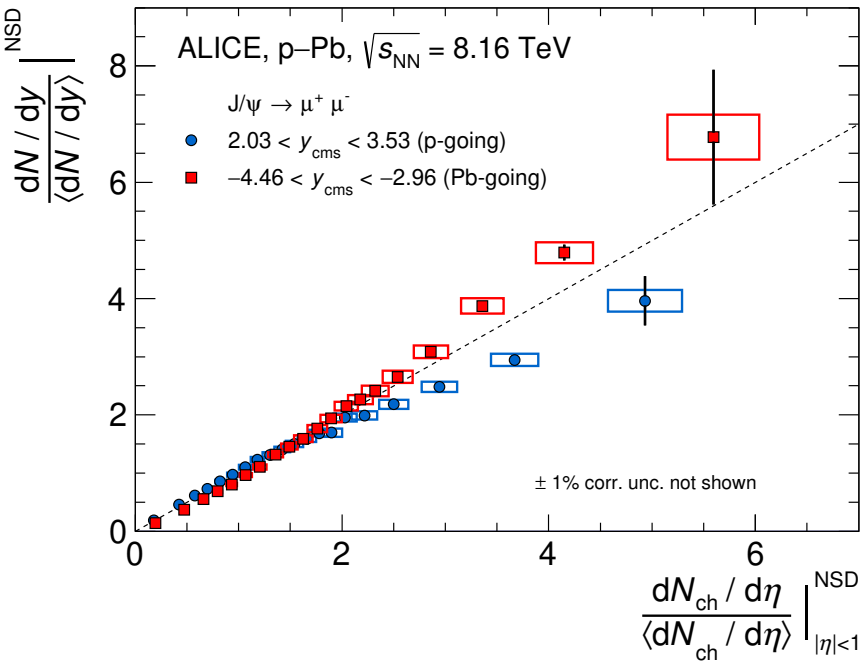

Figure 4.3: Self-normalised J/ψ yields as a function of midrapidity charged-particle multiplicity in p–Pb collisions at $\sqrt{s_{\rm NN}}$ = 8.16 TeV [63], for the measurement performed at forward (backward) rapidity presented in blue (red) points in the figure. The vertical lines present statistical uncertainty, while the box is systematic. The dashed line represents the one-to-one correlation to guide the eye.

a finer multiplicity binning and a higher multiplicity reach (~ 6 times the average multiplicity) could be achieved. At both rapidity regions, and up to ~ 1.5 times the average multiplicity, the yields increase with increasing multiplicity, with a trend compatible with a linear approach ($y = x$), depicted with a dashed line in the figure. At higher multiplicities, the yields seem to deviate from the linear behavior, and exhibit a faster than linear trend for the yields extracted at backward rapidity, and slower than a linear trend for the yields extracted at forward rapidity. The underlying mechanism behind this difference in the be-

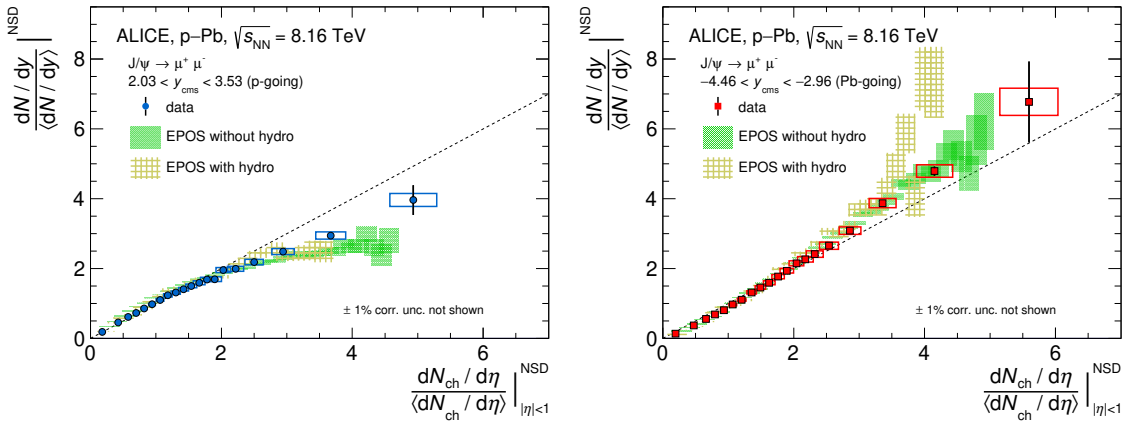

(a) Forward rapidity (b) Backward rapidity

Figure 4.4: Self-normalized J/ψ yields as a function of self-normalized charged-particle multiplicity, measured at midrapidity, in p–Pb collisions at $\sqrt{s_{NN}}$ = 8.16 TeV compared to the EPOS 3 event generator calculation [59, 89]. The measurement in a (b) presents the J/ψ yields extracted at forward (backward) rapidity.

havior at forward and backward rapidity remains unclear. These two measurements probe Pb-nucleus in a different Bjorken-x regime. The forward rapidity measurement is sensitive to the low Bjorken-x regime, $x_{Pb} \sim 10^{-5}$, whereas the backward rapidity is sensitive to the intermediate-to-large values, $x_{Pb} \sim 10^{-2}$. Fig.4.4 compares the multiplicity dependence of J/ψ self-normalized yields to EPOS 3 event generator calculation [59, 89]. EPOS 3 is based on a 3D + 1 viscous hydrodynamical evolution. The individual scatterings emerge as flux tubes (strings) generated in the Gribov-Regge multiple scattering formalism. An individual scattering is called a Pomeron, and is identified with a parton ladder. Each parton ladder consists of pQCD hard process with initial and final state parton emission. EPOS considers possible modifications of the initial conditions of the collision by means of a saturation scale. EPOS 3 without hydro calculations fairly describe the results at both forward and backward rapidity up to the highest probed multiplicity.

4.1.3 ψ(2S)-over-J/ψ results

In this section, we discuss the ψ(2S)-over-J/ψ self-normalized yields as a function of the self-normalized charged-particle multiplicity The measurement is performed by evaluating the self-normalized ratio of the ψ(2S) and J/ψ yields in the same multiplicity interval. The measurement of the multiplicity dependence of J/ψ performed by ALICE at the same energy [63], see Sec.4.1.2, was performed considering different multiplicity intervals than those

used for the ψ(2S) analysis. Hence, we had to re-evaluate the multiplicity dependence of the J/ψ yields with the multiplicity intervals of our ψ(2S) analysis, see Sec.3.4 for the details of the analysis. Fig.4.5 presents the results of this thesis, compared to those of Ref.[63]. We obtain a good agreement for the J/ψ yields, regardless of the different multiplicity intervals considered in both analyses.

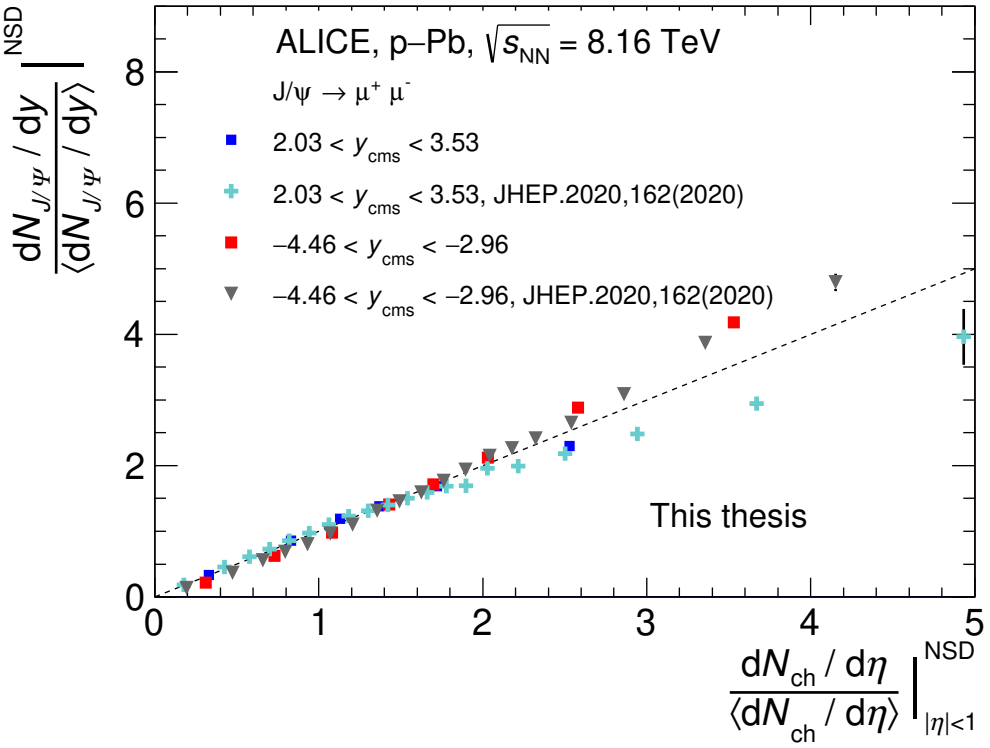

Figure 4.5: Comparison between the results for the J/ψ normalized yields obtained for this thesis multiplicity intervals and Ref.[63].

The double ratio (ψ(2S)-over-J/ψ) measurement allows one to disentangle any possible difference in the multiplicity dependence between the charmonium excited and ground states. The results are shown in Fig.4.6. The ψ(2S)-over-J/ψ is compatible with a flat distribution, within uncertainties, at both forward and backward rapidity in p–Pb collisions at $\sqrt{s_{NN}}$ = 8.16 TeV. In Fig.4.6, the multiplicity dependence of ψ(2S)-over-J/ψ is compared to the comover model calculations [41, 86]. The comover model suggests a stronger suppression for ψ(2S) with respect to the J/ψ, due to the weaker binding of the ψ(2S). The effect is stronger for high multiplicity events. A stronger suppression is expected at backward rapidity compared to forward rapidity due to the larger density of soft particles, which increases the probability of interaction with charmonia and, therefore, the dissociation probability. The

comover model calculation is compatible with our results within uncertainties.

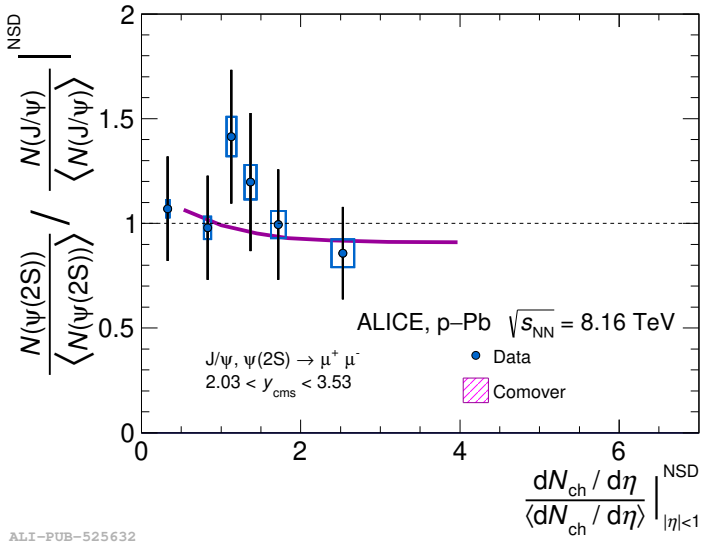

(a) Forward rapidity

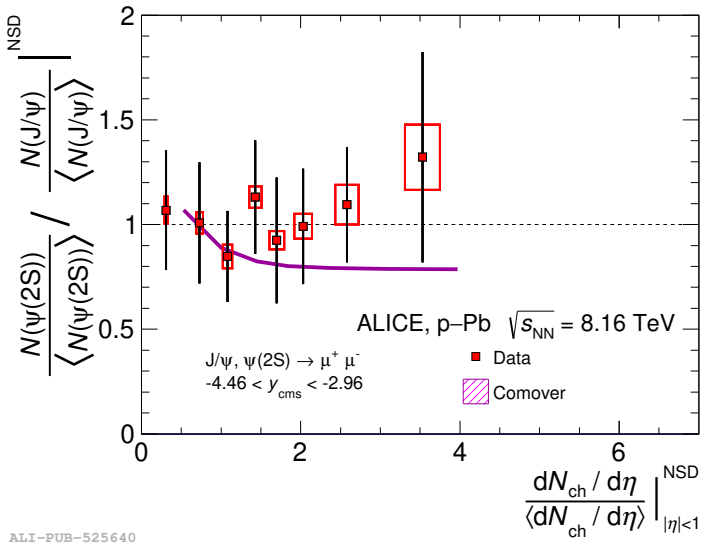

(b) Backward rapidity

Figure 4.6: The self-normalized ψ(2S)-over-J/ψ yields as a function of self-normalized charged-particle multiplicity from p–Pb collisions at $\sqrt{s_{NN}} = 8.16$ TeV, for the forward rapidity region in the top panel and backward rapidity region in the bottom panel [83]. The results are compared to the comover model calculations [41, 86].

4.2 Quarkonium multiplicity dependence in pp collisions

4.2.1 $\psi(2S)$ results

The multiplicity dependence of the $\psi(2S)$ self-normalized yields in pp collisions at $\sqrt{s}$ = 13 TeV is reported in Ref.[83]. $\psi(2S)$ mesons were reconstructed from their decay channel into dimuons in the rapidity interval $2.5 < y_{\rm cms} < 4.0$, while the charged-particle multiplicity was measured at midrapidity $|\eta_{\rm cms}| < 1$. As shown in Fig.4.7, the $\psi(2S)$ self-normalized

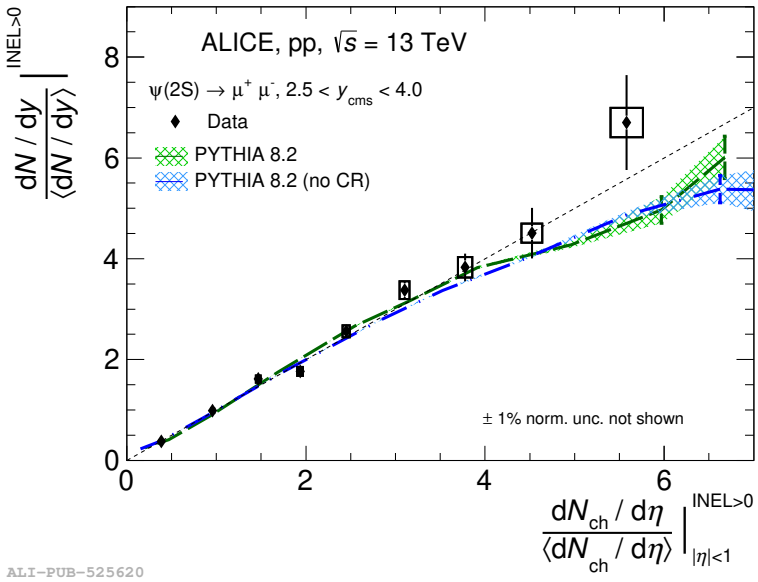

Figure 4.7: Self-normalized $\psi(2S)$ yields, measured at forward rapidity, as a function of the midrapidity charged-particle multiplicity, in pp collisions at $\sqrt{s}$ = 13 TeV [83]. The results are compared to PYTHIA 8.2 calculations with and without color reconnection [26].

yields increase with charged-particle multiplicity. The resulting trend is compatible, within uncertainties, with a linear increase depicted with a dashed line in the figure. The result is compared to PYTHIA 8.2 calculations [26], with and without color reconnection (CR). PYTHIA 8.2 event generator describes the charm quark production during the initial hard processes and with multiparton interactions (MPI). The number of charged particles produced is proportional to the number of events containing MPI. The color reconnection scenario represents the fusion of the final state partons. In Fig.4.7, PYTHIA 8.2 calculations, both with and without color reconnection, show similar behavior to data. The trend of the calculation is compatible with measurements over the full multiplicity range.

4.2.2 J/ψ results

The forward and midrapidity self-normalized J/ψ yields as a function of the charged-particle multiplicity in pp collisions are presented in Fig.4.8 [54, 60]. At forward rapidity ($2.5 < y_{\rm cms} < 4.0$), J/ψ particles are measured via their decay channel into dimuon. At midrapidity ($|y\,y_{\rm cms}| < 0.9$), J/ψ particles are measured via their decay channel into dielectron. On the central and right panels of Fig.4.8, we find the measurements performed in

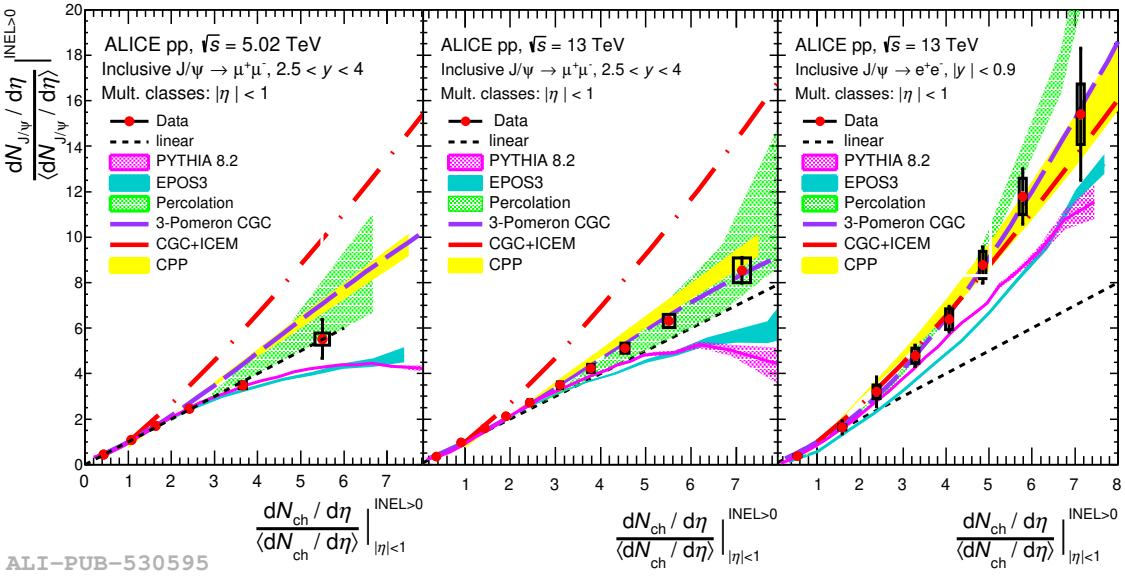

Figure 4.8: Self-normalized yield of J/ψ as a function of midrapidity self-normalized charged-particle multiplicity. The yields are measured in their decay channel into dimuon at forward rapidity in pp collisions at $\sqrt{s}$ = 5.02 and 13 TeV, respectively, in the left and the central panel. The result in the right panel shows the yields measured at midrapidity from pp collisions at $\sqrt{s}$ = 13 TeV [54, 60]. The measurements are compared to the theoretical calculations from PYTHIA 8.2 [26], EPOS3 [59], Percolation [57, 58], 3-Pomeron CGC [56], CGC+ICM [38], and CPP [55].

pp collisions at $\sqrt{s}$ =13 TeV. The forward J/ψ trend is compatible with a linear increase ($y = x$) with increasing multiplicity within uncertainties. At midrapidity, the increase is stronger than linear. On the left and central panels of Fig.4.8, we can compare the forward rapidity measurement at $\sqrt{s}$ = 5.02 TeV and 13 TeV. No energy dependence is observed for the J/ψ self-normalized yields. The measurements are compared to the 3-pomeron color glass condensate (3-pomeron CGC) [56], CGC with improved color evaporation model (CGC+ICEM) [38], percolation [57, 58], coherent particle production (CPP) [55], EPOS3 [59], and PYTHIA 8.2 [26] calculations. The percolation model, EPOS3, and PYTHIA 8.2 event generators have already been introduced in Sec.4.1.1, 4.1.2, and 4.2.1, respectively.

The CPP model treats pp, pA, and AA collisions with similar bases. The model assumes a linear dependence between the mean multiplicity of light and heavy particle production and the number of nucleon-nucleon collisions. In the CGC+ICEM model, the charmonia are produced via the color evaporation model. The model describes the hadronization by employing non-relativistic QCD. In this model, the production of the heavy flavor particles is sensitive to the configuration of the gluons in pp and pA collisions. The model uses a saturation scale to control the dynamics of these gluons. In the computation of the CGC, the probability of producing charmonia increases via a sizable contribution of the multi-pomeron mechanism, particularly the 3-pomeron. The measurements are compatible qualitatively with the theoretical computations from 3-pomeron CGC, percolation, and CPP models within uncertainties, while EPOS3 and PYTHIA 8.2 event generators underestimate the trends at high multiplicity.

4.2.3 ψ(2S)-over-J/ψ results

The forward $\psi(2S)$-over-J/ψ self-normalized yield ratio as a function of the midrapidity charged-particle multiplicity is presented in Fig.4.9. The double ratio measurement allows

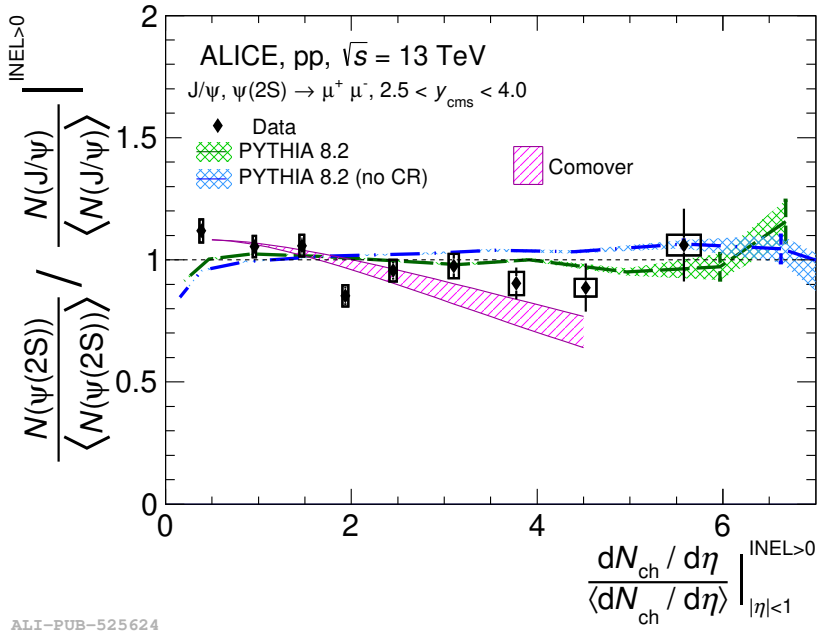

Figure 4.9: $\psi(2S)$-over-J/ψ self-normalized yield ratio, measured at forward rapidity, as a function of the midrapidity charged-particle multiplicity [83]. The result is compared to PYTHIA 8.2 and comover model calculations [26, 41].

one to disentangle any possible differences in the multiplicity dependence between the

charmonium excited and ground states. The resulting trend is compatible with a flat behavior within uncertainties. The result is compared to PYTHIA 8.2 event generator calculations which predict a similar behavior for both particles within uncertainties. PYTHIA 8.2 calculations with and without CR reproduce the results up to the highest probed multiplicity. The result is also compared to the comover model calculation [41]. The comover model predicts a stronger suppression for the ψ(2S) with respect to J/ψ, as the former has a larger size than the J/ψ. The comover model calculation describes the measurement, within uncertainties, in the model calculation domain. The precision of the measurement and of the model calculations does not allow us to conclude on whether final state effects might play a significant role in pp collisions at high multiplicity.

4.2.4 Comparison of charmonium results across system size

Figure 4.10 presents the comparison of J/ψ self-normalized yields as a function of charged-particle multiplicity in pp, p–Pb and Pb–Pb collisions at various center-of-mass energies (see caption for details) [90, 63, 91, 92]. It is important to mention that the average charged-particle multiplicity for pp collisions is ~ 6 [90], whereas the correspondent value for 0-90% Pb–Pb collisions is ~ 545 [93]. Despite this difference, the self-normalized yields exhibit a striking similar behavior in both colliding systems. The trend also presents similarities with the p–Pb results at backward rapidity (Pb-going). Note that the overall increase of multiple parton interactions (from pp to Pb–Pb) is expected to cancel in the self-normalized ratios, that are only sensitive to the relative evolution with charged-particle multiplicity in a given colliding system. Model calculations are required to interpret these similarities.
Analogously, in Fig. 4.11(a) are displayed the self-normalized yields of ψ(2S) in pp and p–Pb collisions as a function of charged-particle multiplicity. The results are compatible, within the uncertainties. As argued earlier in this chapter, the ψ(2S)-over-J/ψ ratio is evaluated to pin down possible differences between the multiplicity dependence of excited and ground states. The ratios, shown in Fig. 4.11(b), are compatible with unity for both colliding systems. A larger data sample would be needed to conclude on the possible differences among ground and excited states, and to clarify the role of initial and final state effects.

4.2.5 Bottomonium results

The self-normalized yields of Υ(1S), Υ(2S), and Υ(3S) are presented as a function of charged-particle multiplicity in Fig.4.12(a) [95]. The measurement is performed in pp collisions at $\sqrt{s}$ = 13 TeV, where the bottomonium yields are measured at forward rapidity, $2.5 < y_{\rm cms} < 4.0$,

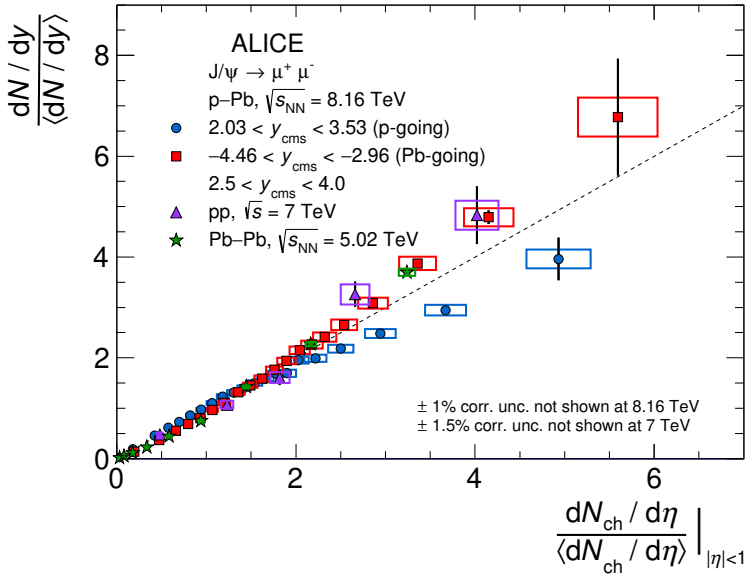

Figure 4.10: Normalized yield of inclusive J/ψ as a function of the normalized charged-particle pseudorapidity density, measured at midrapidity, in various collision systems. The pp results are normalized to INEL collisions [90], whereas p–Pb ones refer to the NSD event class [63]; all for $p_{\mathrm{T}} > 0$. The Pb–Pb data points include J/ψ with $0.3 < p_{\mathrm{T}} < 12$ GeV/c to reduce the low-p_{T} contribution from photoproduction, which is significant only in more peripheral collisions [91, 92, 94]. The vertical bars represent the statistical uncertainties, and the boxes are the systematic ones. The dashed line indicates the one-to-one correlation, to guide the eye.

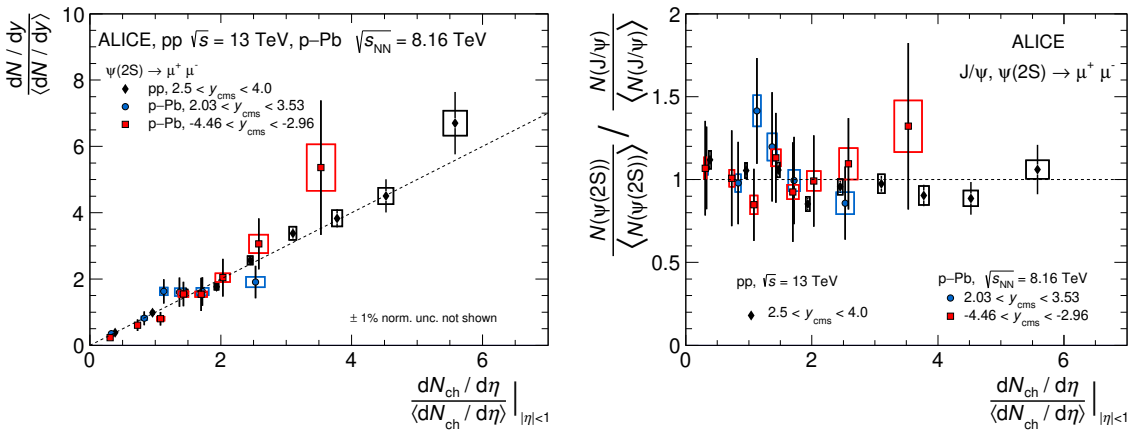

(a) $\psi(2S)$ self-normalized yields

(b) $\psi(2S)$-over-J/ψ

Figure 4.11: (a) The normalized $\psi(2S)$ yield as a function of the normalized charged-particle pseudorapidity density in pp collisions at $\sqrt{s}$ = 13 TeV and p–Pb collisions at $\sqrt{s_{NN}}$ = 8.16 TeV [83]. Quoted is the correlated event-class normalization uncertainty. (b) Ratio of normalized $\psi(2S)$-over-J/ψ yield as a function of the normalized charged-particle pseudorapidity density in pp collisions at $\sqrt{s}$ = 13 TeV and p–Pb collisions at $\sqrt{s_{NN}}$ = 8.16 TeV [83]. The pp results are normalized to the INEL>0 event class, whereas the p–Pb ones refer to the NSD one.

from their decay channel into a dimuon, and the charged-particle multiplicity is measured at midrapidity, $|y_{cms}| < 1$. The yields show an increase with charged-particle multiplicity. This behavior is compatible with a linear increase ($y = x$) depicted with a dashed line in the figure. The bottom panel of Fig.4.12(a) shows the ratio of the bottomonium yields to the charged-particle multiplicity, i.e., the ratio of the y-axis to the x-axis. The nearly linear trends of the Υ yields in the top panel of Fig.4.12(a) result in a flat distribution of the ratios in the bottom panel, suggesting a similar behavior of the Υ states with multiplicity. The self-normalized $\Upsilon(2S)$-over-$\Upsilon(1S)$ ratio as a function of charged-particle multiplicity is displayed in Fig.4.12(b). The $\Upsilon(2S)$-over-$\Upsilon(1S)$ ratio is compatible with unity, within uncertainties, in the probed multiplicity region. The measurement is compared to several theoretical calculations. No relevant difference is observed between PYTHIA 8.2 event generator calculations with and without color reconnection, which describe the observed behavior of the ratio. The 3-pomeron CGC and CPP calculations are compatible with the flat distribution of the self-normalized $\Upsilon(2S)$-over-$\Upsilon(1S)$ ratio within uncertainties. The measurement is also compared to the comover model calculation, which predicts a stronger suppression, 20% to 40%, of the $\Upsilon(2S)$ compared to the $\Upsilon(1S)$. The self-normalized $\Upsilon(3S)$-over-$\Upsilon(1S)$ ratio is also reported in Ref.[95] as a function of charged particle multiplicity in pp collisions

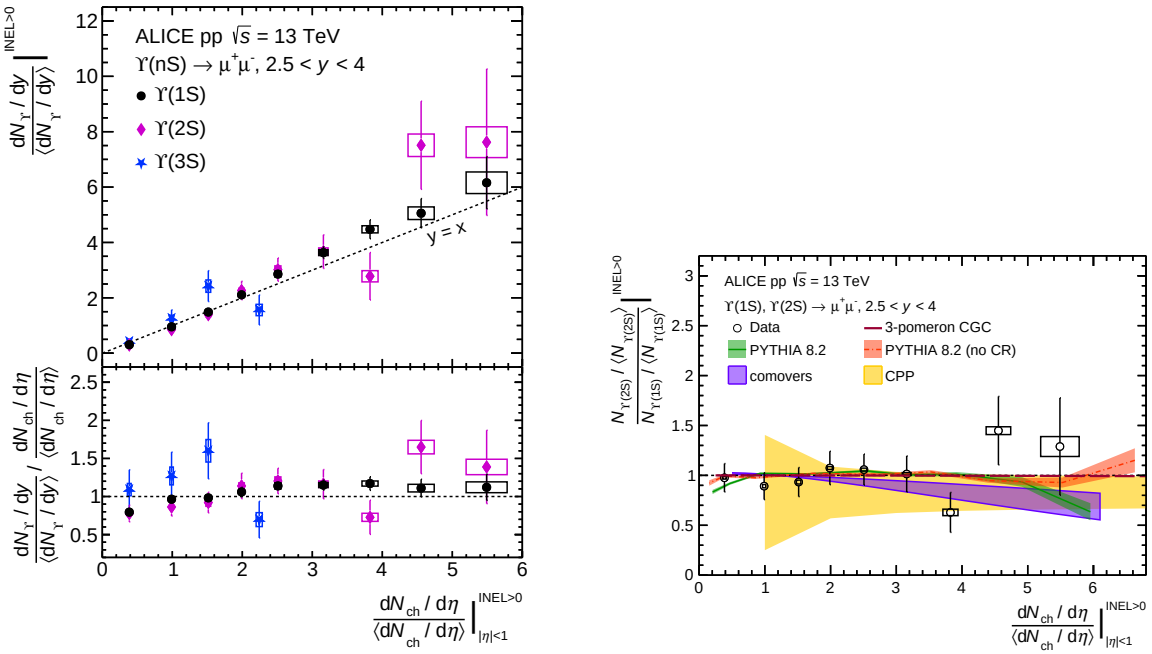

(a) ϒ self-normalized yields

(b) ϒ(2S)-over-ϒ(1S)

Figure 4.12: The multiplicity dependence of (a) self-normalized bottomonium yields, (b)ϒ(2S)-over-ϒ(1S) [95]. The vertical error bars represent the statistical uncertainty on the yields, while the height and the width of the box represent the systematic uncertainty on the yields and the charged-particle multiplicity, respectively. The measurement in (b) is compared to the 3-pomeron CGC [56], PYTHIA 8.2 [26], and CPP [55] calculations.

at $\sqrt{s}$ = 13 TeV. The multiplicity dependence of the Υ(3S)-over-Υ(1S) ratio shows a trend compatible with a flat distribution. However, a firm conclusion on the behavior of the ratio requires further investigation using a larger data sample.
CMS collaboration also reported some measurements of the bottomonium states. In particular, the ratio of the excited-over-ground state yields, Υ(nS)/Υ(1S), as a function of the number of tracks (N_{track}), where both quantities are measured at midrapidity ($|y_{\text{cms}}| < 1.93$) in pp collisions at $\sqrt{s}$ = 2.76 TeV [61] and 7 TeV [62] (see Fig.4.13). A clear decreasing trend is visible for both excited-over-ground state ratios, from low to high N_{track} intervals. The excited-over-ground bottomonium ratio in pp collisions is also compatible with the measurement performed in p–Pb collisions at $\sqrt{s_{\text{NN}}}$ = 5.02 TeV, which is depicted with blue markers in Fig.4.13 [61]. Two hypotheses are suggested to explain the difference in the behavior between the Υ(2S)-over-Υ(1S) and Υ(3S)-over-Υ(1S) in Ref.[61]. First, the Υ(1S) might be systematically produced with much more soft particles than the excited states, creating an artificial dependence when studying the production at small multiplicities. Second, the interaction with the final state comoving particles might result in a stronger suppression for the excited bottomonium states relative to the ground state, due to their weaker binding. In both cases, the ratio is expected to decrease as a function of multiplicity in pp and p–Pb collisions [61].
The measurement from CMS collaboration displays a non-normalized measurement contrary to the measurements from ALICE. In order to compare the two results, the self-normalized Υ(2S)-over-Υ(1S) as a function of $N_{\text{tracks}}/ < N_{\text{tracks}} >$ are evaluated for the CMS data in Ref.[96], and presented in Fig.4.14. The results show a ~ 40% decrease of the yields with increasing $N_{\text{tracks}}/ < N_{\text{tracks}} >$, which might deviate from the flat distribution observed in the measurement performed by ALICE. Note that the CMS measurement is performed at $\sqrt{s}$ = 2.76 TeV with no rapidity gap between the yields and the multiplicity. On the other hand, ALICE results are for $\sqrt{s}$ = 13 TeV and with a rapidity gap between the two measured quantities. The bottomonium results from ALICE and CMS are compatible within the current precision.

4.3 Open heavy-flavor results

Fig.4.15(a) presents the self-normalized average yields of prompt D^0, D^+ and D^* as a function of charged-particle multiplicity, measured at $|\eta| <1$, in pp collisions at $\sqrt{s}$ = 13 TeV. On the left panel, the D-meson yields are displayed in different p_{T} intervals. The measurement shows a yield increase as a function of charged-particle multiplicity in all the

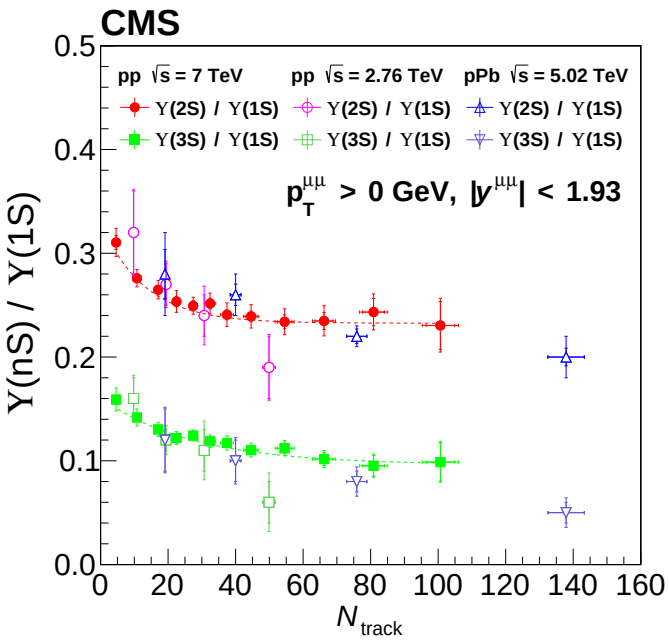

Figure 4.13: The ratios of the $\Upsilon(2S)$-over-$\Upsilon(1S)$ and $\Upsilon(3S)$-over-$\Upsilon(1S)$, with $p_T > 0$ GeV, as a function of the number of tracks (N_{track}). The lines are fits to the data with an exponential function. The vertical error bars represent the combined statistical and systematic uncertainties on the bottomonia ratio, while the horizontal error bars represent the uncertainty on N_{track} [61, 62].

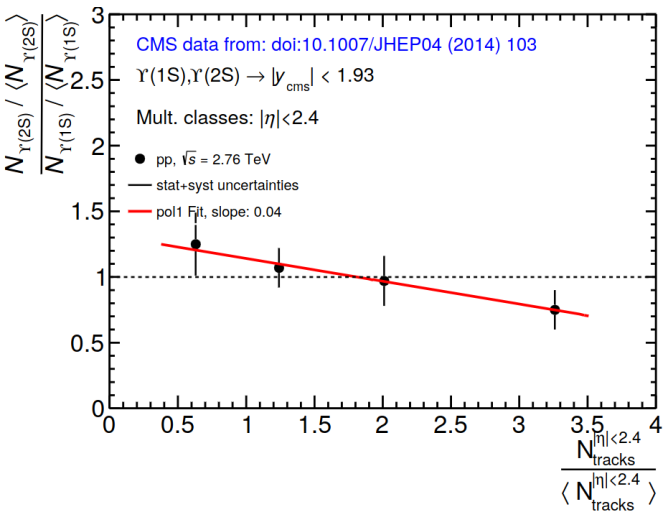

Figure 4.14: The normalized $\Upsilon(2S)$-over-$\Upsilon(1S)$ yields as a function of $N_{\text{tracks}} / < N_{\text{tracks}} >$ measured at midrapidity in pp collisions at $\sqrt{s} = 2.76$ TeV. The figure is taken from Ref. [96].

p_{T} intervals. This increase becomes stronger with increasing p_{T}. On the right panel, the multiplicity dependence of the self-normalized D-meson, J/ψ, and heavy-flavor decay electrons are represented together. The comparison is made for the prompt D-meson yields with $2.0 < p_{\mathrm{T}} < 4.0$ GeV/c, heavy-flavor decay electrons with $3.0 < p_{\mathrm{T}} < 6.0$ GeV/c and J/ψ with $p_{\mathrm{T}} < 4$ GeV/c to ensure that particles have similar kinematics. Prompt D mesons are originated from charm-quark decays, inclusive J/ψ are also predominantly from charm-quark decays (contribution from b-decays is of the order of 10%), while heavy-flavour decay electrons stem from a mixture of charm and beauty quark decays. Fig.4.15(b) shows that J/ψ, prompt D-mesons, and heavy-flavor decay electron yields exhibit similar behavior as a function of charged-particle multiplicity. This suggests that hadronization does not play a significant role on the evolution with charged-particle multiplicity (similar results are observed for prompt D and inclusive J/ψ), and that there are no striking differences on charm and beauty quark decays evolution with charged-particle multiplicity (similar results for prompt D and heavy–flavor decay electrons).

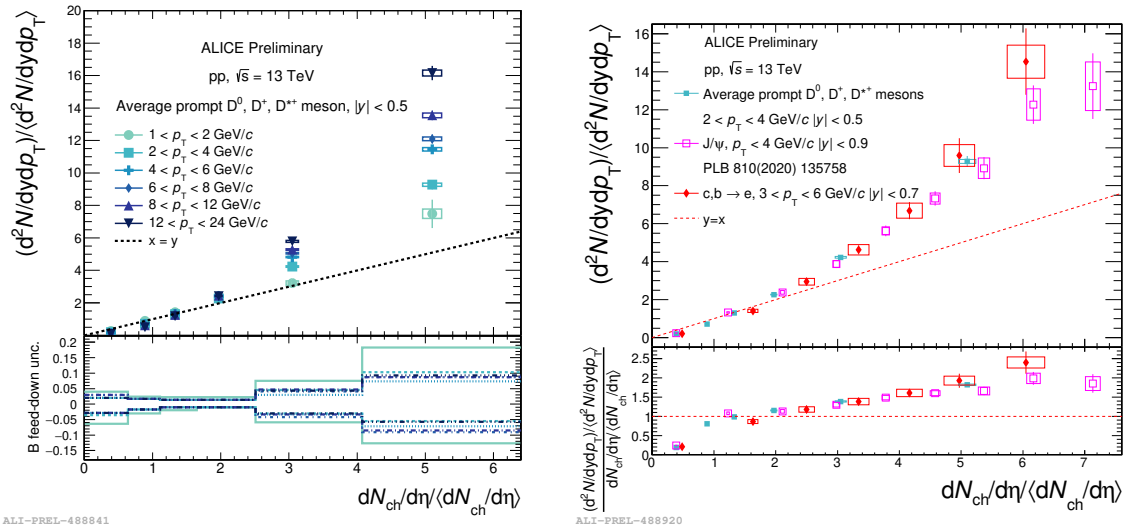

(a) (b)

Figure 4.15: Self-normalized D^0, D^+ and D^* yields as a function of charged-particle multiplicity in pp collisions at $\sqrt{s} = 13$ TeV at midrapidity. (a) The yields are shown in different intervals of p_{T}, (b) The multiplicity dependence of D^0, D^+ and D^* self-normalized yields, for the p_{T} interval $2 < p_{\mathrm{T}} < 4$ GeV/c, compared to the self-normalized J/ψ yields with $p_{\mathrm{T}} < 4$ GeV/c, and compared to the heavy flavor decay electrons yields with $3 < p_{\mathrm{T}} < 6$ GeV/c.

Part III

ALICE Run 3

5

ALICE Run 3 and 4 upgrades

This chapter outlines the main ALICE Run 3 and 4 upgrades relevant to this thesis. These upgrades were carried out during the Long Shutdown 2 (LS2) from 2019 to 2022. In Sec.5.1, we discuss the main motivations for the upgrades. In Sec.5.2 and 5.3, we present the central and forward detector upgrades, respectively. Finally, we discuss the new ALICE online–offline computing system.

5.1 Motivations for Run 3 and 4 upgrades

As explained in the upgrade Letter Of Intent [97], the ALICE upgrades after the LS2 aim at exploiting the full potential of the LHC, focusing on heavy-ion collisions for the higher precision study of the quark-gluon plasma. In this regard, the Run 3 and 4 ALICE upgrade is based on reading out all Pb–Pb (pp) collisions at an interaction rate of 50 (400) kHz. Therefore, major upgrades have taken place during LS2 for the detectors at the central barrel and the forward arm, in addition to the upgrade of the online–offline system. Fig.5.1 presents a schematic of the ALICE detector after the LS2. A last note about the ALICE upgrade program, two new detectors should be installed or upgraded during LS3 (2026-2028): the Forward Calorimeter (FoCal) [98] and the upgraded ITS (ITS3) [99]. They will not be discussed in the following, as they can be considered as *Run 4 only* upgrades.

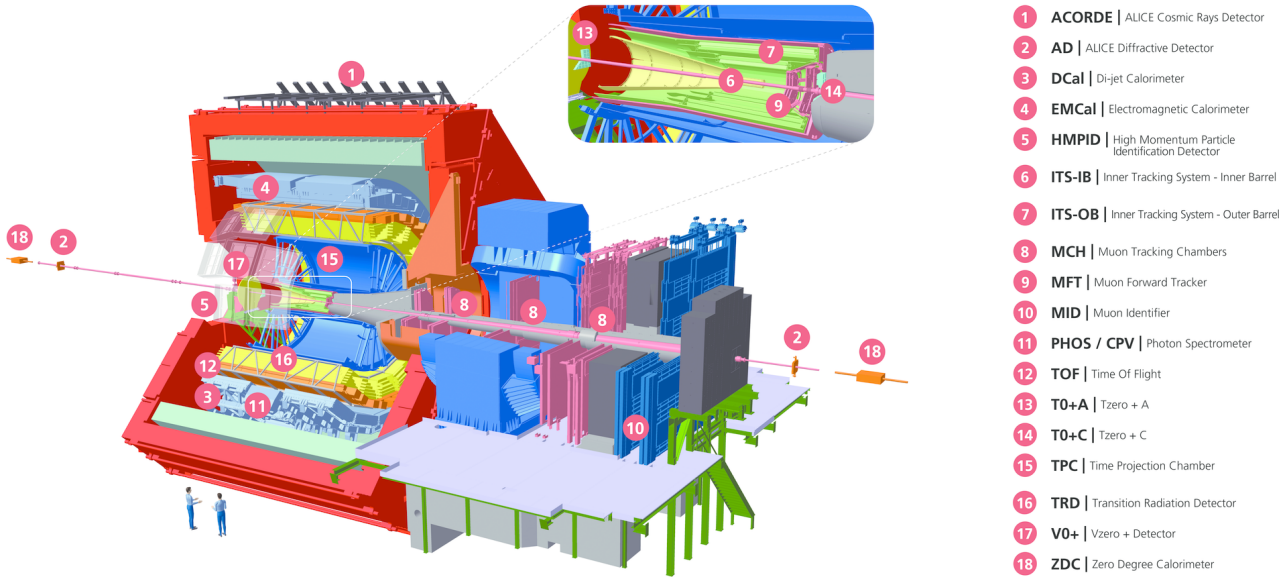

Figure 5.1: ALICE detector schematic after the LS2. Superimposed a zoom–in of the region close to the interaction point.

5.2 Central barrel detectors upgrades

5.2.1 The Inner Tracking System (ITS)

The description of the ITS detector during Run 2 is discussed in Sec.2.2.1. One of the main limitations of the Run 2 ITS detector is the readout capabilities. As mentioned in Ref.[97], the ITS readout electronics can reach a maximum of about 1 kHz regardless of its occupancy. This implies that Run 2 ITS will not be adequate for the readout capabilities for Run 3 physics objectives. The layout of the upgraded ITS detector is shown in Fig.5.2. The upgraded ITS detector consists of seven cylindrical layers of silicon detectors compared to six layers during Run 2. As the upgrade of ALICE included the reduction of the beam pipe radius, the innermost layer of the ITS is located at a closer distance to the interaction point (2.2 cm compared to 3.4 cm during Run 2). In addition to moving the detector closer to the interaction point, the ITS upgrade will involve reducing the material budget and pixel size. These enhancements are expected to significantly improve the tracking efficiency and impact parameter resolution of the detector. The ITS silicon pixels are based on Monolithic Active Pixel Sensor (MAPS), which reduces the silicon material budget per layer seven times compared to the ITS Run 2. Significant improvements in the spatial resolution, especially at low-p_{T} [100, 101], are expected.

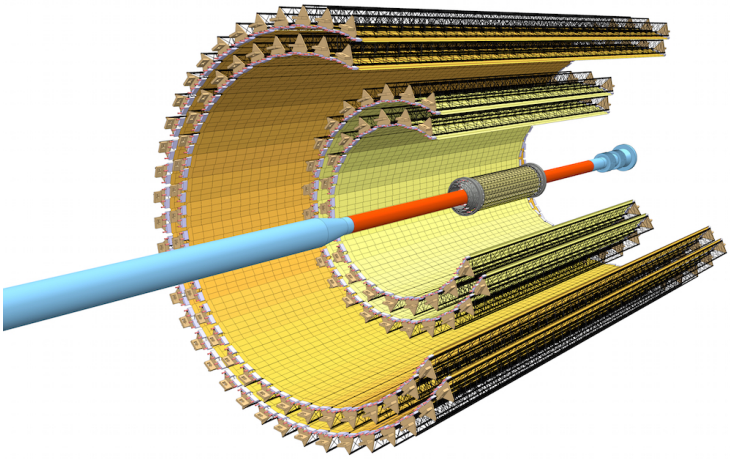

Figure 5.2: The layout of the ITS detector during Run 3.

5.2.2 The Time Projection Chamber (TPC)

The Time Projection Chamber (TPC) is the main charged particle tracker and particle identifier detector of ALICE. During Run 2, the TPC consisted of a cylindrical drift field cage and two readout planes on the end caps (see Sec.2.2.1 for the details). The design of the readout was based on the Multi Wire Proportional Chambers (MWPC) technology with cathode pad readout. The readout chambers use a scheme of wire grids consisting of a plane of anode wires, cathode wires, and a gating grid. As the event rate is increased during Run 3, and with the requirements of a continuous readout. The TPC MWPCs read-out chambers have been replaced with Gas Electron Multipliers (GEM), allowing the TPC to be continuously read out. The front end of the TPC has also been upgraded to cope with the increased data-taking rate [102].

5.2.3 The Fast Interaction Trigger

The Fast Interaction Trigger (FIT) detector is the Run 3 replacement of the V0, T0, and FMD detectors. The FIT consists of three sub-detectors: the FT-zero (FT0), FV-zero (FV0), and the Forward Diffractive Detector (FDD). FT0, FV0, and the FDD serve as the leading fast trigger for ALICE during Run 3 and 4. In addition, FIT provides information for measuring the event multiplicity, initial indication for vertex location, beam-gas rejection, collision time, and event-plane position. All the aforementioned requirements are expected to be fulfilled with the FIT with high precision compared to the V0, T0, and FMD detectors during Run 2 [102].

5.3 The new Muon Spectrometer

5.3.1 The Muon Tracking Chambers (MCH)

MCH detector is based on multi-wire proportional chambers with cathode pads read-out. The system consists of 5 stations, each composed of two chambers. The first two stations are based on a quadrant structure, while the last three are based on a slat structure. Significant modifications have been implemented in the electronics of the MCH to accommodate the continuous readout scheme for Run 3. However, the overall detector implementation and the physical location and layout of its electronics have remained unchanged. The diagram shown in Fig.5.3 depicts the muon tracking system's electronics. The signal originating from the Front-End Electronics (FEE) is transmitted to the GigaBite Transceiver (GBT) readout card, which multiplexes 40 FEE signal outputs into a single gigabit serial stream. This stream is then directed to the Common Readout Unit (CRU). The CRUs are interconnected with the online computing system (O2) through the DDL3 interfaces, enabling the transmission of detector data to the O2 and receiving DCS (Detector Control System) information from it [102].

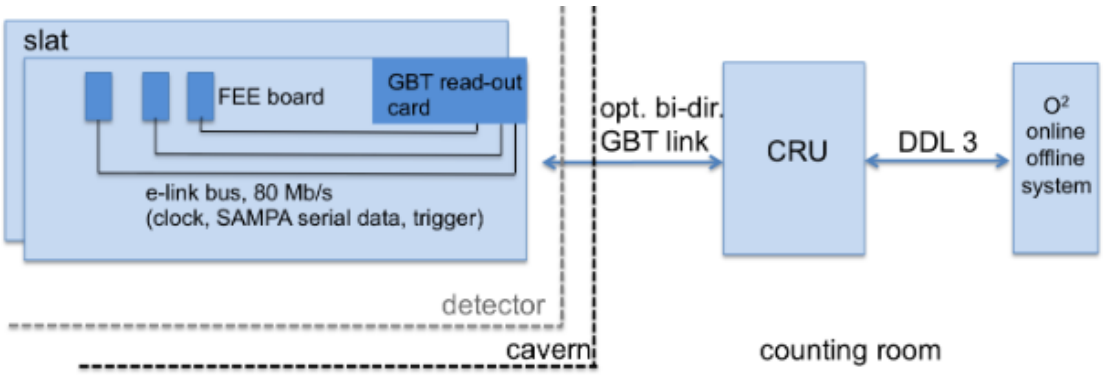

Figure 5.3: Schematic of the ALICE muon tracking chambers electronics during Run 3 [102].

5.3.2 The Muon Identifier (MID)

The MID detector relies on Resistive Plate Chamber (RPC), the same detector as in Run 2. In the continuous readout scheme, the task to provide p_{T}-dependent muon-triggered signals was replaced by the need to readout all RPCs at much higher rate. Thus, the readout architecture was upgraded similarly to the MCH one. The front-end readout electronics situated on the RPC detectors was also upgraded to mitigate the aging process of the RPCs

and increase the readout rate capabilities. The RPCs now operate in a genuine avalanche mode which leads to a reduced charge generated within the gas, thereby limiting the aging effects. The counterpart is the need to amplify the analog signals from the RPCs and a new front-end electronics circuit was designed for this purpose [102].

5.3.3 The Muon Forward Tracker (MFT)

The MFT is an all-silicon detector added to the muon spectrometer in the region between the ITS and the front absorber. The presence of the MFT in this region during Run 3 will allow to reduce the uncertainty in the matching between the muon tracks and the primary vertex. The MFT pixel detector is based on CMOS monolithic pixel sensor technology, the same technology employed by the upgraded ITS detector[103]. In addition, the MFT will allow distinguishing between the muon tracks from the primary vertex and those originating from the decay of B-hadrons. The MFT consists of two half cones, each consisting of five silicon discs, placed along the beam axis at a distance of z = -460, -493, -531, -687, -768 mm from the interaction point, and covers the pseudorapidity range of $2.5 < \eta_{\mathrm{lab}} < 3.6$.

5.4 Online-Offline computing system

The general workflow of the new ALICE Online-Offline (O2) computing system is presented in Fig.5.4. It includes data processing starting from the raw data to the Analysis Object Data (AO2D), which are used for the physics analysis. The upgraded ALICE computing system supports both continuous and triggered raw data processing.
First, the collected data are transferred from the detector readouts into the common read-out units using detector data links or gigabit transceivers. At this point, data are divided into Sub-Time Frames (STF) corresponding to the first level processing granularity and covering a period of about 11.4 ms (128 LHC orbits in 2022). In the second step, all the STFs of a given period converge to an event processing node, where the STFs are merged into complete Time Frames (TF). At this step, further calibration and data compression are performed. Then, the compressed TF is stored in a disk buffer for temporary storage. The final processing step is an asynchronous operation where the data are stored on the grid, and reconstruction and calibration are performed. Finally, the analysis is performed using the AODs within the O2 framework.

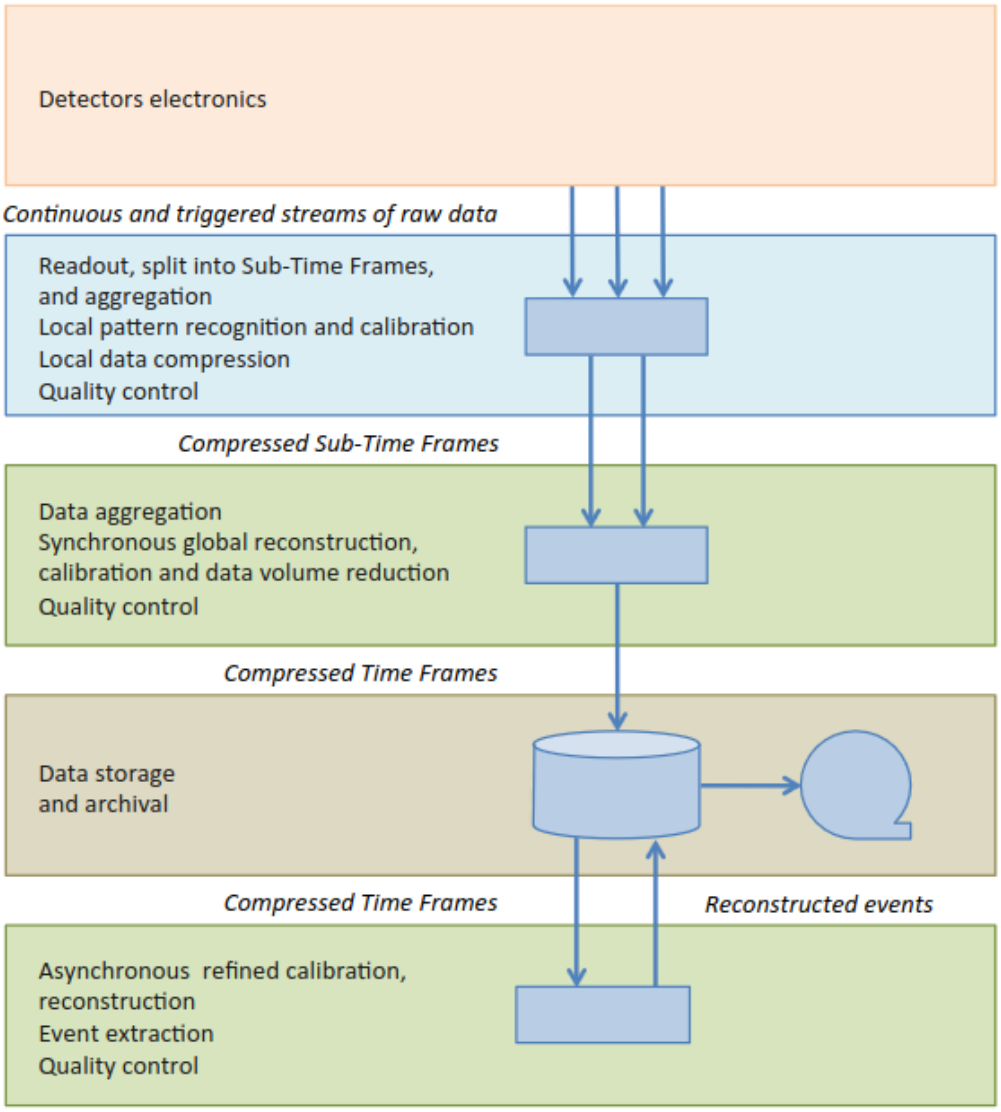

Figure 5.4: The flow chart of O2 computing system [104].

6

Systematic uncertainty of tracking efficiency of the Muon Tracking Chambers

In this chapter, we present the methodology used to compute the systematic uncertainty of the tracking efficiency of the muon tracking chambers. The results discussed in this chapter are obtained using Run 3 data from pp collisions at $\sqrt{s} = 13.6$ TeV. In Sec.6.1, we introduce the track reconstruction algorithm used in Run 3, and highlight the main differences with respect to the algorithm used in Run 2. In Sec.6.2, we present the equations used to estimate the tracking efficiency of the muon chambers. In Sec.6.3, we show the main results obtained for the muon tracking efficiency, both per muon tracking (MCH) chamber, and per station. Results are presented in intervals of p_{T}, η, or ϕ, as well as an integrated quantity. Finally, in Sec.6.4, we conclude with the comparison between the tracking efficiency computed from simulations and from data, in order to assess the systematic uncertainty on the tracking efficiency.

6.1 Muon track reconstruction

6.1.1 Muon track reconstruction: Run 2 algorithm

The reconstruction process starts in stations 4 and 5, where the particle multiplicity is lower compared to the other stations. The steps discussed in this section are explained in Ref.[105].

1. The reconstruction process starts in station 5 of the MCH by combining the information of the clusters from both chambers and by connecting them to build track segments. These segments are then extrapolated to a primary vertex, reconstructed by the SPD detector, through the magnetic field. For each reconstructed track segment, the local position, the direction, the impact parameter to the primary vertex, and their associated uncertainties are computed.

2. The track candidates that are out of the spectrometer acceptance and those which does not pass the initial momentum cut are rejected.

3. Steps 1 and 2 are repeated with the clusters in station 4.

4. The track candidates of station 4 (5) are extrapolated to station 5 (4). The algorithm looks for at least one compatible cluster in the other station to validate the candidate. If several compatible clusters are found in the same chamber, the track is duplicated to consider all the possibilities.

5. The tracks sharing the same clusters are removed, also those with an impact parameter and/or momentum out of given limits.

6. The remaining candidates are propagated to stations 3, 2, and 1, sequentially. The algorithm searches for at least one compatible cluster in each station. The track parameters are recalculated at each step, and only candidates that pass the impact parameter and momentum cuts are kept. In addition, when several compatible clusters are found in the same chamber, the track is duplicated to consider all the possibilities.

7. The candidates that share one or more clusters in stations 1, 2, or 3 are removed. The candidates with the largest number of clusters are kept. In case of a similar number of clusters, the track with a lower χ^2, i.e., better quality, is kept. By this step, the reconstructed tracks are called MCH standalone tracks.

8. The MCH tracks are matched with a track segment reconstructed from the same collision in the Muon Trigger Chambers to identify the muon tracks. The reconstructed tracks after this step are called MCH-MTR tracks.

9. Finally, the reconstructed tracks are extrapolated to the primary vertex. The track parameters are recalculated and corrected for the energy loss and multiple scattering in the front absorber.

6.1.2 Muon track reconstruction: Run 3 algorithm

As mentioned in Sec.5.3.2, the Muon Identifier (MID) is used to identify the muon tracks. Thanks to its excellent timing, the MID is able to separate tracks that belong to adjacent bunch crossings. Steps 1-7 are the same in Run 2 and Run 3.

8. The MCH tracks are matched to the track segments reconstructed in the MID detector. The MID track segment must belong to the same time period as the MCH track within some uncertainty related to the MCH tracks cluster time dispersion (around ±4 bunch crossings). The MCH-MID track is extrapolated to the primary vertex reconstructed by the ITS detector. The tracks that are out of the spectrometer acceptance or do not pass the momentum cuts are rejected. At this step in Run 3, the reconstructed track is called a muon standalone track.

9. The muon tracks are matched to the track segments reconstructed in the Muon Forward Tracker, i.e., MFT standalone tracks. Only the tracks that pass the impact parameter and the momentum cuts, and those within the MFT acceptance are kept. In cases where no MFT track can be matched, the track is labeled as an MCH-MID track, and the track parameters are updated.

10. Finally, the remaining tracks are extrapolated to the primary vertex reconstructed by the ITS detector. The final tracks are called global muon tracks.

11. For all track types, the track parameters are recalculated and corrected for the energy loss and multiple scattering in the front absorber.

A scheme of the different types of tracks that can be reconstructed in the upgraded Muon spectrometer (MFT+MCH+MID) is shown in Fig.6.1. They are defined as follows:

- Global muon track is a matched track in the MFT, MCH, and MID detectors.
- Global forward track is a matched track in the MFT and MCH detectors.
- Muon standalone track is a matched track in the MCH and MID detectors.
- MCH standalone track is a track in the MCH only.
- MFT standalone track is a track in the MFT only.

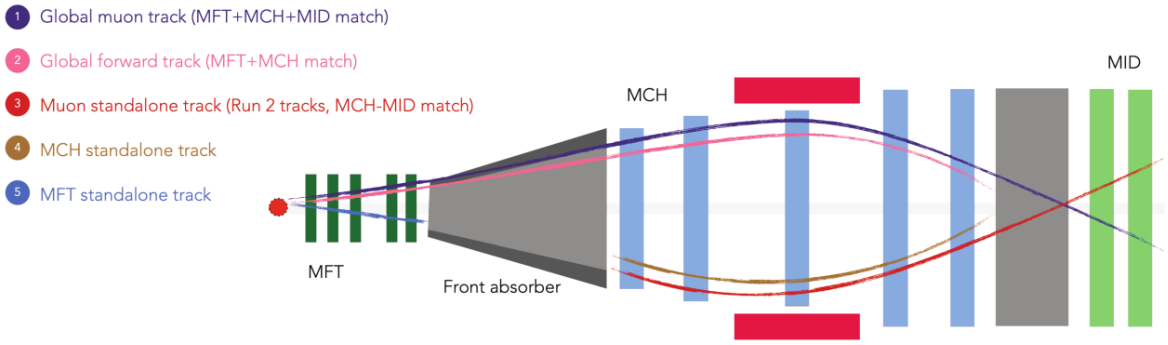

Figure 6.1: Scheme of the track types reconstructed in the muon spectrometer in Run 3. The sketch is taken from Ref.[106].

6.2 Tracking efficiency estimation from reconstructed tracks

We present here a method to evaluate the tracking efficiency of the muon chambers based on the reconstructed MCH standalone tracks. This method is exploiting the redundancy of the chambers, considering that the efficiency of one chamber is independent of that of the other chambers. This method can be applied on both data and simulations, and the comparison of results provides an indicator on how well the simulation reproduces the data. The difference between the tracking efficiency computed from data and from simulation can then be used to assess the systematic uncertainty on the tracking efficiency. However, since this method is based on reconstructed MCH standalone tracks, there is an intrinsic bias due to the tracking reconstruction algorithm, which requires at least three clusters in stations 4 and 5 and at least one cluster per station in stations 1, 2, and 3 as explained in the previous section. Thus this method cannot be used to compute the MCH tracking efficiency needed for corrections (which is extracted from dedicated MC simulations as described in 3.5.2).

The total number of tracks (N_{Tot}) crossing a station can be expressed as:

$$N_{Tot} = N_{i-j} + N_{i-0} + N_{0-j} + N_{0-0}, \tag{6.1}$$

where N_{i-j} is the number of tracks having a cluster in both chambers of the station, N_{i-0} (N_{0-j}) is the number of tracks having only one cluster in the first (second) chamber of the station and N_{0-0} is the number of tracks having no cluster at all. In this last case, the track is simply not reconstructed as it does not fulfill the conditions of the tracking algorithm. An illustration of the four cases is given in Fig.6.2 for station 1.

Considering that the efficiency of chamber i (ϵ_i) is independent from the efficiency of

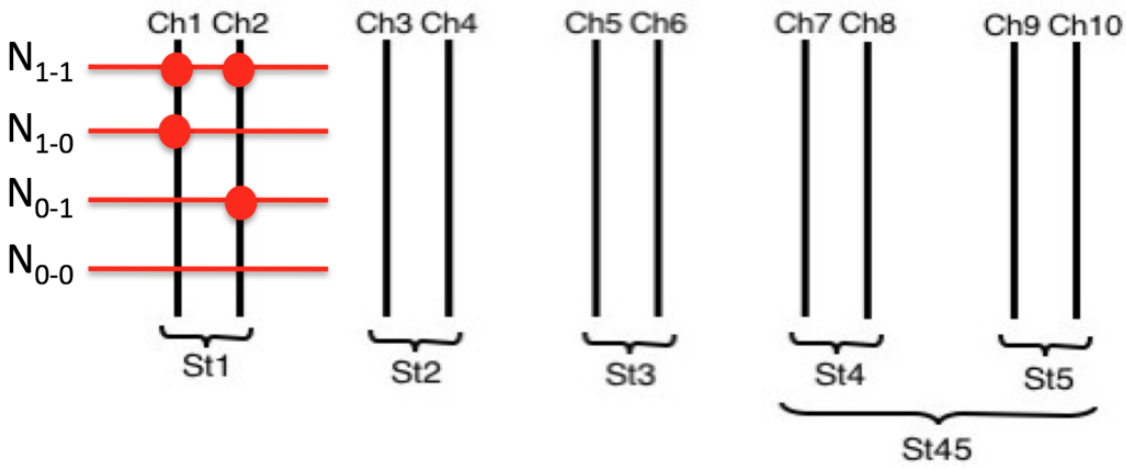

Figure 6.2: Conceptual drawing showing the possible responses of the MCH chambers to a track. The sketch is taken from Ref.[105].

chamber j (ϵ_j), one can write the number of tracks with a cluster in chamber i and j as:

$$N_{i-j} = \epsilon_i \times \epsilon_j \times N_{Tot}. \tag{6.2}$$

In the same way, the number of tracks with a cluster in the chamber i or j can be written as:

$$N_{i-0} = \epsilon_i \times (1-\epsilon_j) \times N_{Tot}, \tag{6.3}$$

$$N_{0-j} = (1-\epsilon_i) \times \epsilon_j \times N_{Tot}. \tag{6.4}$$

Using Eq.6.3 and Eq.6.4, the efficiency of the chambers i and j can be expressed as:

$$\epsilon_i = \frac{N_{i-j}}{N_{i-j} + N_{0-j}}, \tag{6.5}$$

$$\epsilon_j = \frac{N_{i-j}}{N_{i-j} + N_{i-0}}. \tag{6.6}$$

The efficiency of the first three stations can be written as a function of their chambers efficiency:

$$\epsilon_{St(1)(2)(3)} = 1 - (1-\epsilon_i) \times (1-\epsilon_j), \tag{6.7}$$

where (i, j) denote the chambers in the first, the second, or the third station, and can take the values (1,2), (3,4), or (5,6), respectively. The efficiency of stations 4 and 5 is evaluated as

a whole due to the tracking algorithm requirements, and is given by:

$$\epsilon_{St(45)} = \prod_{i=7}^{i=10} \epsilon_i + \sum_{i=7}^{i=10} \left((1-\epsilon_i) \prod_{j=7, j\neq i}^{j=10} \epsilon_j \right). \tag{6.8}$$

Then the muon chamber tracking efficiency is given by the product of the station's efficiency:

$$\epsilon_{tracking} = \epsilon_{St(1)} \times \epsilon_{St(2)} \times \epsilon_{St(3)} \times \epsilon_{St(45)}. \tag{6.9}$$

6.3 Tracking efficiency studies in pp collisions at $\sqrt{s} = 13.6$ TeV

We apply the method explained in the previous section to estimate the MCH tracking efficiency from pp collisions at $\sqrt{s}$ = 13.6 TeV. Only a very small sample of the collected data has been analyzed, in particular run number 523306, from the LHC22m period. The run 523306 corresponds to data taken on 14/08/2022, starting at 00:09:56 and up to 00:24:24. The pp interaction rate was about 500 kHz, with low pile-up (< 2%).

6.3.1 Integrated MCH tracking efficiency

The tracking efficiency integrated over p_{T}, η, and ϕ is presented in Fig.6.3 as a function of the chamber ID. The tracking efficiency is higher than 90% for all of the MCH tracking chambers, apart from chamber 3, which shows a value of 83%. We expect a chamber efficiency above 95% so the chambers with a value below that threshold, i.e. chambers 3, 5 and 8, will be investigated further in the following.
The tracking efficiency of the MCH stations is evaluated using Eq.6.7 and Eq.6.8, and is shown in Fig.6.4. The computed tracking efficiency for each station is higher than 99%, thanks to the chambers redundancy. In the same figure, the tracking efficiency for the full MCH detector, computed with Eq.6.9, is shown and reaches a value of 98.5%.

6.3.2 Tracking efficiency as a function of p_{T}, η, and ϕ

Here we present the efficiency of the MCH chambers as a function of the track kinematic variables p_{T}, η, and ϕ. Figure 6.5 presents the MCH chambers efficiency for six intervals of p_{T}. The p_{T}-differential tracking efficiency is above 95% for all the chambers except for chambers 3, 5, and 8; chambers in which we have already seen a lower tracking efficiency. The tracking efficiency per station and for the full MCH detector is presented in Fig.6.6 as

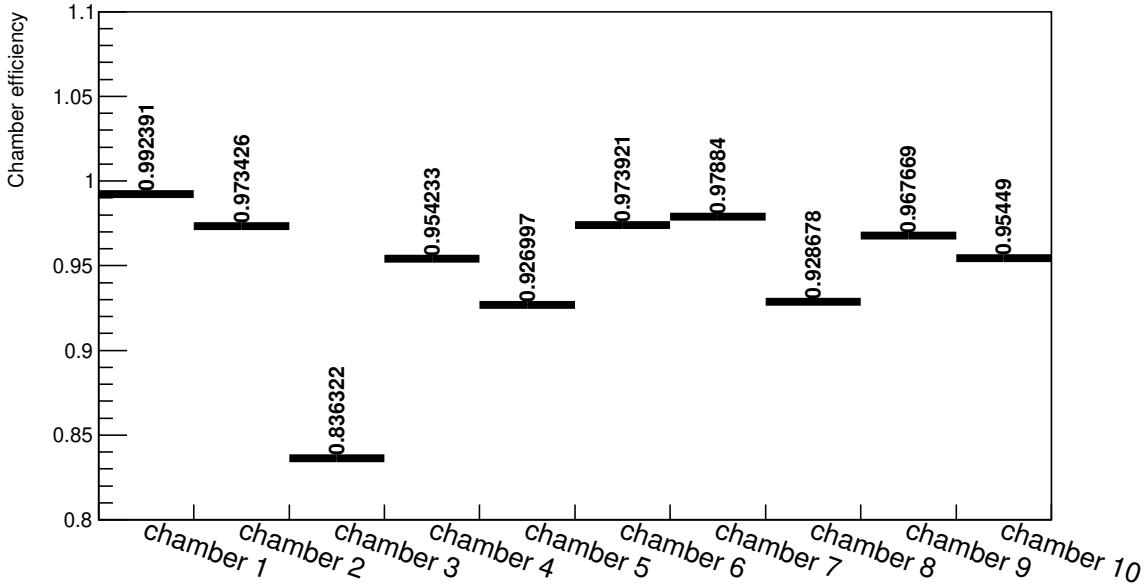

Figure 6.3: The tracking efficiency of the MCH chambers vs. chamber ID extracted from a sample of pp collisions at $\sqrt{s} = 13.6$ TeV.

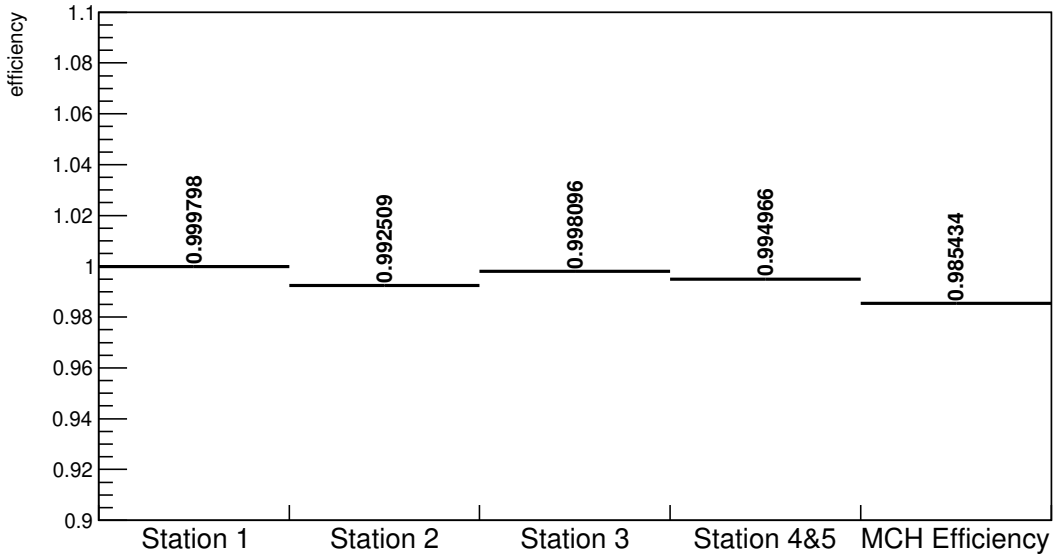

Figure 6.4: The tracking efficiency of the MCH stations vs. station ID and of full MCH extracted from a sample of pp collisions at $\sqrt{s} = 13.6$ TeV.

a function of p_T. The plot shows a 99% tracking efficiency of the stations and the MCH detector across all the p_T ranges.

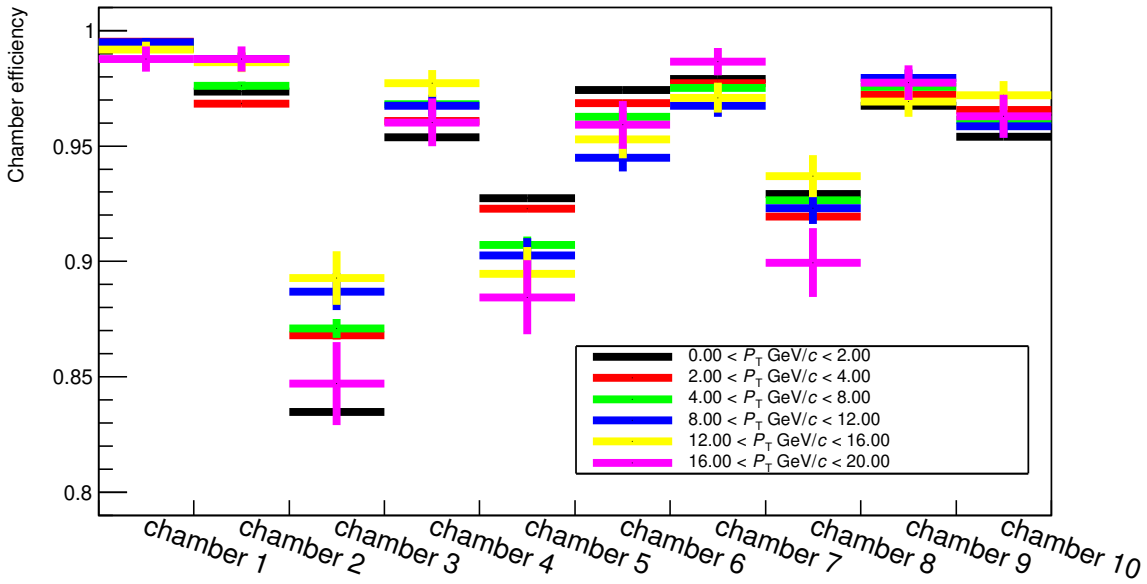

Figure 6.5: The tracking efficiency of the MCH tracking chambers vs. chamber ID. The efficiency for each chamber is shown in six intervals of p_T.

Figures 6.7 and 6.8 present the η dependence of the tracking efficiency of the MCH chambers and stations, respectively. The MCH chambers show efficiency values higher than 90% for all η intervals, except for chamber 3, which has an efficiency ranging between 80 - 85%. The issue with chamber 3 low efficiency is going to be discussed in more detail in 6.3.3. The MCH efficiency per station is presented in Fig.6.8, showing a high efficiency for all the stations, as well as for the full MCH detector in all η intervals. No trend is observed for the efficiency as a function of η.

We have also studied the efficiency of the MCH detector as a function of the azimuthal angle ϕ. Figure 6.9 presents the efficiency of the MCH chambers for four intervals of ϕ. Chamber 3 shows a very low efficiency ~ 60% in the range $0 < \eta < 1.57$. This particular ϕ angle corresponds to a specific location in station 2 and gives a first indication about where the problem may come from. A relatively low efficiency ~ 85% is observed for different ϕ intervals in chambers 5 and 8, as already spotted in the p_T and η dependent studies. The efficiency of the MCH stations and the overall efficiency of the MCH detector is higher than 98% in all the ϕ intervals.

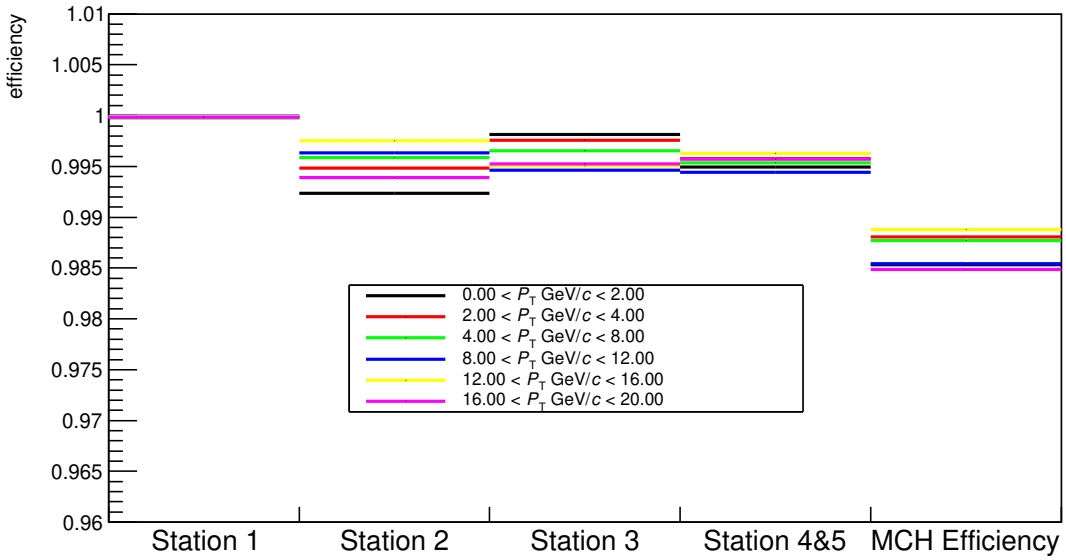

Figure 6.6: The tracking efficiency of the MCH tracking stations vs. station ID. The efficiency for each station is shown in six intervals of p_T. The last bin of the figure shows the MCH detector efficiency.

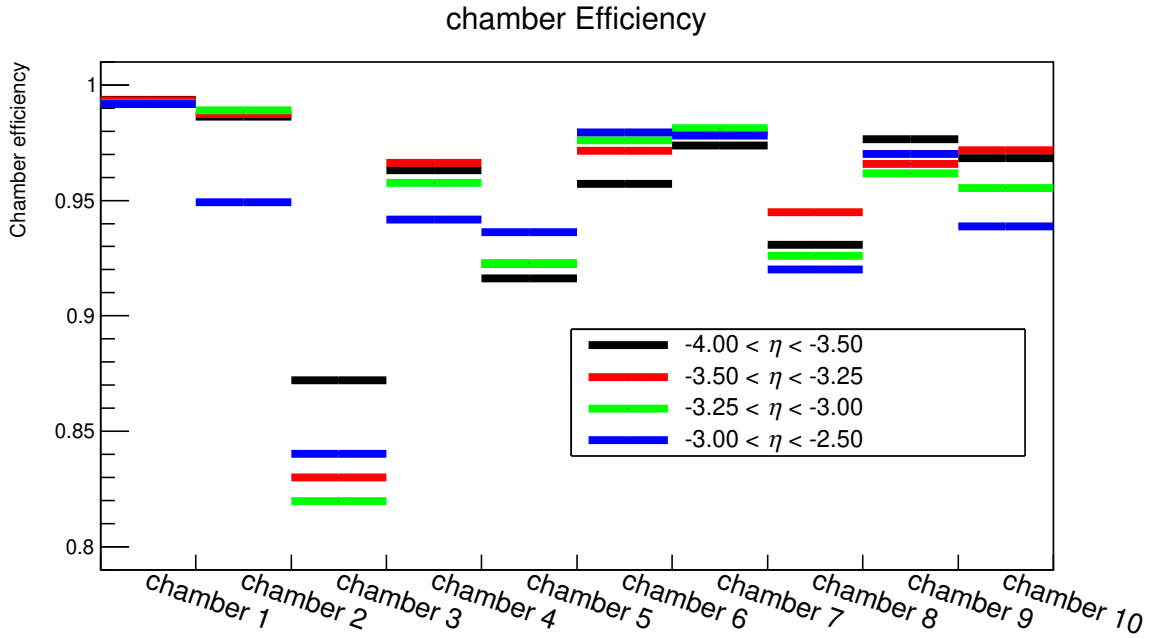

Figure 6.7: The tracking efficiency of the MCH tracking chambers vs. chamber ID. The efficiency for each chamber is shown in four intervals of η.

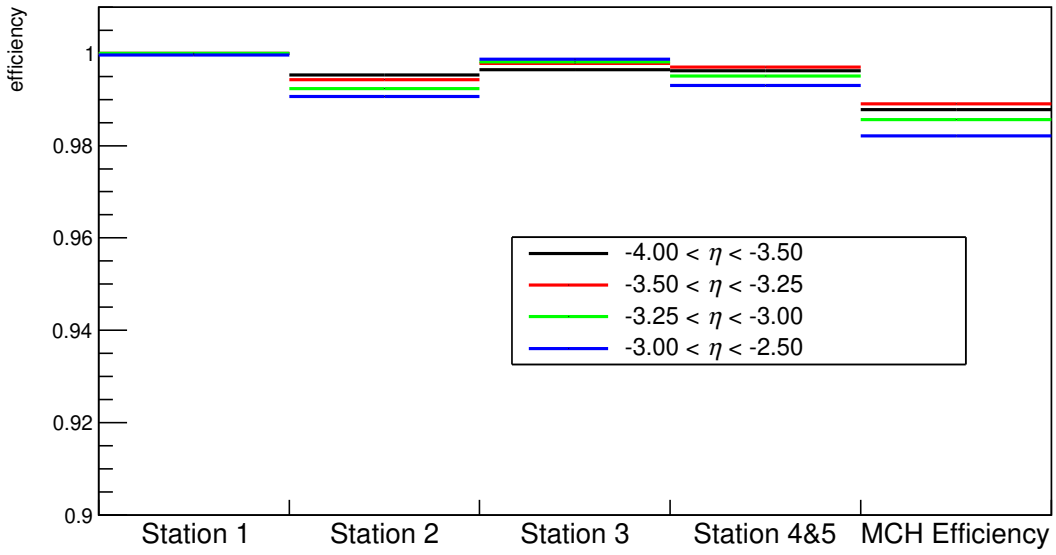

Figure 6.8: The tracking efficiency of the MCH tracking stations vs. station ID. The efficiency for each station is shown in four intervals of η. The last bin of the figure shows the MCH detector efficiency.

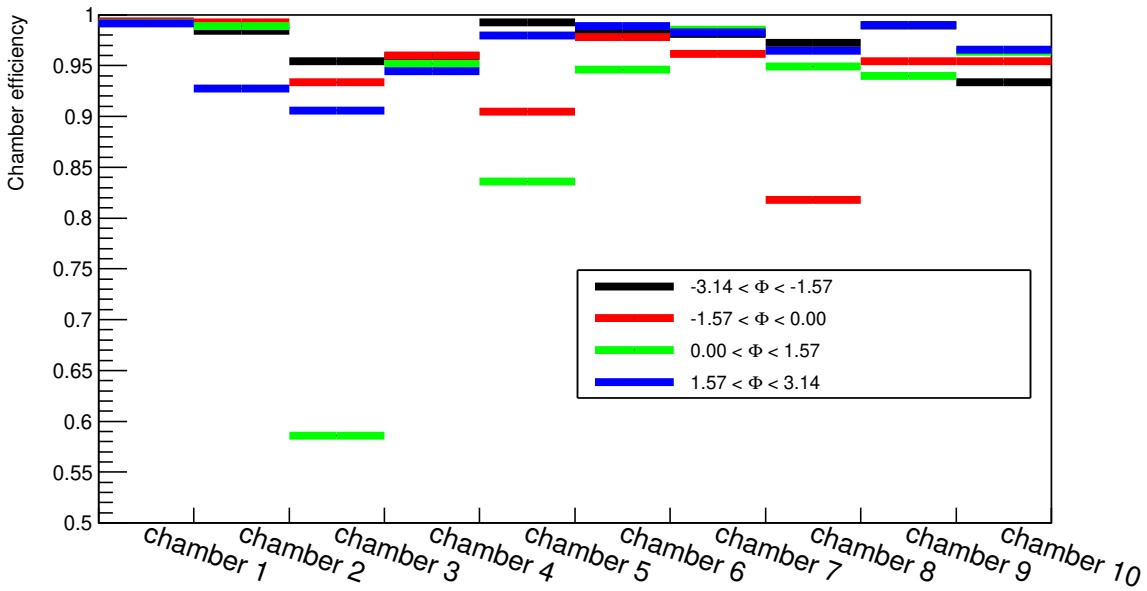

Figure 6.9: The tracking efficiency of the MCH tracking chambers vs. chamber ID. The efficiency for each chamber is shown in four intervals of azimuthal angle ϕ.

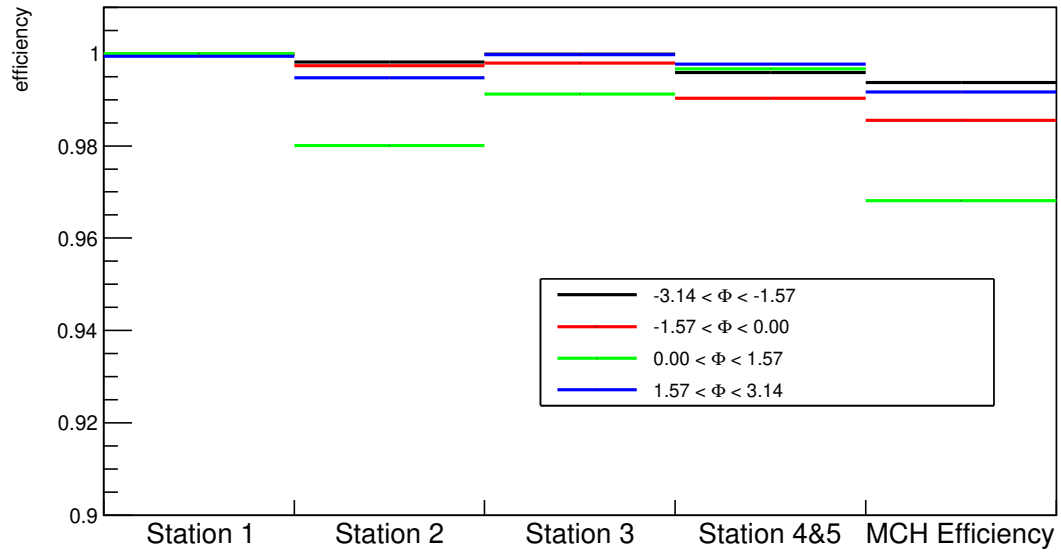

Figure 6.10: The tracking efficiency of the MCH tracking stations vs. station ID. The efficiency for each station is shown in four intervals of azimuthal angle ϕ. The last bin of the figure shows the MCH detector efficiency.

6.3.3 2D tracking efficiency studies per MCH chamber

In order to understand the low tracking efficiency observed for chambers 3, 5 and 8 and identify any potential dead areas in the MCH chambers, we have represented the tracking efficiency of the MCH chambers in 2D, exploiting η and ϕ variables. Figure 6.11 displays the computed tracking efficiency as a function of η and ϕ for the 10 MCH chambers. A very low tracking efficiency, depicted by a blue color, is clearly visible in some areas of chambers 2, 3, 5, and 8. These are the areas likely to have hardware or detector issues that will require to be fixed. We also need to understand these issues so they can be implemented in simulations to reproduce as well as possible the real status of the detector.
The 2D η and ϕ representation from Fig. 6.11 cannot be translated directly to chamber coordinates. To investigate the low tracking efficiency spots, we will also use the 2D representation of the fired pads (see Fig. 6.12) from the Quality Control (QC) of this particular run. The QC embraces several processes to ensure, online and offline, that we are taking good-quality data.

In chamber 2, the low tracking efficiency in the range ($\phi \sim 2.9$) – ($\eta \sim 2.6$) translates into a reduced tracking efficiency along the edges of the top left quadrant of chamber 2. Vertically, one could retrieve a problem on the high voltage of this sector, which implies that

the particle detection is disabled. Horizontally, this corresponds to a SOLAR board (readout board which interfaces up to 40 FEE boards to the DAQ) that lost its configuration.

In chamber 3, the low tracking efficiency (blue band) is visible in the azimuth range [0,1] and spans over almost the full η range. This region corresponds to the top right quadrant of chamber 3 (third column of top part of ($\phi \sim 2.9$) – ($\eta \sim -2.6$)) where a vertical blue line is visible. This observation aligns with the quality control plot depicted in figure 6.12, which indicates a low occupancy region (blue line) in the first quadrant. The low efficiency is due to a fault on a wire inside the chamber that required to disconnect a group of wires from the high-voltage distribution circuit. This quadrant was opened and repaired during the 2022 winter shutdown.

In chamber 5, the low tracking efficiency is centered at ($\phi \sim 0$) and extends over the full η range. This problem is also visible in the bottom part of Fig.6.12 in the middle of the right side of chamber 5. However, this issue seems to be transient and only appeared in a few runs. Its origin, low voltage power supply issue, or SOLAR board loss of configuration was not clearly established.

In chamber 8, the low tracking efficiency is strongest at ($\phi \sim -1.4$) and large η and extends up to ($\phi \sim -0.8$) and ($\eta \sim 3.5$). This can be correlated to a fully missing slat in the bottom right part of chamber 8. This fault is due to a faulty channel in the low-voltage power supply, thus the FEE is not powered.

We have successfully correlated the low tracking efficiency areas from pp data with the issues detected by the Quality Control for a dedicated run. This demonstrates that our tracking efficiency calculation method can effectively reproduce the inactive parts of the MCH detector.

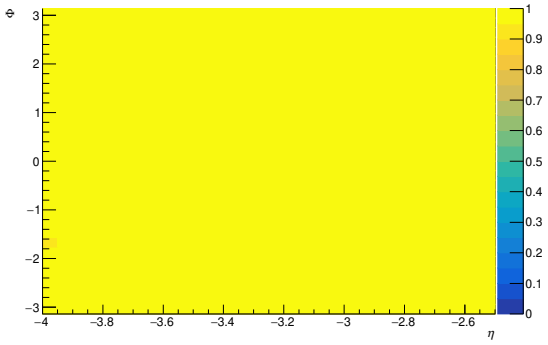

(a) chamber 1

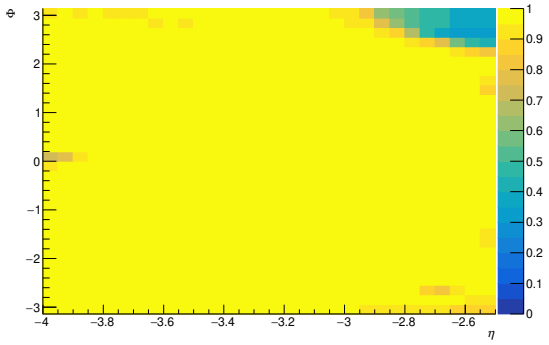

(b) chamber 2

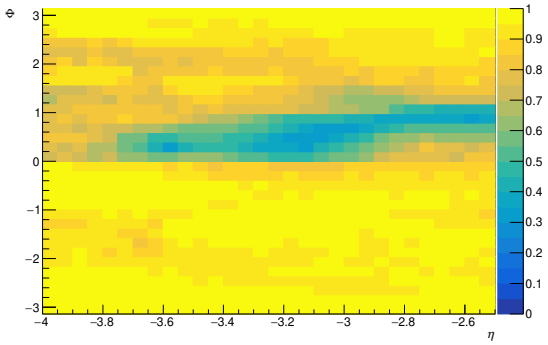

(c) chamber 3

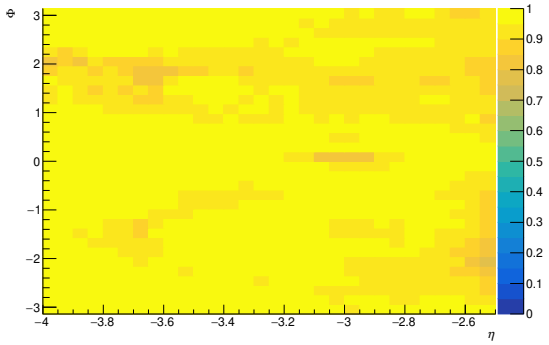

(d) chamber 4

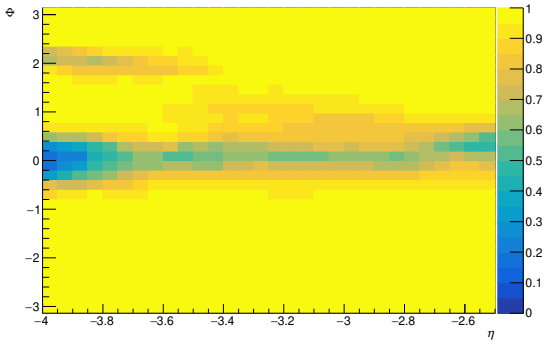

(e) chamber 5

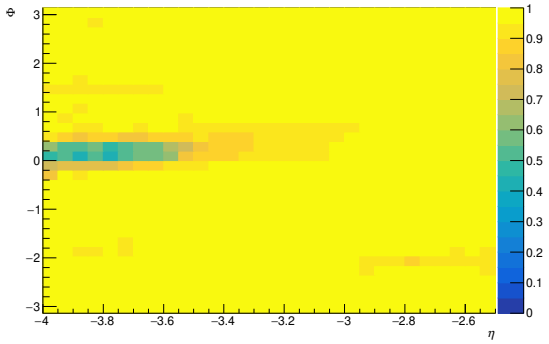

(f) chamber 6

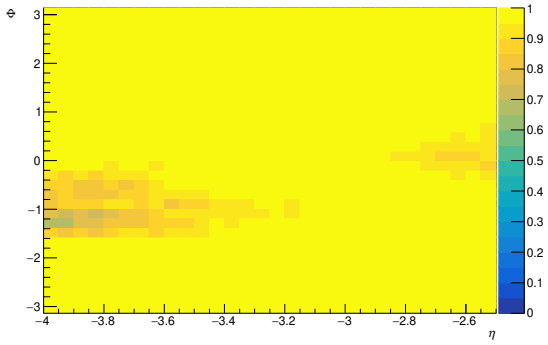

(g) chamber 7

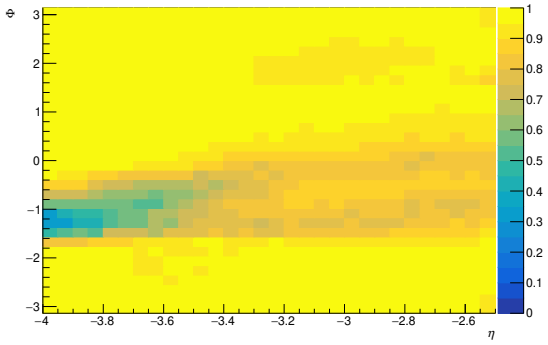

(h) chamber 8

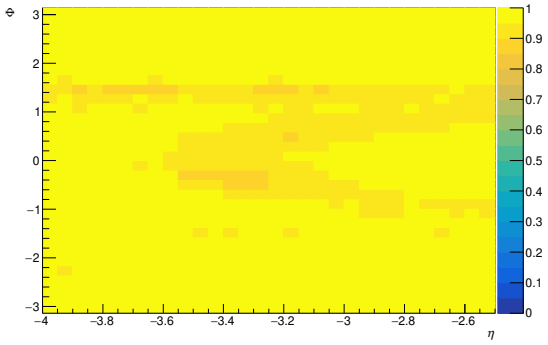

(i) chamber 9

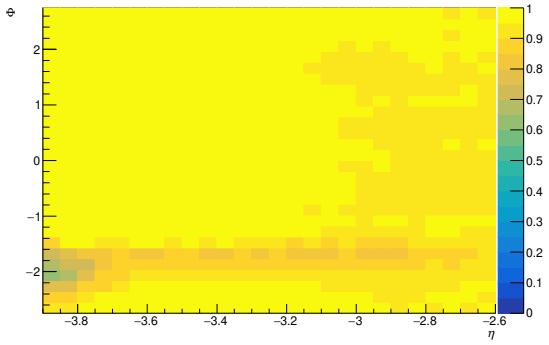

(j) chamber 10

Figure 6.11: MCH chambers tracking efficiency as a function of η and ϕ.

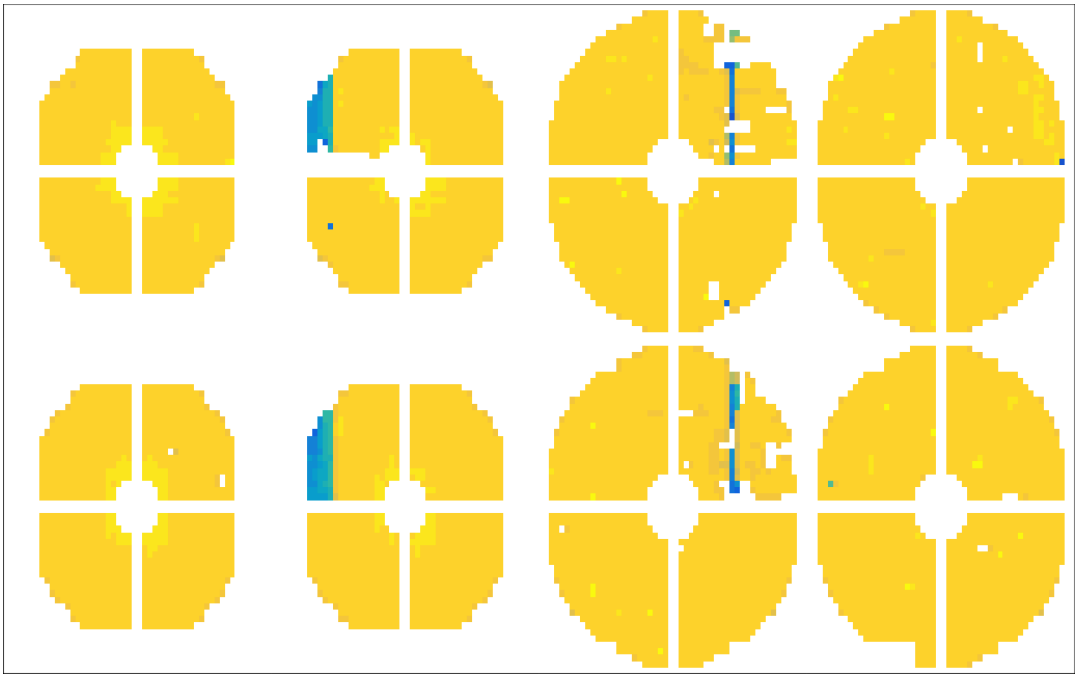

(a)

(b)

Figure 6.12: Plots from Quality Control for run 523306 showing the 2D x-y distribution of fired pads. The top part (a) shows chambers 1, 2, 3 and 4 bending planes on the first line and non-bending planes on the second line. The top part (b) shows chambers 5, 6, 7, 8, 9 and 10 bending planes on the first line and non-bending planes on the second line.

6.4 Tracking efficiency studies in Monte Carlo

In this section, we present the estimated MCH tracking efficiency based on MC simulations for pp collisions at $\sqrt{s}$ = 13.6 TeV. We used an ideal MC simulations (named LHC21i3g2 in the ALICE jargon) that considers a perfect detector to calculate the results since the software to retrieve and to include realistic data taking conditions has not been released at the time of this thesis. The same procedure as the one described in Sec.6.2 was followed to estimate the MCH tracking efficiency.

6.4.1 Integrated MCH tracking efficiency

The tracking efficiency integrated over p_{T}, y, and ϕ is presented in Fig.6.13 as a function of the chamber ID. The computed tracking efficiency is higher than 99.2% for all the MCH chambers.

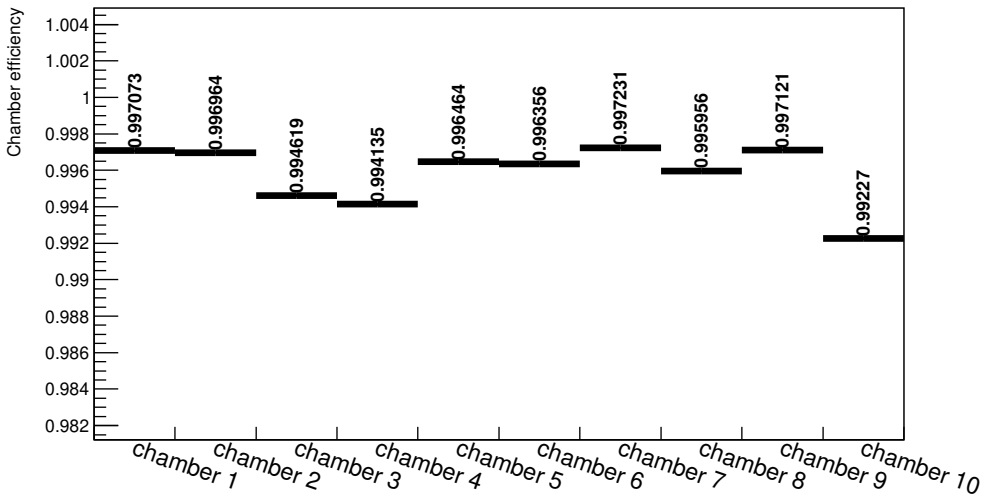

Figure 6.13: The tracking efficiency of the MCH chambers vs. chamber ID extracted from an ideal MC simulation for pp collisions at $\sqrt{s}$ = 13.6 TeV.

Fig.6.14 displays the tracking efficiency of the MCH stations. The result shows an efficiency higher than 99.9% in all the stations. The full MCH detector efficiency is shown in the last bin of Fig.6.14 and reaches an efficiency of 99.9% as well.

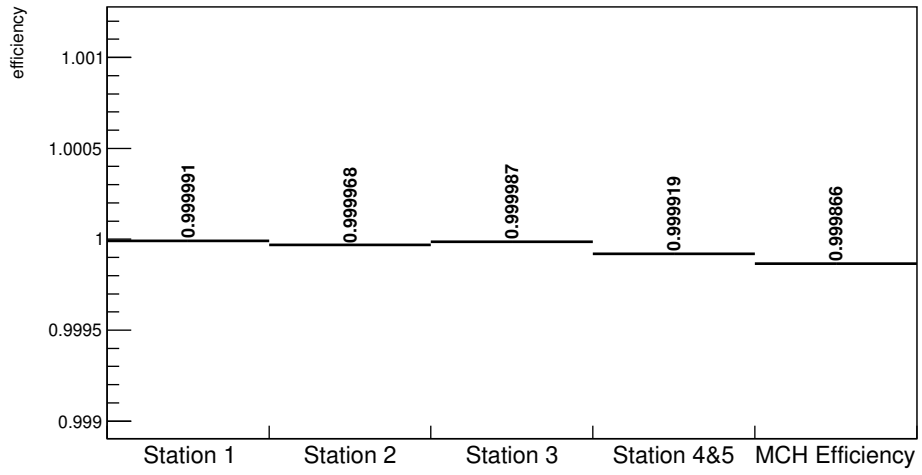

Figure 6.14: The tracking efficiency of the MCH chambers vs. station ID extracted from an ideal MC simulation for pp collisions at $\sqrt{s}$ = 13.6 TeV. The last bin of the figure presents the MCH detector efficiency.

6.4.2 Tracking efficiency as a function of p_{T}, η, and ϕ

In this section, we present the MCH tracking efficiency extracted from MC as a function of the track kinematic variables p_{T}, η, and ϕ. The p_{T}-differential chamber efficiency is presented in Fig.6.15. The tracking efficiency exceeds 99% for all MCH chambers and across all p_{T} intervals.
In Fig.6.16, we present the η-differential of the MCH chamber efficiency. The MCH chambers show an efficiency higher than 99% in all η intervals. No trend is observed for the efficiency as a function of η.
Finally, we have also studied the azimuthal angle ϕ dependence of the MCH tracking efficiency, which is presented in Fig.6.17. The tracking efficiency is higher than 99% for all the chambers in all ϕ intervals.
In conclusion, the MCH chamber efficiency has been studied as a function of p_{T}, η, and ϕ. We obtained an efficiency exceeding 99% in all the results, which is compatible with the expectations from ideal MC simulations.

6.4.3 2D tracking efficiency studies per MCH chamber

In this section, we show the results for the MCH tracking efficiency as a function of η and ϕ obtained from ideal MC simulations. A similar study has been carried out using

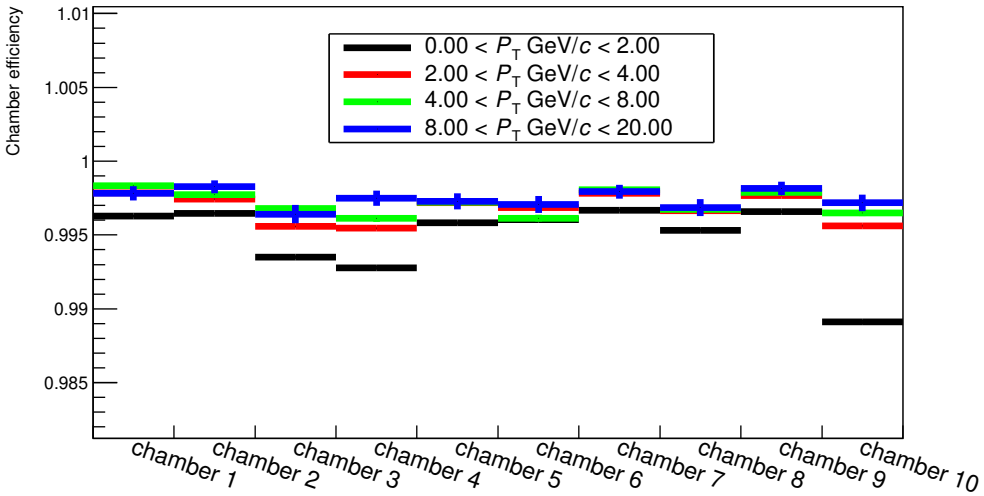

Figure 6.15: The tracking efficiency of the MCH tracking chambers vs. chamber ID. The efficiency for each chamber is shown in four intervals of p_T. The results are obtained with an ideal MC for pp collisions at $\sqrt{s}$ = 13.6 TeV.

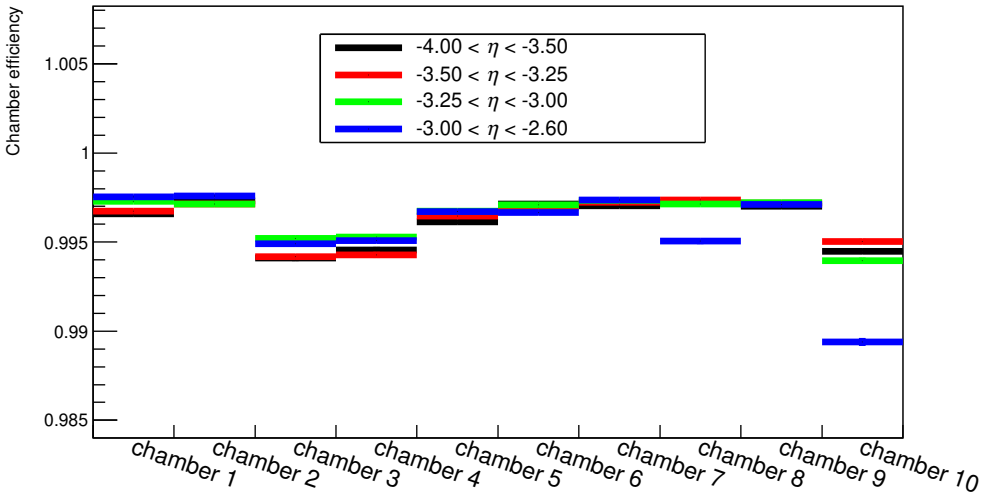

Figure 6.16: The tracking efficiency of the MCH tracking chambers vs. chamber ID. The efficiency for each chamber is shown in four intervals of η. The results are performed with an ideal MC for pp collisions at $\sqrt{s}$ = 13.6 TeV.

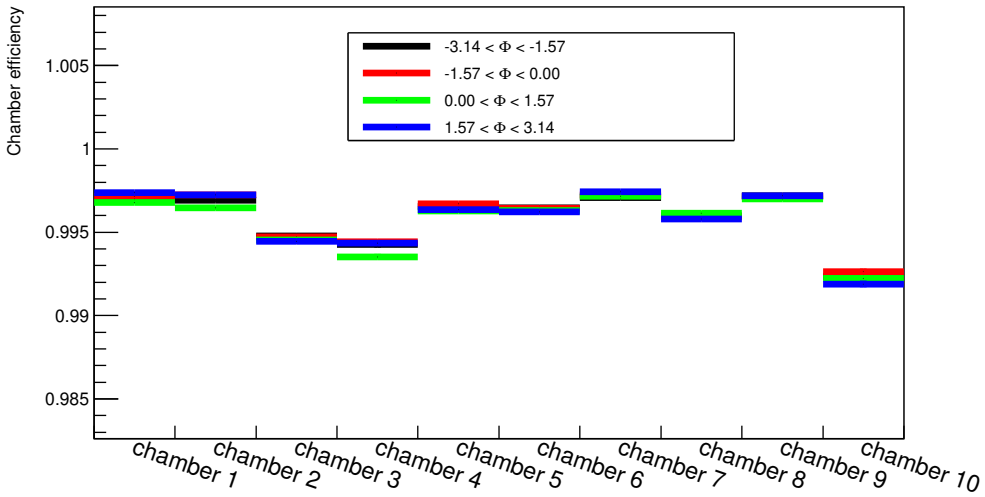

Figure 6.17: The tracking efficiency of the MCH tracking chambers vs. chamber ID. The efficiency for each chamber is shown in four intervals of ϕ. The results are performed with an ideal MC for pp collisions at $\sqrt{s}$ = 13.6 TeV.

data presented in Sec.6.3.3. Such analysis helps identify potential dead areas in the MCH chambers that might not be visible in the 1D efficiency studies. As an example, Fig.6.18 displays the ϕ–η dependence of the MCH tracking efficiency for chamber 1 and chamber 10. The result shows ~ 100% tracking efficiency in all the MCH chambers, similar to the efficiency obtained for chambers 1 and 10 shown in the example. It is worth noting that using the ideal MC we are not expecting to see any dead areas effect in the 2D MCH tracking efficiency, as there are no detector conditions implemented in such simulations.

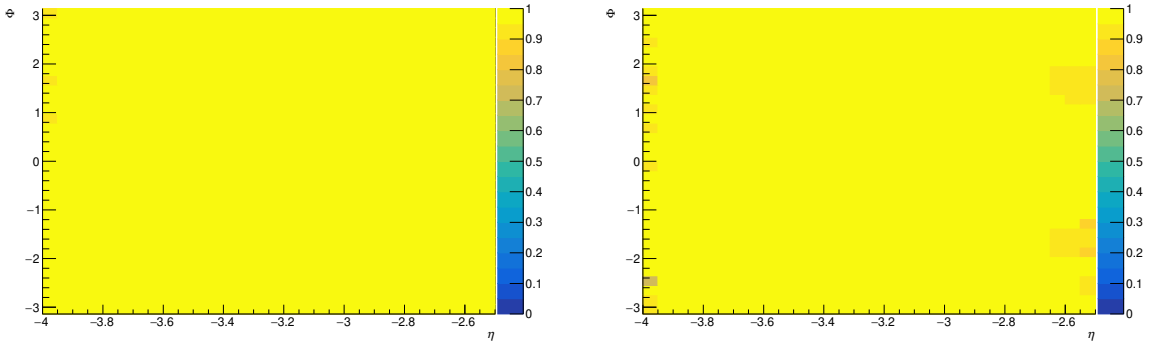

(a) chamber 1

(b) chamber 10

Figure 6.18: MCH chambers tracking efficiency as a function of η and ϕ from ideal MC simulation for pp collisions at $\sqrt{s}$ = 13.6 TeV. The presented plots are for chambers 1 and 10.

6.5 Systematic uncertainty determination

To estimate the uncertainty of the MCH tracking efficiency, we compare the efficiency computed from data and that obtained from MC simulations. The results of these comparisons are presented in Fig.6.19 for the tracking efficiency per chamber ID and in Fig.6.20 for the efficiency per station ID.

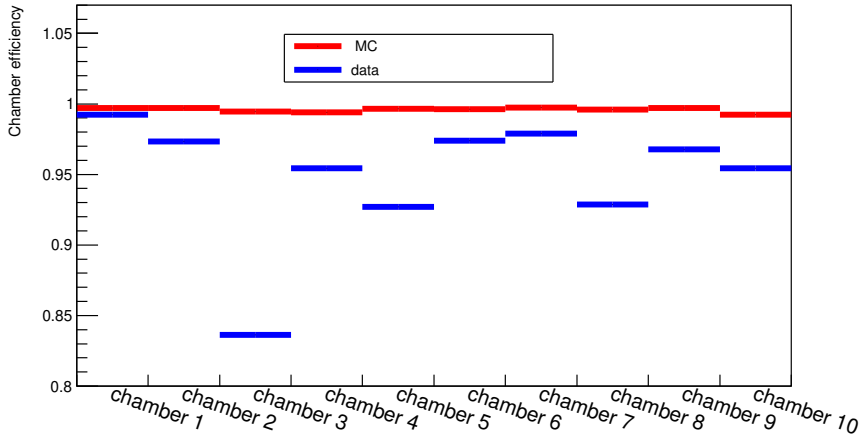

Figure 6.19: Comparison between MCH chamber efficiency extracted from ideal MC (in red) and the one extracted from data (in blue) for pp collisions at $\sqrt{s}$ = 13.6 TeV.

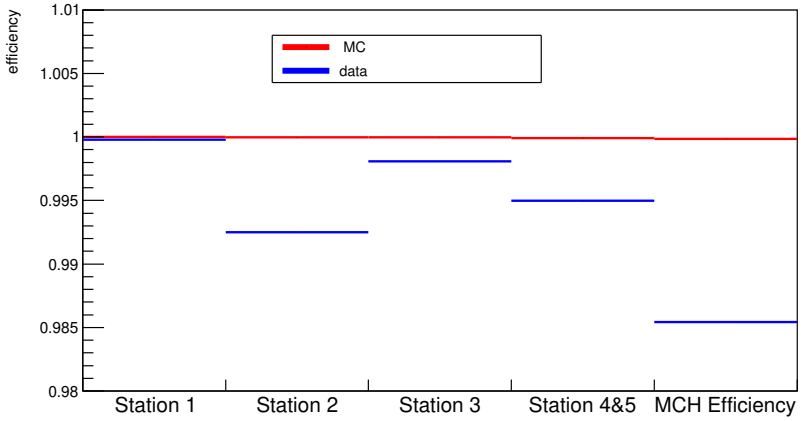

Figure 6.20: Comparison between MCH station efficiency extracted from ideal MC (in red) and the one extracted from data (in blue) for pp collisions at $\sqrt{s}$ = 13.6 TeV.

Significant differences are observed between the values obtained from data and MC, for both chamber and station tracking efficiencies. These discrepancies arise from two sources.

The first and dominant source is the missing description of realistic and time-dependent detector conditions in the MC simulations, which are, for now, only ideal. The work is ongoing to include in the MC simulations a realistic detector status so MC simulations can be anchored to data.
The second source is related to the kinematic distributions of the muon tracks in MC simulation. It is crucial to tune these distributions to data to ensure that they describe the kinematics of the true distributions. A data-driven procedure is performed to tune the MC p_{T}, ϕ, and η distributions on data. The same procedure has been followed when computing the $A \times \varepsilon$ for the $\psi(2S)$ multiplicity-dependent analysis. Fig.3.13, presents the flow chart of the iterative procedure that we followed to tune the MC distributions in data.

Part IV

Conclusion

7
Conclusion

In ultra-relativistic heavy-ion collisions, a deconfined state of quarks and gluons called Quark Gluon plasma (QGP) is formed. Several soft and hard observables are used to probe the QGP, such as charmonia. Charmonia are bound states of charm and anti-charm quarks. Given the heavy mass of the charm quarks, they are produced in the initial stages of the collision, before the QGP formation, and experience the full evolution of the system. Besides the QGP effects, these observables might be influenced by the presence of the nuclei, referred to as cold nuclear matter effects. Proton–nucleus collisions are used as a control system to disentangle the QGP effects from the cold nuclear matter effects, since the energy density of the system is not sufficient to create a QGP. Recently, several intriguing QGP-like behaviors have been observed at high multiplicity in small systems, i.e., proton–proton and proton–nucleus collisions. For example, the non-zero elliptic flow of charged particles, and the strange hadron production enhancement. These findings are surprising, as they are usually interpreted as QGP signatures in heavy-ion collisions. Multiparton interactions (MPI) are one of the scenarios proposed to interpret these behaviors. Charmonium production as a function of charged-particle multiplicity is a tool to probe the MPIs.
In this thesis, we measured the self-normalized charmonium yields as a function of the self-normalized charged-particle multiplicity. The analysis is performed using the data set of p–Pb collisions at $\sqrt{s_{\mathrm{NN}}} = 8.16$ TeV collected by the ALICE experiment. The charged-particle multiplicity is measured at midrapidity, $|y| < 1$, exploiting the information of the inner tracking system, where the number of track segments was used as a multiplicity estimator. The correlation between the number of tracklets and the charged-particle multiplicity is

evaluated using MC simulations. The information from the muon spectrometer is used to reconstruct the charmonium yields from their decay channel into dimuon at forward, $2.03 < y_{\mathrm{cms}} < 3.53$, and backward, $-4.46 < y_{\mathrm{cms}} < -2.96$, rapidity. The charmonium yields are extracted by fitting the invariant mass distribution of unlike-sign muon pairs. A significant effort was dedicated to achieve a stable fit procedure because of the limited statistics of $\psi(2S)$.

The normalized $\psi(2S)$ yields show an increase with increasing normalized multiplicity at both forward and backward rapidity. The yield increase is compatible with a linear trend with a slope close to unity. Moreover, the measurements are compared to the calculation from the percolation + comover + EPS09 model. The model describes the data trend within uncertainties in both rapidity regions. To disentangle any possible final state effect at play in p–Pb collisions, we measured the self-normalized $\psi(2S)$-over-J/ψ yields as a function of the self-normalized charged-particle multiplicity. The ratio presents a flat behavior; i.e. a similar behavior is observed for the J/ψ and $\psi(2S)$ as a function of multiplicity. The results are compared to the calculation from the comover model, which suggests a stronger suppression for the $\psi(2S)$ relative to J/ψ as a function of multiplicity. The comover model calculations are compatible with the data within uncertainties. The limited statistics prevents us from ruling out or drawing conclusions about possible final state effects.

The LHC Run 3 data-taking will provide higher luminosity to the experiments. This will allow us to perform measurements with higher precision. ALICE has been upgraded to cope with the increase of the collision rate. One of the main upgrades is the replacement of the electronics of the sub-detectors to enable ALICE to read out all Pb–Pb collisions at a high interaction rate. The main contribution of this thesis to the Run 3 data-taking is the development of the tools required to study the systematic uncertainty related to the tracking efficiency of the muon tracking chambers. We present the tracking efficiency of the muon tracking detector, both in bins of p_{T}, η, and ϕ, and integrated. The comparison between the tracking efficiency computed from ideal simulations and data from Run 3 is also presented. Such comparison is needed to assess the systematic uncertainty on the tracking efficiency when the anchored simulations will be available.

ALICE aims at collecting 50 nb^{-1} of p–Pb collisions as well as 200 pb^{-1} of pp collisions during Run 3 and 4 [107]. This luminosity increase will enhance the precision of measurements, particularly in the case of pp collisions, where the statistical uncertainty is expected to be reduced $\sim$ 3 times compared to Run 2 for the multiplicity-dependent charmonium production. In addition, the larger luminosity will allow us to reach higher multiplicity events, where MPIs are expected to play a more prominent role.

Furthermore, with the new muon forward tracker, we are able to separate the charmonia produced at the primary vertex and those originating from B-hadron decays. For multiplicity-dependent analysis, this will provide deeper insights into the behavior of charmonia and beauty-flavored hadrons as a function of multiplicity relative to currently available measurements.

A

Data set run numbers

Two data sets periods are used in this analysis to extract the charmonia raw yields: the LHC16r is the data set for p–Pb at forward rapidity, while the LHC16s is the p–Pb at backward rapidity. The analysed data sample consists of the following run numbers:

- **p–Pb period (LHC16r)**: 266318, 266316, 266312, 266305, 266304, 266300, 266299, 266296, 266235, 266234, 266208, 266197, 266196, 266193, 266190, 266189, 266187, 266117, 266086, 266085, 266084, 266081, 266076, 266074, 266034, 266025, 266023, 266022, 265841, 265840, 265797, 265795, 265792, 265789, 265788, 265787, 265785, 265756, 265754, 265746, 265744, 265742, 265741, 265740, 265714, 265713, 265709, 265701, 265700, 265698, 265697, 265696, 265694, 265691, 265607, 265596, 265594.

- **p–Pb period (LHC16s)**: 267131, 267110, 267109, 267077, 267072, 267070, 267067, 267063, 267062, 267022, 267020, 266997, 266994, 266993, 266988, 266944, 266943, 266942, 266940, 266915, 266912, 266886, 266885, 266883, 266882, 266880, 266878, 266857, 266807, 266805, 266800, 266776, 266775, 266708, 266706, 266703, 266702, 266676, 266674, 266669, 266668, 266665, 266659, 266658, 266657, 266630, 266621, 266618, 266614, 266613, 266595, 266593, 266591, 266588, 266587, 266549, 266543, 266539, 266534, 266533, 266525, 266523, 266522, 266520, 266518, 266516, 266514, 266487, 266480, 266472, 266470, 266441, 266439, 266438, 266437.

All the above-mentioned run numbers were chosen according to a QA criteria.

B

Fit description and tail parameters

The functions used to delineate the signal lineshape are the so called extended Crystal-Ball and extended NA60 functions.

B.1 Extended Crystal-Ball

The extended Crystal-Ball (CB) has seven parameters: normalisation factor N, two Gaussian core parameters (mean $\bar{x}$ and width σ), and four tail parameters (α, n, $\alpha\prime$ and $n\prime$). The function is defined as:

$$f(x) = N \cdot \begin{cases} \exp\left(\frac{-(x-\bar{x})^2}{2\sigma^2}\right) & \text{for } \alpha\prime > \frac{(x-\bar{x})}{\sigma} > -\alpha \\ A \cdot \left(B - \frac{(x-\bar{x})}{\sigma}\right)^{-n} & \text{for } \frac{(x-\bar{x})}{\sigma} \leq -\alpha \\ C \cdot \left(D + \frac{(x-\bar{x})}{\sigma}\right)^{-n'} & \text{for } \frac{(x-\bar{x})}{\sigma} \geq \alpha' \end{cases} \tag{B.1}$$

where

$$A = \left(\frac{n}{|\alpha|}\right)^n \cdot \exp\left(-\frac{|\alpha|^2}{2}\right), \qquad B = \frac{n}{|\alpha|} - |\alpha|,$$
$$C = \left(\frac{n\prime}{|\alpha\prime|}\right)^{n\prime} \cdot \exp\left(-\frac{|\alpha\prime|^2}{2}\right), \qquad D = \frac{n\prime}{|\alpha\prime|} - |\alpha\prime|.$$

Table B.1 summarises the parameters used for the Crystal-Ball tail description. In the table the tails extracted from data or MC are specified. The tails tagged as RA refer to those

extracted when the event selection criteria does not include neither vertex selection, nor pileup event rejection. Whereas tails tagged as JC refer to those extracted with the event selection criteria used in this analysis, including vertex and pileup selection criteria.

p–Pb period					
tag	data/MC	A	B	C	D
RA	data	0.944475	4.922742	1.891761	5.889739
JC	data	0.89	35.66	7.14	2.28
JC	MC	0.993676	2.90278	2.21568	2.80558
Pb–p period					
tag	data/MC	A	B	C	D
RA	data	0.889421	7.572801	1.893422	57.948783
JC	data	0.85	52.17	30.	57.01
JC	MC	0.978398	2.9648	2.24946	2.74322
pp 13 TeV					
tag	data/MC	A	B	C	D
pp13	data	0.98	6.97	1.86	14.99
pp13	MC	1.0116	3.3694	2.2731	2.6237

Table B.1: Parameters used for the Crystal-Ball tails definition.

B.2 Extended NA60

The function has the following eleven parameters: normalisation factor N, two Gaussian core parameters (mean $\bar{x}$ and width σ), and eight tail parameters (α_L, p_1^L, p_2^L, p_3^L, α_R, p_1^R, p_2^R and p_3^R). The function is defined as:

$$f(x) = N \cdot \exp\left(-0.5\left(\frac{t}{t_0}\right)^2\right) \qquad \text{with} \qquad t = \frac{x-\bar{x}}{\sigma}, \tag{B.2}$$

and

$$t_0 = \begin{cases} 1 + p_1^L\left(\alpha^L - t\right)^{\left(p_2^L - p_3^L\sqrt{\alpha^L - t}\right)} & \text{for } t < \alpha^L \\ 1 & \text{for } \alpha^L < t < \alpha^R \\ 1 + p_1^R\left(t - \alpha^R\right)^{\left(p_2^R - p_3^R\sqrt{t-\alpha^R}\right)} & \text{for } t > \alpha^R \end{cases}$$

p–Pb period									
tag	data/MC	α^R	p_1^R	p_2^R	p_3^R	α^L	p_1^L	p_2^L	p_3^L
JC	MC	0.002847	0.447453	0.225085	0.008193	0.766468	0.328259	-0.786211	2.020080
Pb–p period									
tag	data/MC	α^R	p_1^R	p_2^R	p_3^R	α^L	p_1^L	p_2^L	p_3^L
JC	MC	0.002881	0.447732	0.225378	0.007315	0.722032	0.311685	-0.792803	2.146690

Table B.2: Parameters used for the NA60 tail definition.

C

J/ψ raw yields in multiplicity intervals

Figures. C.1, C.2, C.3, C.4 show the fit results for J/ψ raw yields in all the multiplicity bins.

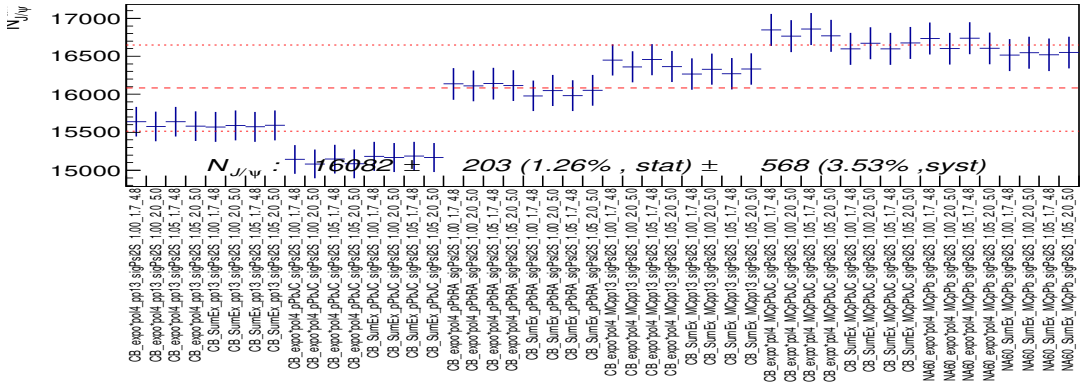

(a) forward rapidity, multiplicity interval $|1,20|$

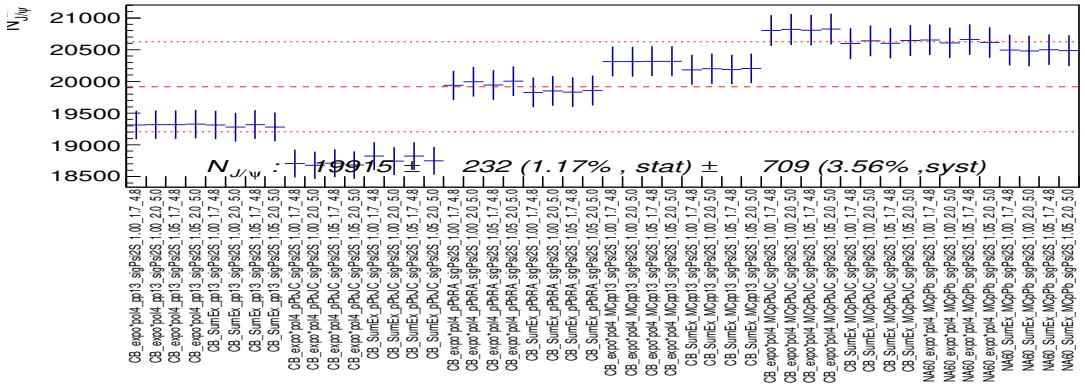

(b) forward rapidity, multiplicity interval $|21,31|$

Figure C.1: Number of J/ψ for the forward rapidity in multiplicity intervals.

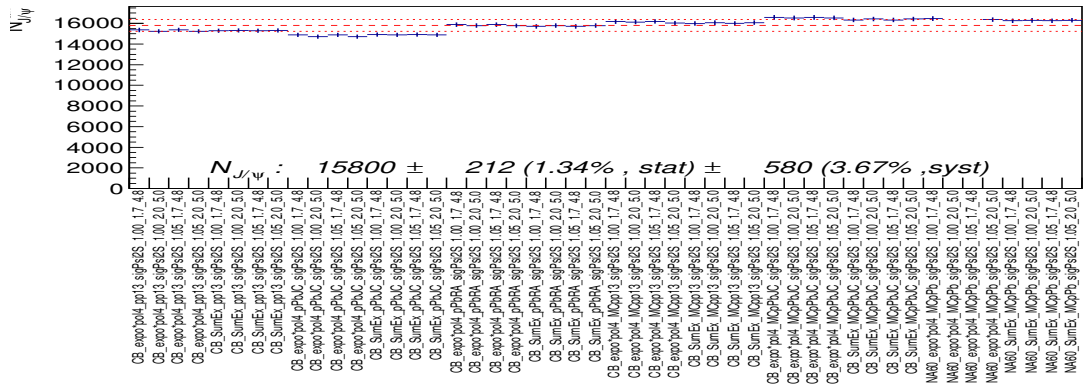

(a) forward rapidity, multiplicity interval |32,41|

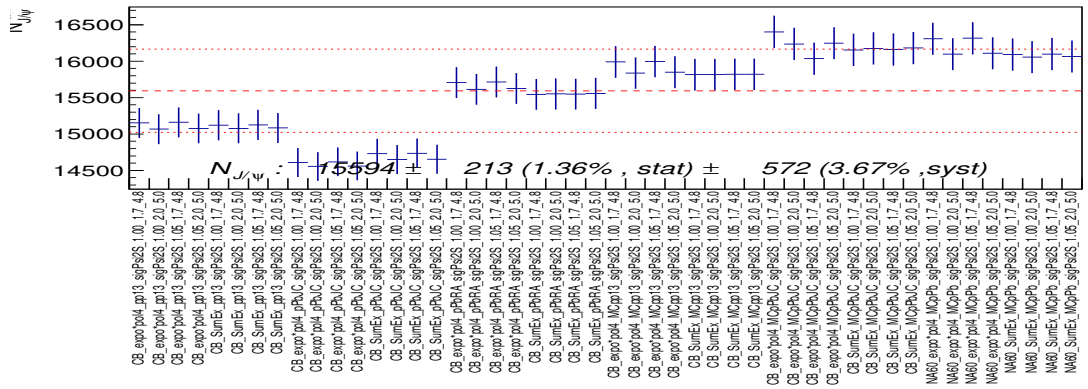

(b) forward rapidity, multiplicity interval |42,56|

Figure C.2: Number of J/ψ for the forward rapidity in multiplicity intervals.

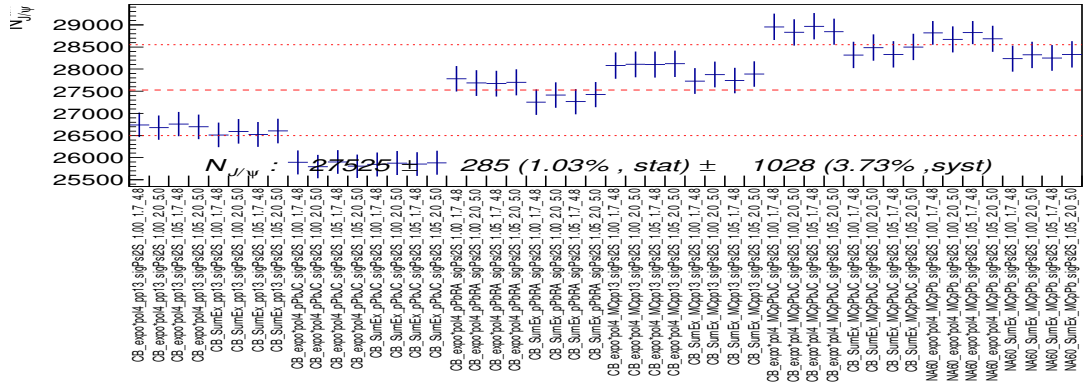

(a) forward rapidity, multiplicity interval |57,67|

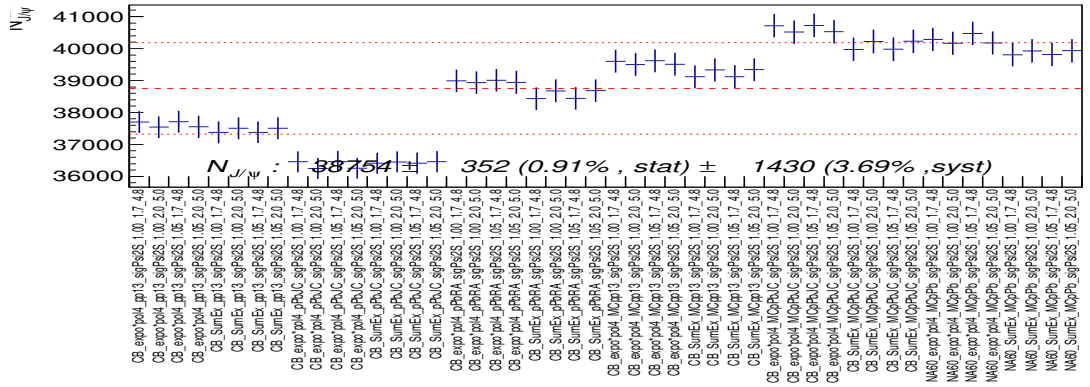

(b) forward rapidity, multiplicity interval |68,300|

Figure C.3: Number of J/ψ for the forward rapidity in multiplicity intervals.

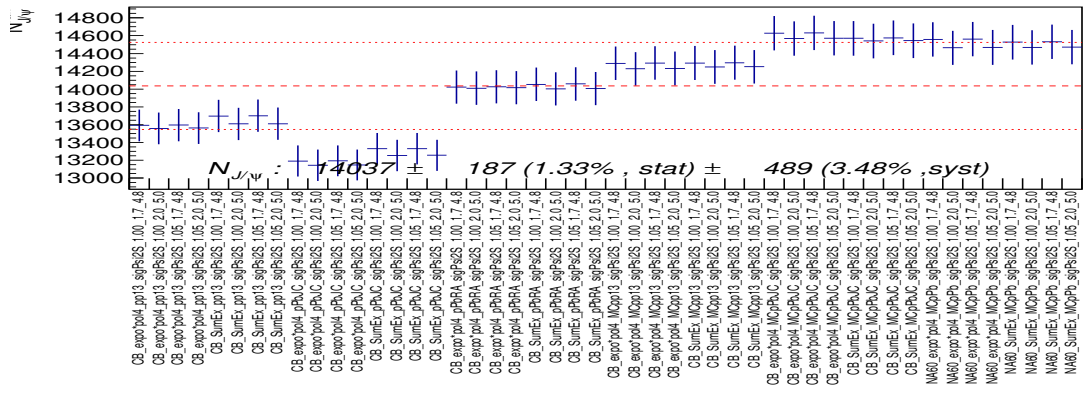

(a) backward, multiplicity interval $|1,18|$

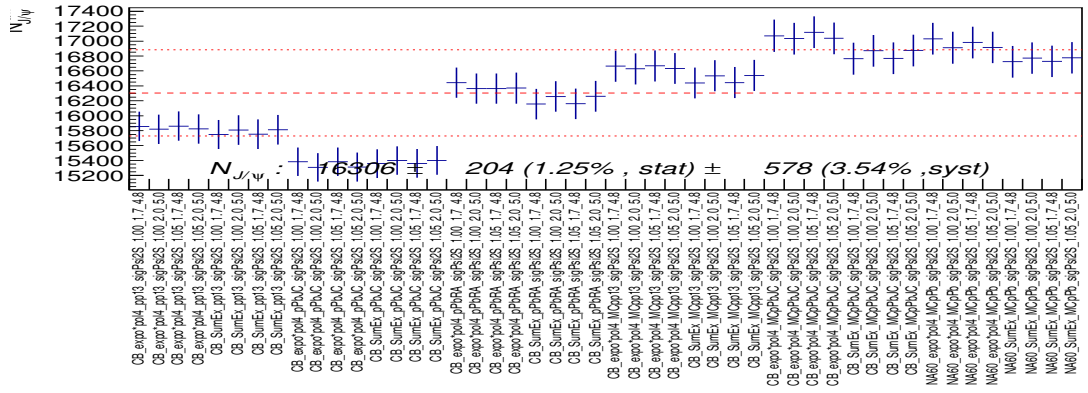

(b) backward, multiplicity interval $|19,27|$

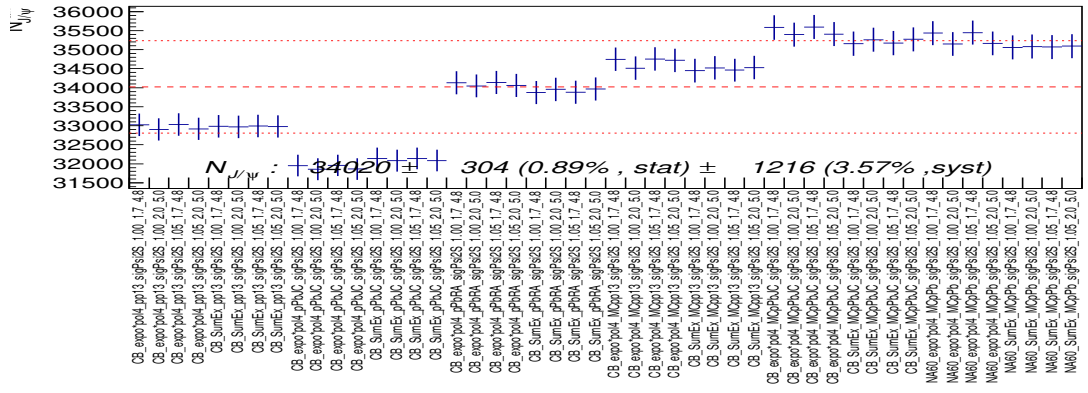

(c) backward, multiplicity interval $|28,41|$

Figure C.4: Number of J/ψ for the backward rapidity in multiplicity intervals.

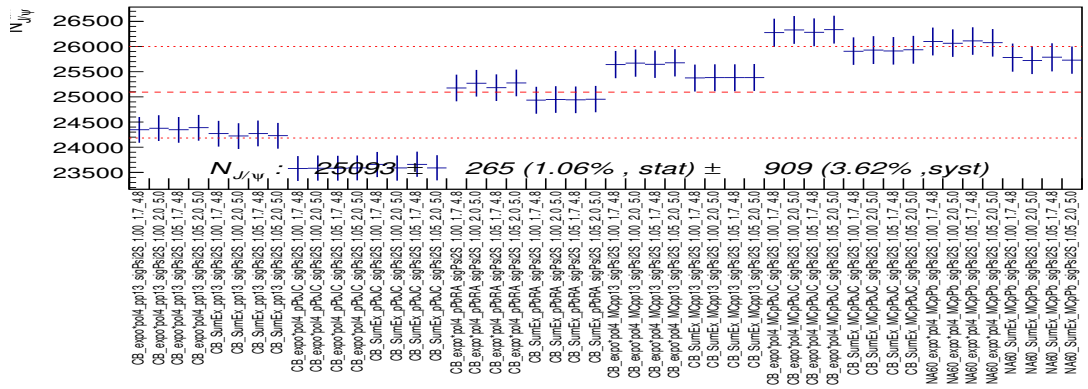

(a) backward, multiplicity interval $|42,50|$

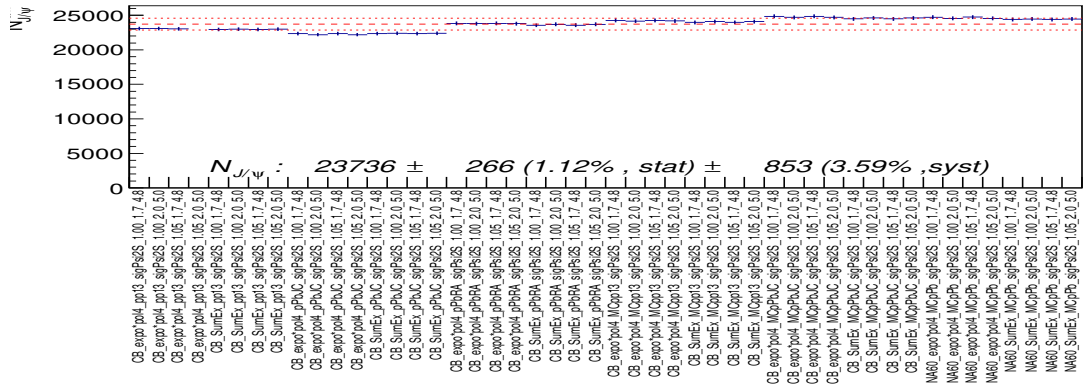

(b) backward, multiplicity interval $|51,59|$

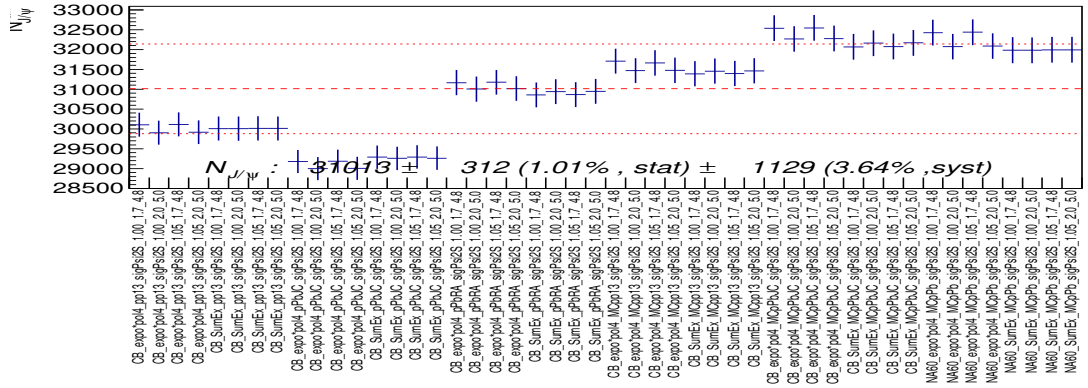

(c) backward, multiplicity interval $|60,73|$

Figure C.5: Number of J/ψ for the backward rapidity in multiplicity intervals.

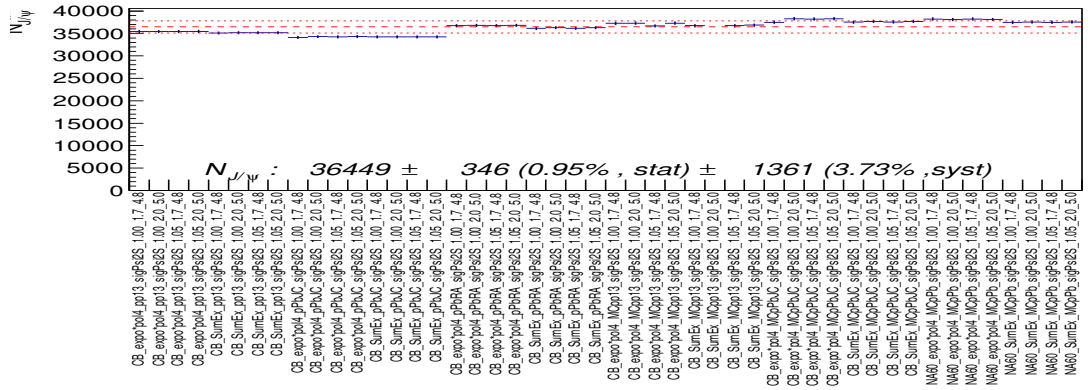

(a) backward, multiplicity interval |74, 102|

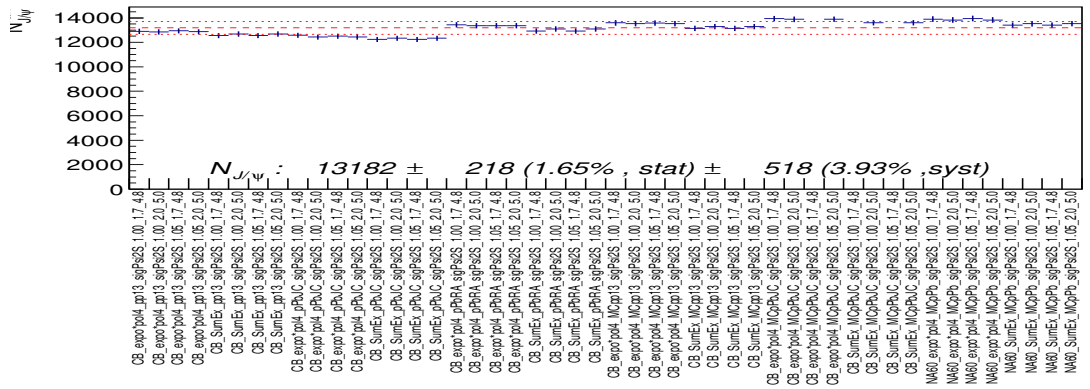

(b) backward, multiplicity interval |103, 350|

Figure C.6: Number of J/ψ for the backward rapidity in multiplicity intervals.

D

$\psi(2S)$ raw yields in multiplicity intervals

Fig. D.1, D.2, D.4, D.5 and D.6 report the fit results for $\psi(2S)$ in all multiplicity intervals for both periods.

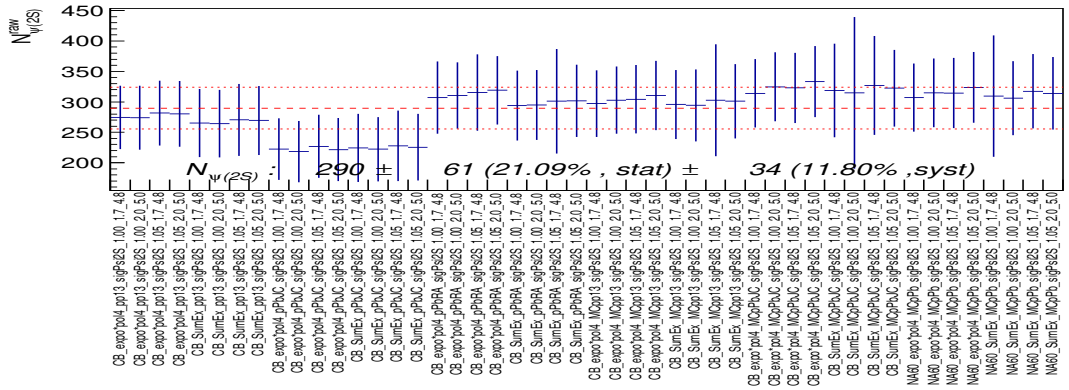

(a) Forward rapidity, multiplicity interval $|1,20|$

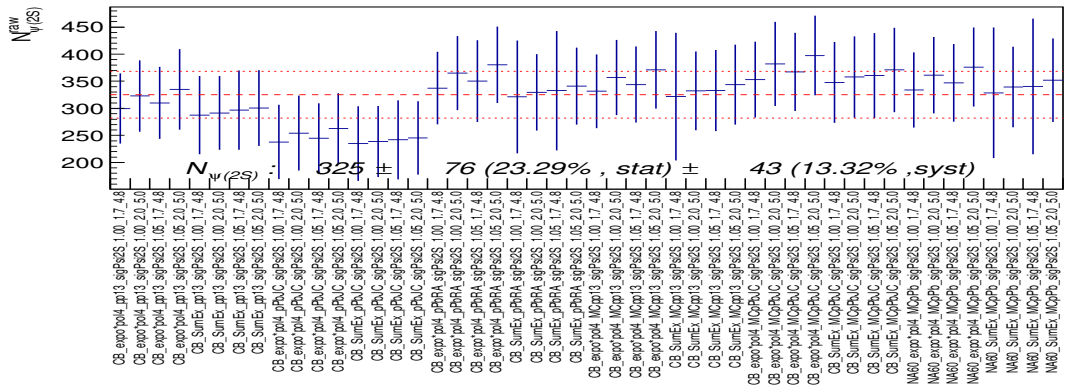

(b) forward rapidity, multiplicity interval $|21,31|$

Figure D.1: Number of $\psi(2S)$ for the forward rapidity in multiplicity intervals.

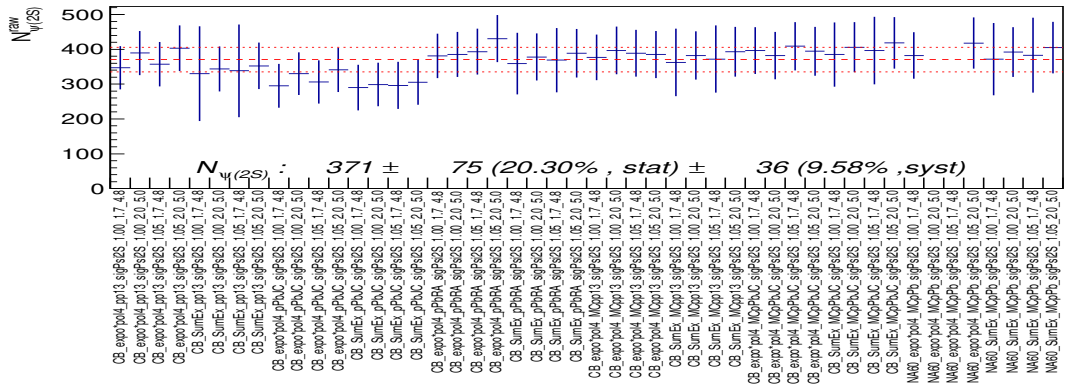

(a) Forward rapidity, multiplicity interval |32,41|

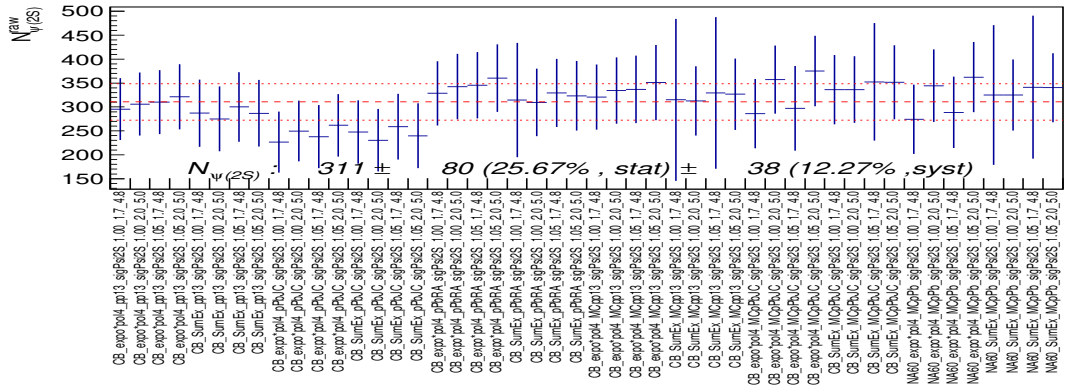

(b) Forward rapidity, multiplicity interval |42,56|

Figure D.2: Number of ψ(2S) for the forward rapidity in multiplicity intervals.

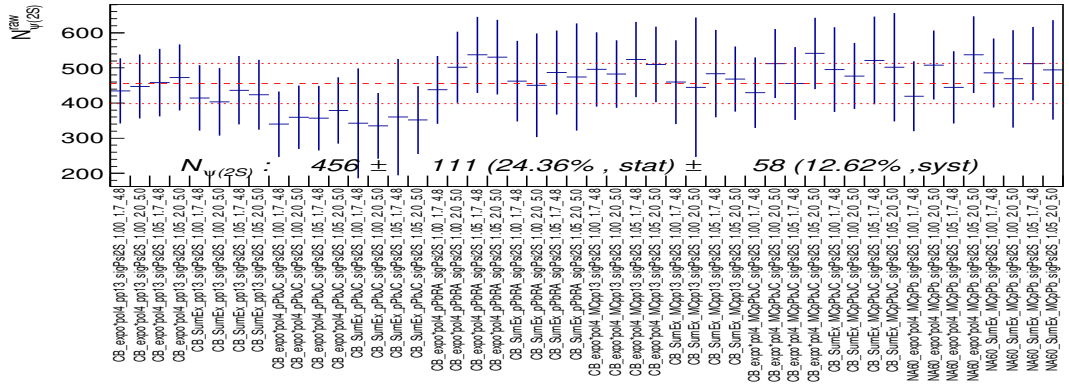

(a) Forward rapidity, multiplicity interval $|57,67|$

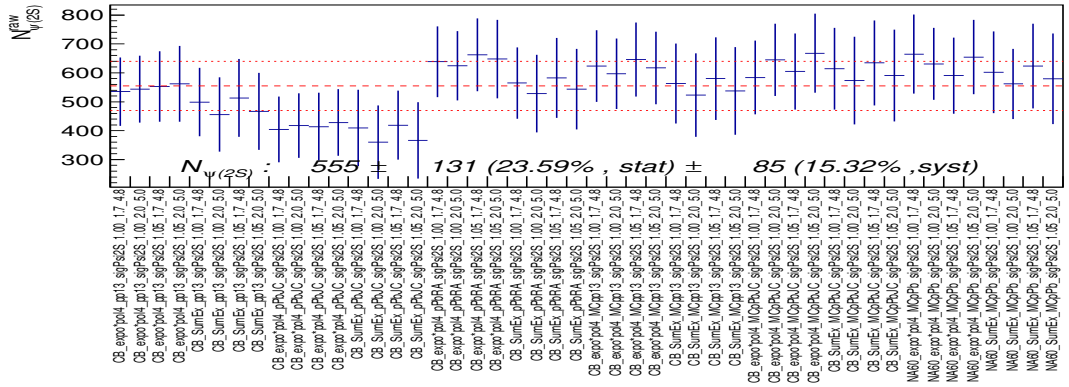

(b) Forward rapidity, multiplicity interval $|68,300|$

Figure D.3: Number of $\psi(2S)$ for the forward rapidity in multiplicity intervals.

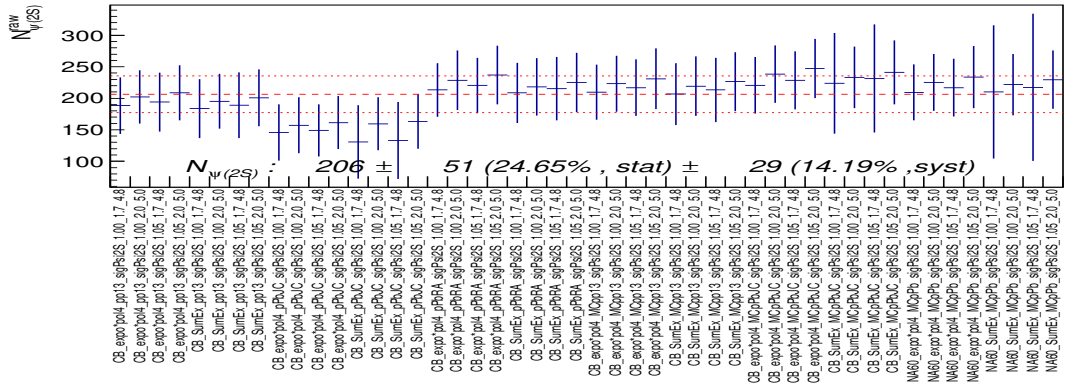

(a) Backward rapidity, multiplicity interval $|1,18|$

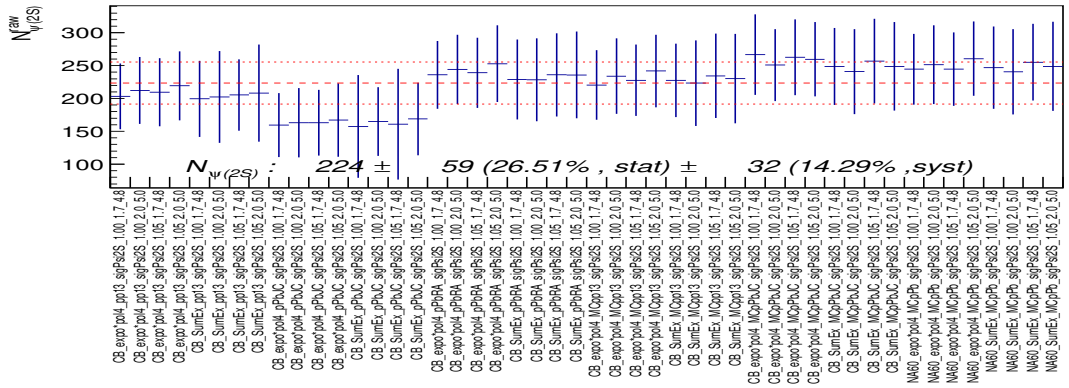

(b) Backward rapidity, multiplicity interval $|19,27|$

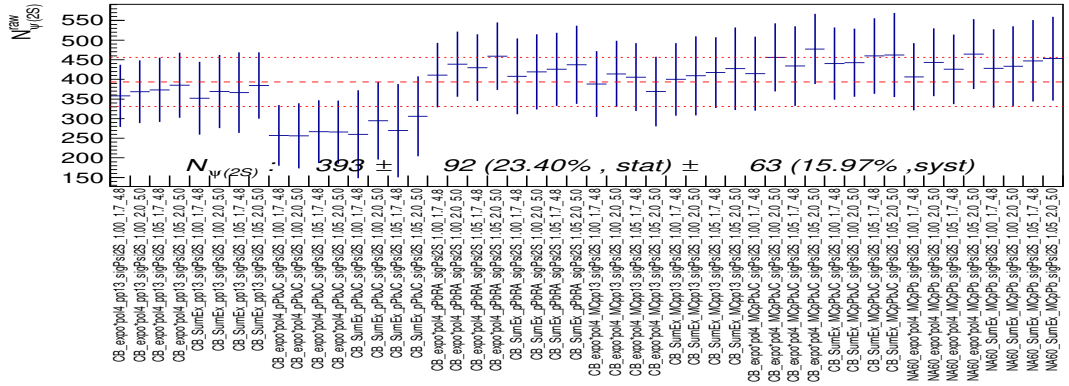

(c) Backward rapidity, multiplicity interval $|28,41|$

Figure D.4: Number of $\psi(2S)$ for the backward rapidity in multiplicity intervals.

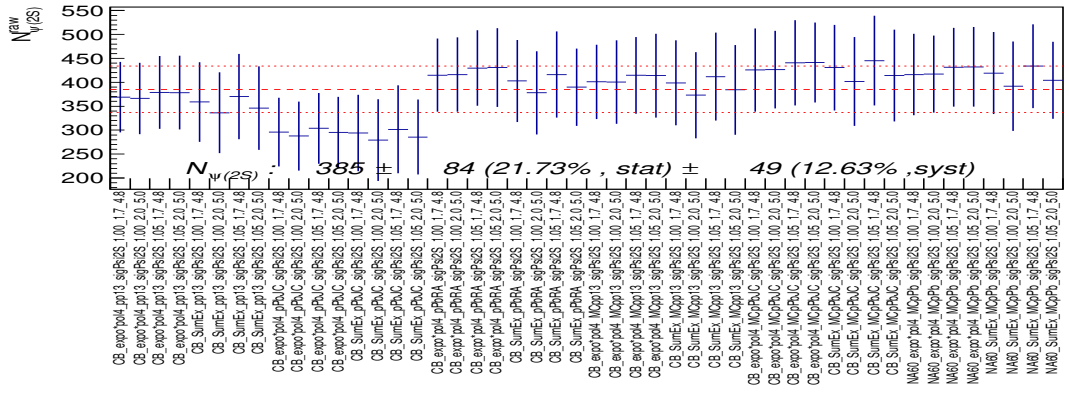

(a) Backward rapidity, multiplicity interval $|42,50|$

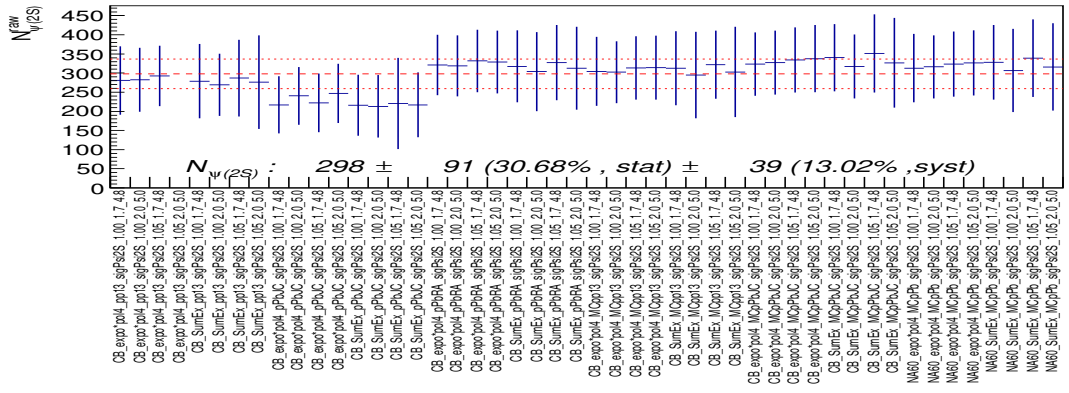

(b) Backward rapidity, multiplicity interval $|51,59|$

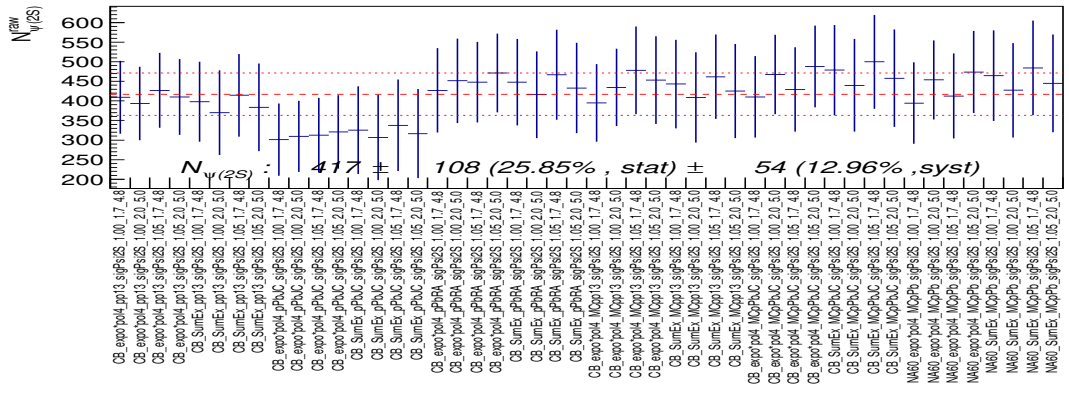

(c) Backward rapidity, multiplicity interval $|60,73|$

Figure D.5: Number of $\psi(2S)$ for the backward rapidity in multiplicity intervals.

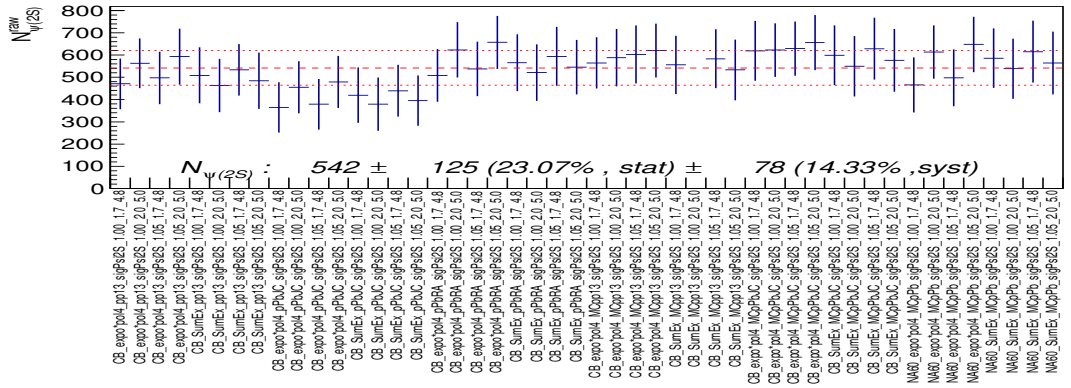

(a) Backward rapidity, multiplicity interval |74, 102|

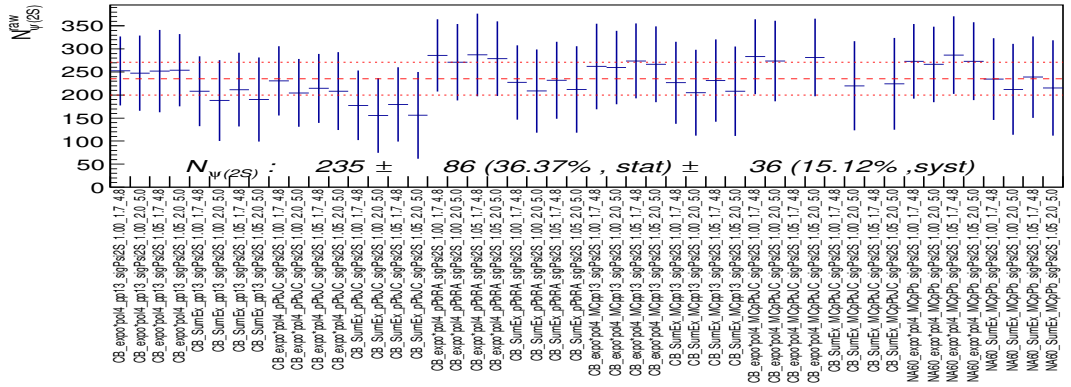

(b) Backward rapidity, multiplicity interval |103, 350|

Figure D.6: Number of ψ(2S) for the backward rapidity in multiplicity intervals.

Bibliography

[1] W. Commons, "File:standard model of elementary particles.svg — wikimedia commons, the free media repository", 2023. https://commons.wikimedia.org/w/index.php?title=File:Standard_Model_of_Elementary_Particles.svg&oldid=774435160. [Online; accessed 15-June-2023].

[2] P. W. Higgs, "Broken Symmetries and the Masses of Gauge Bosons", *Phys. Rev. Lett.* **13** (1964) 508–509.

[3] **ATLAS** Collaboration, G. Aad *et al.*, "Observation of a new particle in the search for the Standard Model Higgs boson with the ATLAS detector at the LHC", *Phys. Lett. B* **716** (2012) 1–29, arXiv:1207.7214 [hep-ex].

[4] **CMS** Collaboration, S. Chatrchyan *et al.*, "Observation of a New Boson at a Mass of 125 GeV with the CMS Experiment at the LHC", *Phys. Lett. B* **716** (2012) 30–61, arXiv:1207.7235 [hep-ex].

[5] **Particle Data Group** Collaboration, P. A. Zyla *et al.*, "Review of Particle Physics", *PTEP* **2020** no. 8, (2020) 083C01.

[6] S. Sarkar, H. Satz, and B. Sinha, eds., *The physics of the quark-gluon plasma*, vol. 785. Springer, 2010.

[7] Z. Fodor and S. D. Katz, "Critical point of QCD at finite T and mu, lattice results for physical quark masses", *JHEP* **04** (2004) 050, arXiv:hep-lat/0402006.

[8] M. Strickland, "Anisotropic Hydrodynamics: Three lectures", *Acta Phys. Polon. B* **45** no. 12, (2014) 2355–2394, arXiv:1410.5786 [nucl-th].

[9] S. Hands, "The Phase diagram of QCD", *Contemp. Phys.* **42** (2001) 209–225, arXiv:physics/0105022.

[10] **ALICE** Collaboration, J. Adam *et al.*, "Measurement of transverse energy at midrapidity in Pb-Pb collisions at $\sqrt{s_{\mathrm{NN}}} = 2.76$ TeV", *Phys. Rev. C* **94** no. 3, (2016) 034903, arXiv:1603.04775 [nucl-ex].

[11] W. Busza, K. Rajagopal, and W. van der Schee, "Heavy Ion Collisions: The Big Picture, and the Big Questions", *Ann. Rev. Nucl. Part. Sci.* **68** (2018) 339–376, arXiv:1802.04801 [hep-ph].

[12] **ALICE** Collaboration, K. Aamodt *et al.*, "Two-pion Bose-Einstein correlations in central Pb-Pb collisions at $\sqrt{s_{NN}}$ = 2.76 TeV", *Phys. Lett. B* **696** (2011) 328–337, arXiv:1012.4035 [nucl-ex].

[13] C. P. Office, "New State of Matter created at CERN. Un nouvel état de la matière",. https://cds.cern.ch/record/716634. Issued on 10 Feb 2000.

[14] **PHENIX** Collaboration, K. Adcox *et al.*, "Formation of dense partonic matter in relativistic nucleus-nucleus collisions at RHIC: Experimental evaluation by the PHENIX collaboration", *Nucl. Phys. A* **757** (2005) 184–283, arXiv:nucl-ex/0410003.

[15] **PHOBOS** Collaboration, B. B. Back *et al.*, "The PHOBOS perspective on discoveries at RHIC", *Nucl. Phys. A* **757** (2005) 28–101, arXiv:nucl-ex/0410022.

[16] **STAR** Collaboration, J. Adams *et al.*, "Experimental and theoretical challenges in the search for the quark gluon plasma: The STAR Collaboration's critical assessment of the evidence from RHIC collisions", *Nucl. Phys. A* **757** (2005) 102–183, arXiv:nucl-ex/0501009.

[17] **BRAHMS** Collaboration, I. Arsene *et al.*, "Quark gluon plasma and color glass condensate at RHIC? The Perspective from the BRAHMS experiment", *Nucl. Phys. A* **757** (2005) 1–27, arXiv:nucl-ex/0410020.

[18] **ALICE** Collaboration, S. A. et al, "The ALICE experiment – A journey through QCD", arXiv:2211.04384 [nucl-ex].

[19] **NA57** Collaboration, F. Antinori *et al.*, "Strangeness enhancements at central rapidity in 40 A GeV/c Pb-Pb collisions", *J. Phys. G* **37** (2010) 045105, arXiv:1001.1884 [nucl-ex].

[20] **NA49** Collaboration, C. Alt *et al.*, "Energy dependence of Lambda and Xi production in central Pb+Pb collisions at A-20, A-30, A-40, A-80, and A-158 GeV measured at the CERN Super Proton Synchrotron", *Phys. Rev. C* **78** (2008) 034918, arXiv:0804.3770 [nucl-ex].

[21] **STAR** Collaboration, B. I. Abelev *et al.*, "Enhanced strange baryon production in Au + Au collisions compared to p + p at s(NN)**(1/2) = 200-GeV", *Phys. Rev. C* **77** (2008) 044908, arXiv:0705.2511 [nucl-ex].

[22] **ALICE** Collaboration, B. B. Abelev *et al.*, "Multi-strange baryon production at mid-rapidity in Pb-Pb collisions at $\sqrt{s_{NN}}$ = 2.76 TeV", *Phys. Lett. B* **728** (2014) 216–227, arXiv:1307.5543 [nucl-ex]. [Erratum: Phys.Lett.B 734, 409–410 (2014)].

[23] R. Pasechnik and M. Šumbera, "Phenomenological Review on Quark–Gluon Plasma: Concepts vs. Observations", *Universe* **3** no. 1, (2017) 7, arXiv:1611.01533 [hep-ph].

[24] **ALICE** Collaboration, J. Adam *et al.*, "Enhanced production of multi-strange hadrons in high-multiplicity proton-proton collisions", *Nature Phys.* **13** (2017) 535–539, arXiv:1606.07424 [nucl-ex].

[25] **ALICE** Collaboration, B. B. Abelev *et al.*, "Multiplicity Dependence of Pion, Kaon, Proton and Lambda Production in p-Pb Collisions at $\sqrt{s_{NN}}$ = 5.02 TeV", *Phys. Lett. B* **728** (2014) 25–38, arXiv:1307.6796 [nucl-ex].

[26] T. Sjostrand, "An introduction to PYTHIA 8.2", *Comput. Phys. Commun.* **191** (2015) 159–177, arXiv:1410.3012 [hep-ph].

[27] T. Pierog, I. Karpenko, J. M. Katzy, E. Yatsenko, and K. Werner, "EPOS LHC: Test of collective hadronization with data measured at the CERN Large Hadron Collider", *Phys. Rev. C* **92** no. 3, (2015) 034906, arXiv:1306.0121 [hep-ph].

[28] C. Bierlich and J. R. Christiansen, "Effects of color reconnection on hadron flavor observables", *Phys. Rev. D* **92** no. 9, (2015) 094010, arXiv:1507.02091 [hep-ph].

[29] **CMS** Collaboration, S. Chatrchyan *et al.*, "Observation of Long-Range Near-Side Angular Correlations in Proton-Lead Collisions at the LHC", *Phys. Lett. B* **718** (2013) 795–814, arXiv:1210.5482 [nucl-ex].

[30] **ALICE** Collaboration, B. Abelev *et al.*, "Long-range angular correlations on the near and away side in p-Pb collisions at $\sqrt{s_{NN}}$ = 5.02 TeV", *Phys. Lett. B* **719** (2013) 29–41, arXiv:1212.2001 [nucl-ex].

[31] **CMS** Collaboration, V. Khachatryan *et al.*, "Observation of Long-Range Near-Side Angular Correlations in Proton-Proton Collisions at the LHC", *JHEP* **09** (2010) 091, arXiv:1009.4122 [hep-ex].

[32] **LHCb** Collaboration, R. Aaij *et al.*, "Measurements of long-range near-side angular correlations in $\sqrt{s_{\mathrm{NN}}}$ = 5TeV proton-lead collisions in the forward region", *Phys. Lett. B* **762** (2016) 473–483, arXiv:1512.00439 [nucl-ex].

[33] J.-P. Lansberg, "New Observables in Inclusive Production of Quarkonia", *Phys. Rept.* **889** (2020) 1–106, arXiv:1903.09185 [hep-ph].

[34] G. T. Bodwin, E. Braaten, and J. Lee, "Comparison of the color-evaporation model and the NRQCD factorization approach in charmonium production", *Phys. Rev. D* **72** (2005) 014004, arXiv:hep-ph/0504014.

[35] **European Muon** Collaboration, J. J. Aubert *et al.*, "The ratio of the nucleon structure functions $F2_n$ for iron and deuterium", *Phys. Lett. B* **123** (1983) 275–278.

[36] K. J. Eskola, P. Paakkinen, H. Paukkunen, and C. A. Salgado, "EPPS16: Nuclear parton distributions with LHC data", *Eur. Phys. J. C* **77** no. 3, (2017) 163, arXiv:1612.05741 [hep-ph].

[37] E. Iancu and R. Venugopalan, *The Color glass condensate and high-energy scattering in QCD*, pp. 249–3363. Wordk Scientific, 3, 2003. arXiv:hep-ph/0303204.

[38] Y.-Q. Ma, P. Tribedy, R. Venugopalan, and K. Watanabe, "Event engineering studies for heavy flavor production and hadronization in high multiplicity hadron-hadron and hadron-nucleus collisions", *Phys. Rev. D* **98** no. 7, (2018) 074025, arXiv:1803.11093 [hep-ph].

[39] F. Arleo and S. Peigne, "J/ψ suppression in p-A collisions from parton energy loss in cold QCD matter", *Phys. Rev. Lett.* **109** (2012) 122301, arXiv:1204.4609 [hep-ph].

[40] F. Arleo and S. Peigne, "Heavy-quarkonium suppression in p-A collisions from parton energy loss in cold QCD matter", *JHEP* **03** (2013) 122, arXiv:1212.0434 [hep-ph].

[41] E. G. Ferreiro, "Excited charmonium suppression in proton–nucleus collisions as a consequence of comovers", *Phys. Lett. B* **749** (2015) 98–103, arXiv:1411.0549 [hep-ph].

[42] C. Lourenco, R. Vogt, and H. K. Woehri, "Energy dependence of J/psi absorption in proton-nucleus collisions", *JHEP* **02** (2009) 014, arXiv:0901.3054 [hep-ph].

[43] **ALICE** Collaboration, S. Acharya *et al.*, "Inclusive J/ψ production at forward and backward rapidity in p-Pb collisions at $\sqrt{s_{\rm NN}}$ = 8.16 TeV", *JHEP* **07** (2018) 160, arXiv:1805.04381 [nucl-ex].

[44] **LHCb** Collaboration, R. Aaij *et al.*, "Prompt and nonprompt J/ψ production and nuclear modification in pPb collisions at $\sqrt{s_{\rm NN}}$ = 8.16 TeV", *Phys. Lett. B* **774** (2017) 159–178, arXiv:1706.07122 [hep-ex].

[45] K. Kovarik *et al.*, "nCTEQ15 - Global analysis of nuclear parton distributions with uncertainties in the CTEQ framework", *Phys. Rev. D* **93** no. 8, (2016) 085037, arXiv:1509.00792 [hep-ph].

[46] K. J. Eskola, H. Paukkunen, and C. A. Salgado, "Nuclear PDFs at NLO - status report and review of the EPS09 results", *Nucl. Phys. A* **855** (2011) 150–157, arXiv:1011.6534 [hep-ph].

[47] Y.-Q. Ma, R. Venugopalan, K. Watanabe, and H.-F. Zhang, "$\psi(2S)$ versus J/ψ suppression in proton-nucleus collisions from factorization violating soft color exchanges", *Phys. Rev. C* **97** no. 1, (2018) 014909, arXiv:1707.07266 [hep-ph].

[48] B. Ducloué, T. Lappi, and H. Mäntysaari, "Forward J/ψ production at high energy: centrality dependence and mean transverse momentum", *Phys. Rev. D* **94** no. 7, (2016) 074031, arXiv:1605.05680 [hep-ph].

[49] F. Arleo and S. Peigné, "Quarkonium suppression in heavy-ion collisions from coherent energy loss in cold nuclear matter", *JHEP* **10** (2014) 073, arXiv:1407.5054 [hep-ph].

[50] B. Chen, T. Guo, Y. Liu, and P. Zhuang, "Cold and Hot Nuclear Matter Effects on Charmonium Production in p+Pb Collisions at LHC Energy", *Phys. Lett. B* **765** (2017) 323–327, arXiv:1607.07927 [nucl-th].

[51] J.-P. Lansberg and H.-S. Shao, "Towards an automated tool to evaluate the impact of the nuclear modification of the gluon density on quarkonium, D and B meson production in proton–nucleus collisions", *Eur. Phys. J. C* **77** no. 1, (2017) 1, arXiv:1610.05382 [hep-ph].

[52] J. L. Albacete *et al.*, "Predictions for Cold Nuclear Matter Effects in p+Pb Collisions at $\sqrt{s_{NN}}$ = 8.16 TeV", *Nucl. Phys. A* **972** (2018) 18–85, arXiv:1707.09973 [hep-ph].

[53] **ALICE** Collaboration, S. Acharya *et al.*, "Measurement of nuclear effects on ψ(2S) production in p-Pb collisions at $\sqrt{s_{\rm NN}}$ = 8.16 TeV", *JHEP* **07** (2020) 237, arXiv:2003.06053 [nucl-ex].

[54] **ALICE** Collaboration, S. Acharya *et al.*, "Multiplicity dependence of J/ψ production at midrapidity in pp collisions at $\sqrt{s}$ = 13 TeV", *Phys. Lett. B* **810** (2020) 135758, arXiv:2005.11123 [nucl-ex].

[55] B. Z. Kopeliovich, H. J. Pirner, I. K. Potashnikova, K. Reygers, and I. Schmidt, "J/ψ in high-multiplicity pp collisions: Lessons from pA collisions", *Phys. Rev. D* **88** no. 11, (2013) 116002, arXiv:1308.3638 [hep-ph].

[56] E. Levin, I. Schmidt, and M. Siddikov, "Multiplicity dependence of quarkonia production in the CGC approach", *Eur. Phys. J. C* **80** no. 6, (2020) 560, arXiv:1910.13579 [hep-ph].

[57] E. G. Ferreiro and C. Pajares, "High multiplicity pp events and J/ψ production at LHC", *Phys. Rev. C* **86** (2012) 034903, arXiv:1203.5936 [hep-ph].

[58] N. Armesto, M. A. Braun, E. G. Ferreiro, and C. Pajares, "Percolation approach to quark - gluon plasma and J / psi suppression", *Phys. Rev. Lett.* **77** (1996) 3736–3738, arXiv:hep-ph/9607239.

[59] H. J. Drescher, "Parton based Gribov-Regge theory", *Phys. Rept.* **350** (2001) 93–289, arXiv:hep-ph/0007198.

[60] **ALICE** Collaboration, S. Acharya *et al.*, "Forward rapidity J/ψ production as a function of charged-particle multiplicity in pp collisions at $\sqrt{s}$ = 5.02 and 13 TeV", *JHEP* **06** (2022) 015, arXiv:2112.09433 [nucl-ex].

[61] **CMS** Collaboration, S. Chatrchyan *et al.*, "Event Activity Dependence of Υ(nS) Production in $\sqrt{s_{NN}}$=5.02 TeV pPb and $\sqrt{s}$=2.76 TeV pp Collisions", *JHEP* **04** (2014) 103, arXiv:1312.6300 [nucl-ex].

[62] **CMS** Collaboration, A. M. Sirunyan *et al.*, "Investigation into the event-activity dependence of Υ(nS) relative production in proton-proton collisions at $\sqrt{s}$ = 7 TeV", *JHEP* **11** (2020) 001, arXiv:2007.04277 [hep-ex].

[63] **ALICE** Collaboration, S. Acharya *et al.*, "J/ψ production as a function of charged-particle multiplicity in p-Pb collisions at $\sqrt{s_{\rm NN}}$ = 8.16 TeV", *JHEP* **09** (2020) 162, arXiv:2004.12673 [nucl-ex].

[64] O. S. Bruning, P. Collier, P. Lebrun, S. Myers, R. Ostojic, J. Poole, and P. Proudlock, "LHC Design Report Vol.1: The LHC Main Ring", CERN-2004-003-V1, CERN-2004-003, CERN-2004-003-V-1.

[65] **ALICE** Collaboration, K. Aamodt *et al.*, "The ALICE experiment at the CERN LHC", *JINST* **3** (2008) S08002.

[66] **ALICE** Collaboration, B. B. Abelev *et al.*, "Performance of the ALICE Experiment at the CERN LHC", *Int. J. Mod. Phys. A* **29** (2014) 1430044, arXiv:1402.4476 [nucl-ex].

[67] **ATLAS** Collaboration, G. Aad *et al.*, "The ATLAS Experiment at the CERN Large Hadron Collider", *JINST* **3** (2008) S08003.

[68] **CMS** Collaboration, S. Chatrchyan *et al.*, "The CMS Experiment at the CERN LHC", *JINST* **3** (2008) S08004.

[69] **LHCb** Collaboration, A. A. Alves, Jr. *et al.*, "The LHCb Detector at the LHC", *JINST* **3** (2008) S08005.

[70] **ALICE** Collaboration, G. Dellacasa *et al.*, "ALICE technical design report of the inner tracking system (ITS)", CERN-LHCC-99-12. http://cds.cern.ch/record/391175.

[71] **ALICE** Collaboration, C. W. Fabjan *et al.*, "ALICE: Physics Performance Report", *J. Phys. G* **32** (2006) 1295–2040.

[72] **ALICE** Collaboration, G. Dellacasa *et al.*, "ALICE: Technical design report of the time projection chamber", CERN-OPEN-2000-183, CERN-LHCC-2000-001. http://cds.cern.ch/record/451098.

[73] **ALICE** Collaboration, G. Dellacasa *et al.*, "ALICE technical design report of the zero degree calorimeter (ZDC)", CERN-LHCC-99-05. http://cds.cern.ch/record/381433.

[74] **ALICE** Collaboration, P. Cortese *et al.*, "ALICE technical design report on forward detectors: FMD, T0 and V0", CERN-LHCC-2004-025. http://cds.cern.ch/record/781854.

[75] **ALICE** Collaboration, G. Dellacasa *et al.*, "ALICE technical design report of the dimuon forward spectrometer", CERN-LHCC-99-22. http://cds.cern.ch/record/401974.

[76] https://twiki.cern.ch/twiki/bin/viewauth/ALICE/MuonTracking. Last accessed 03 August 2023.

[77] M. Tarhini, *Measurement of Z-boson and J/ψ Production in p-Pb and Pb-Pb Collisions at* $\sqrt{s_{NN}}$ *= 5.02 TeV with ALICE at the LHC.* PhD thesis, Orsay, IPN, CERN, 2017.

[78] J. Crkovská, *Study of the J/ψ production in pp collisions at* $\sqrt{s}$ *= 5.02 TeV and of the J/ψ production multiplicity dependence in p-Pb collisions at* $\sqrt{s_{NN}}$ *= 8.16 TeV with ALICE at the LHC.* PhD thesis, Orsay, IPN, 2018.

[79] S. Roesler, R. Engel, and J. Ranft, "The Monte Carlo event generator DPMJET-III", in *International Conference on Advanced Monte Carlo for Radiation Physics, Particle Transport Simulation and Applications (MC 2000)*, pp. 1033–1038. 12, 2000. arXiv:hep-ph/0012252.

[80] V. Zaccolo, *Charged-Particle Multiplicity Distributions over Wide Pseudorapidity Range in Proton-Proton and Proton-Lead Collisions with ALICE*. PhD thesis, Bohr Inst., 2015.

[81] **ALICE** Collaboration, A. et al., "Quarkonium signal extraction in ALICE", ALICE-PUBLIC-2015-006.

[82] **ALICE** Collaboration, S. Acharya *et al.*, "Energy dependence of forward-rapidity J/ψ and ψ(2S) production in pp collisions at the LHC", *Eur. Phys. J. C* **77** no. 6, (2017) 392, arXiv:1702.00557 [hep-ex].

[83] **ALICE** Collaboration, S. Acharya *et al.*, "Measurement of ψ(2S) production as a function of charged-particle pseudorapidity density in pp collisions at $\sqrt{s}$ = 13 TeV and p-Pb collisions at $\sqrt{s_{\rm NN}}$ = 8.16 TeV with ALICE at the LHC", *JHEP* **06** (2023) 147, arXiv:2204.10253 [nucl-ex].

[84] X.-N. Wang and M. Gyulassy, "hijing: A monte carlo model for multiple jet production in pp, pA, and AA collisions", *Phys. Rev. D* **44** (Dec, 1991) 3501–3516. https://link.aps.org/doi/10.1103/PhysRevD.44.3501.

[85] **ALICE** Collaboration, S. Acharya *et al.*, "Charged-particle pseudorapidity density at mid-rapidity in p-Pb collisions at $\sqrt{s_{\rm NN}}$ = 8.16 TeV", *Eur. Phys. J. C* **79** no. 4, (2019) 307, arXiv:1812.01312 [nucl-ex].

[86] A. Esposito, E. G. Ferreiro, A. Pilloni, A. D. Polosa, and C. A. Salgado, "The nature of X(3872) from high-multiplicity pp collisions", *Eur. Phys. J. C* **81** no. 7, (2021) 669, arXiv:2006.15044 [hep-ph].

[87] K. J. Eskola, H. Paukkunen, and C. A. Salgado, "EPS09: A New Generation of NLO and LO Nuclear Parton Distribution Functions", *JHEP* **04** (2009) 065, arXiv:0902.4154 [hep-ph].

[88] H. Paukkunen, "Nuclear PDFs Today", *PoS* **HardProbes2018** (2018) 014, arXiv:1811.01976 [hep-ph].

[89] K. Werner, B. Guiot, I. Karpenko, and T. Pierog, "Analysing radial flow features in p-Pb and p-p collisions at several TeV by studying identified particle production in EPOS3", *Phys. Rev. C* **89** no. 6, (2014) 064903, arXiv:1312.1233 [nucl-th].

[90] **ALICE** Collaboration, B. Abelev *et al.*, "J/ψ Production as a Function of Charged Particle Multiplicity in pp Collisions at $\sqrt{s}$ = 7 TeV", *Phys. Lett. B* **712** (2012) 165–175, arXiv:1202.2816 [hep-ex].

[91] **ALICE** Collaboration, S. Acharya *et al.*, "Studies of J/ψ production at forward rapidity in Pb-Pb collisions at $\sqrt{s_{\rm NN}}$ = 5.02 TeV", *JHEP* **02** (2020) 041, arXiv:1909.03158 [nucl-ex].

[92] **ALICE** Collaboration, J. Adam *et al.*, "Measurement of an excess in the yield of J/ψ at very low p_{T} in Pb-Pb collisions at $\sqrt{s_{\mathrm{NN}}} = 2.76$ TeV", *Phys. Rev. Lett.* **116** no. 22, (2016) 222301, arXiv:1509.08802 [nucl-ex].

[93] **ALICE** Collaboration, J. Adam *et al.*, "Centrality Dependence of the Charged-Particle Multiplicity Density at Midrapidity in Pb-Pb Collisions at $\sqrt{s_{\mathrm{NN}}} = 5.02$ TeV", *Phys. Rev. Lett.* **116** no. 22, (2016) 222302, arXiv:1512.06104 [nucl-ex].

[94] **ALICE** Collaboration, S. Acharya *et al.*, "Coherent J/ψ photoproduction at forward rapidity in ultra-peripheral Pb-Pb collisions at $\sqrt{s_{\mathrm{NN}}} = 5.02$ TeV", *Phys. Lett. B* **798** (2019) 134926, arXiv:1904.06272 [nucl-ex].

[95] **ALICE** Collaboration, A. et al., "Multiplicity dependence of Υ production at forward rapidity in pp collisions at $\sqrt{s} = 13$ TeV", arXiv:2209.04241 [nucl-ex].

[96] T. Chowdhury, *Study of Υ production as a function of charged-particle multiplicity in proton-proton collisions at $\sqrt{s} = 13$ TeV with ALICE at the LHC.* PhD thesis, Clermont-Ferrand U., 2019. https://theses.hal.science/tel-02302458.

[97] **ALICE** Collaboration, B. Abelev *et al.*, "Upgrade of the ALICE Experiment: Letter Of Intent", *J. Phys. G* **41** (2014) 087001 CERN-LHCC-2012-012, CERN-LHCC-I-022, ALICE-UG-001.

[98] **ALICE** Collaboration, A. et al., "A Forward Calorimeter (FoCal) in the ALICE experiment",. http://cds.cern.ch/record/2696471.

[99] **ALICE** Collaboration, A. et al., "Expression of Interest for an ALICE ITS Upgrade in LS3",. http://cds.cern.ch/record/2644611.

[100] **ALICE** Collaboration, F. Reidt, "Upgrade of the ALICE ITS detector", *Nucl. Instrum. Meth. A* **1032** (2022) 166632, arXiv:2111.08301 [physics.ins-det].

[101] **ALICE** Collaboration, B. Abelev *et al.*, "Technical Design Report for the Upgrade of the ALICE Inner Tracking System", *J. Phys. G* **41** (2014) 087002 CERN-LHCC-2013-024, ALICE-TDR-017.

[102] **ALICE** Collaboration, P. Antonioli, A. Kluge, and W. Riegler, "Upgrade of the ALICE Readout & Trigger System", CERN-LHCC-2013-019, ALICE-TDR-015. http://cds.cern.ch/record/1603472.

[103] **ALICE** Collaboration, A. et al., "Technical Design Report for the Muon Forward Tracker", CERN-LHCC-2015-001, ALICE-TDR-018. https://cds.cern.ch/record/1981898.

[104] P. Buncic, M. Krzewicki, and P. Vande Vyvre, "Technical Design Report for the Upgrade of the Online-Offline Computing System", CERN-LHCC-2015-006, ALICE-TDR-019. http://cds.cern.ch/record/2011297.

[105] J. Martin Blanco, *Study of J/ψ production dependence with the charged particle multiplicity in p-Pb collisions at $\sqrt{s_{\mathrm{NN}}} = 5.02$ TeV and pp collisions at $\sqrt{s} = 8$ TeV with the ALICE experiment at the LHC.* PhD thesis, Nantes U., 1, 2016.

[106] R. Sadek Finot, *MFT commissioning and preparation for Run 3 data analysis with ALICE (LHC, CERN)*. Theses, Ecole nationale supérieure Mines-Télécom Atlantique, Oct., 2022. https://theses.hal.science/tel-04008085.

[107] **ALICE** Collaboration, adam et al., "Future high-energy pp programme with ALICE",.